MASTER

LBL-11322

Lawrence Berkeley Laboratory

UNIVERSITY OF CALIFORNIA

Physics, Computer Science & Mathematics Division

JETS IN $e^+ e^-$ ANNIHILATION

Susan Catherine Cooper
(Ph.D. thesis)

RECEIVED BY TIC SEP 10 1980

August 1980

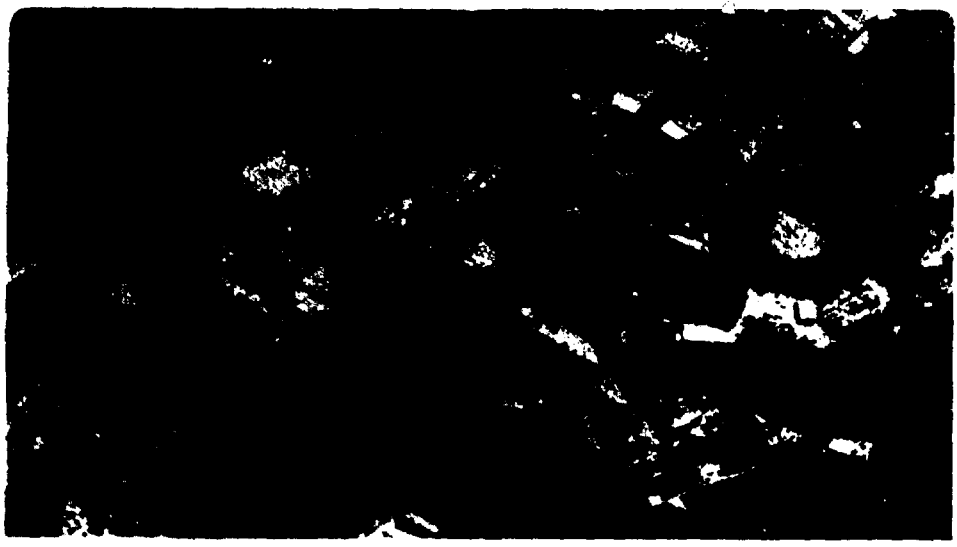

Prepared for the U.S. Department of Energy under Contract W-7405-ENG-48

DISTRIBUTION OF THIS DOCUMENT IS UNLIMITED

LEGAL NOTICE

This book was prepared as an account of work sponsored by an agency of the United States Government. Neither the United States Government nor any agency thereof, nor any of their employees, makes any warranty, express or implied, or assumes any legal liability or responsibility for the accuracy, completeness, or usefulness of any information, apparatus, product, or process disclosed, or represents that its use would not infringe privately owned rights. Reference herein to any specific commercial product, process, or service by trade name, trademark, manufacturer, or otherwise, does not necessarily constitute or imply its endorsement, recommendation, or favoring by the United States Government or any agency thereof. The views and opinions of authors expressed herein do not necessarily state or reflect those of the United States Government or any agency thereof.

Jets in e^+e^- Annihilation

DISCLAIMER

Susan Catherine Cooper

Lawrence Berkeley Laboratory
University of California
Berkeley, California

August 1980

ABSTRACT

The properties of jets produced in e^+e^- annihilation have been investigated using data taken with the Mark 1 detector at SPEAR. The momentum distributions parallel and perpendicular to the jet axis were measured for all charged tracks, for K^0s, and for ρ^0s. The K^0 and ρ^0 Pt^2 distributions are well fit by the form $dn/dPt^2 = A \exp(-B \cdot Pt^2)$ with B = 4.6 +/- 0.2 for K^0s and 5 +/- 1 for ρ^0s. The charged particle Pt^2 distribution cannot be fit with a single exponential, but is similar to that of K^0s and ρ^0s above $Pt^2 \sim 0.2$ GeV^2. The charged particle and K^0 parallel momentum distributions are similar in shape and

DISTRIBUTION OF THIS DOCUMENT IS UNLIMITED

approximately exponential. The production of ρ^0s at low parallel momentum is suppressed. The average number of ρ^0s per event is 0.4 +/- 0.1.

ACKNOWLEDGEMENTS

The data used in this thesis were taken with the SLAC-LBL magnetic detector before I joined the collaboration. I wish to thank all those who participated in the construction and running of SPEAR and the magnetic detector. For their particular contributions at various times in my graduate career, I thank Willy Chinowsky, Jim Wiss, Jim Siegrist, Gail Hanson, and Vera Luth.

This work was supported by the U.S. Department of Energy under Contract W-7405-ENG-48.

TABLE OF CONTENTS

ACKNOWLEDGEMENTS i

Chapter page

I. INTRODUCTION 1

Discovery of Jets in e^+e^- Annihilation 2
The Jet Model 10
Angular Distribution of Jet Axis 10
Detailed Jet Properties 12

II. DETECTOR 15

Trigger 21
Tracking 23
Event Selection 23
Monte Carlo Detector Simulation 26

III. DETERMINATION OF JET AXIS 28

Sphericity 28
Thrust and Sphericity 30
Analysis of Sphericity Axis Error 31
Visible Energy Cut 34
High Momentum Track Cut 38

IV. CHARGED PARTICLE DISTRIBUTIONS 42

Method of Efficiency Calculations 44
Momenta Parallel to the Jet Axis 49
Momenta Transverse to the Jet Axis 59

V. K^0 PRODUCTION 69

K^0 Selection 77
K^0 Momentum Distributions 84

VI. ρ^0 PRODUCTION 90

Background Determination 93
Method 1 93
Method 2 96
Method 3 100
Results 101
Comparison with Previous Measurements 109

Mass 109
Rate 110
Momentum Distributions 111

VII. CONCLUSION 117

Appendix page

A. RADIATIVE CORRECTIONS 120

B. LIMITED TRANSVERSE MOMENTUM MODEL 128

C. FEYNMAN-FIELD MODEL 137

LIST OF TABLES

Table page

1. Mark 1 Detector Components 19

2. $x_{\parallel}$ 53

3. pt^2 64

4. Estimate of Strange Sea Quark Fraction 74

5. ρ^0 Production 103

6. Initial State Radiation. 125

7. Parameters for LIMPT Model 136

LIST OF FIGURES

Figure		page
1.	Observed Pt^2 Distribution	5
2.	Observed Sphericity Distributions	6
3.	Observed X Distribution	8
4.	Observed Sphericity Distributions	9
5.	ϕ Distribution of Observed Jet Axis	14
6.	Observed inclusive α vs. X	15
7.	Mark 1 Detector	17
8.	Mark 1 Detector	18
9.	TASH efficiency	22
10.	Vertex Position	25
11.	Sphericity Axis Error	33
12.	Visible Energy	35
13.	Average Sphericity Axis Error	36
14.	Average Event Properties	37
15.	Average Jet Axis Error vs. Largest $X_{\parallel}$	39
16.	Average Event Properties for $X_{\parallel}$ Cut	40
17.	Raw Distributions in $X_{\parallel}$ and Pt^2	43
18.	Uncorrected, Tau Subtracted $X_{\parallel}$	50
19.	Error in $X_{\parallel}$	51
20.	Efficiency for $X_{\parallel}$	54
21.	Corrected $X_{\parallel}$ Distribution	55
22.	$X_{\parallel}$ in Feynman-Field Model	57

23. $x_{\parallel}$ of Primary Hadrons 58
24. Tau subtracted, Uncorrected Pt^2 60
25. Comparison of Data and Monte Carlo. 61
26. Efficiency for Pt^2 62
27. Corrected Pt^2 Distribution 63
28. Error in Pt^2 66
29. Pt^2 in Feynman-Field Model 67
30. Pt^2 of Primary Hadrons 68
31. R(K) vs. center-of-mass energy 71
32. Average number of kaons per event 72
33. K^0 Production in Feynman-Field Model. 76
34. Uncut $\pi^+\pi^-$ Mass Distribution 78
35. $\pi^+\pi^-$ Mass Distribution with Final Cuts 80
36. Plots of cut quantities 82
37. Primary vertex position 83
38. K^0 Efficiency 86
39. K^0 Momentum Distributions 87
40. K^0 Momentum Distributions 88
41. K^0 Sources. 89
42. $M(\pi^+\pi^-)$ for various mass bins. 92
43. Same-Sign Background 95
44. Fits to ρ mass with same-sign background. 97
45. Fits to ρ mass with exponential background. 99
46. Comparison of Methods 1,2&3 102
47. Corrected $x_{\parallel}$ and Pt^2 of ρ^0s. 105
48. ρ^0 Production in the Feynman-Field Model. 107
49. ρ^0 Momenta in Feynman-Field Model. 108

50. $R(\rho^0)$ vs. Ecm. 112

51. ρ^0 Production vs. Ecm. 113

52. Pt^2 distribution of ρ^0s 115

53. $X_{\parallel}$ Distribution of ρ^0s 116

54. Feynman graphs for $e^+e^- \longrightarrow q\,\bar{q}$ 121

55. Effect of Radiation on Jet Axis 127

56. Flow Chart of Quark Fragmentation 139

57. Feynman-Field Charged Particle $X_{\parallel}$ 142

58. The Joining of Two Jets. 144

59. Total Energy and Momentum before Re-scaling. . . . 145

Chapter I

INTRODUCTION

According to the quark-parton model, hadronic final states are produced in e^+e^- annihilation via a three step process: the electron and the positron annihilate to form a heavy virtual photon, the photon produces a quark and an anti-quark, and they in turn produce hadrons. The first two steps are described by well-understood Quantum Electrodynamics and are exactly the same in lowest order as for the process $e^+e^- \longrightarrow \mu^+\mu^-$ except that the quark charge replaces the muon charge. Thus the ratio R of the cross sections for $e^+e^- \longrightarrow$ hadrons and $e^+e^- \longrightarrow \mu^+\mu^-$ should be constant and equal to the sum of the squares of the quark charges multiplied by 3 because each quark can have each of 3 colors. In fact the data[1] show two regions of nearly constant R, in approximate agreement with production of up, down and strange quarks (charges 2/3, -1/3 and -1/3, hence R=2) below 4 GeV, and with the addition of charmed quark production (charge 2/3, increasing R to 3 1/3) above that energy. The discovery of the psi particles at 3.095 GeV[2],

---

[1] J. L. Siegrist (thesis) SLAC-225, 1979.

[2] J.-E. Augustin et al., Phys. Rev. Lett. 33:1406, 1974
J. J. Aubert et al., Phys. Rev. Lett. 33:1404, 1974.

3.685 GeV[3], and 3.77 GeV[4] and of charmed meson production above 4 GeV[5] has given strong support to the presence of the charmed quark in this picture.

1.1 DISCOVERY OF JETS IN e^+e^- ANNIHILATION

The mechanism by which quarks turn into hadrons is not well understood, but the suggestion[6] that the hadrons might cluster about the quark direction, resulting in two oppositely-directed "jets" of particles in e^+e^- annihilation, was investigated by Gail Hanson using Mark 1 data taken at center-of-mass energies between 3 and 7.8 GeV[7]. Evidence for jets was seen at center-of-mass energies above 5 GeV.

The clustering may be expressed as a limitation of momentum transverse to the quark direction, similar to the

---

[3]G. S. Abrams et al., Phys. Rev. Lett. 33:1453, 1974.

[4]P. Rapidis et al., Phys. Rev. Lett. 39:526 and 974, 1977.

[5]G. Goldhaber, F. Pierre, et al., Phys. Rev. Lett. 37:255, 1976.

[6]S. D. Drell, D. J. Levy, and T. M. Yan, Phys. Rev. 187:2159, 1969, and Phys. Rev. D1:1617, 1970.
N. Cabibbo, G. Parisi, and M. Testa, Lett. Nuovo Cimento 4:35, 1970.
J. D. Bjorken and S. J. Brodsky, Phys. Rev. D1:1416, 1970.
R. P. Feynman, Photon-Hadron Interactions, (W. A. Benjamin, Inc., 1972), p. 166.

[7]G. Hanson et. al., Phys. Rev. Lett. 35:1609, 1975.

limitation of momentum transverse to the beam direction that is characteristic of hadron interactions. We might expect the average transverse momentum in e^+e^- annihilation to be similar to the .3 to .4 GeV/c average transverse momentum seen in hadron interactions. In e^+e^- annihilation, the average hadron momentum increases from .47 to .66 GeV/c as the total center-of-mass energy goes from 3 to 7.4 GeV.[3] Thus these energies are not sufficiently high for the clustering to be obvious in a visual inspection of events; our jet studies must rely on statistical analyses.

One would like to plot the hadron momenta transverse to the quark direction. However it is impossible to know the quark direction for any given event since hadrons, not quarks, are detected; but if this picture were correct one would expect that the quark axis would be close to an axis which in some way minimizes the transverse momenta of the hadrons or maximizes the longitudinal momenta.

The particular approach used was suggested in a footnote to a paper by Bjorken and Brodsky[9] and is described in detail in chapter 3 of this thesis. The sphericity axis is defined to minimize the sum of the squares of the transverse momenta. Of course, such an axis exists for any event. Figure 1 illustrates this for a Monte Carlo model which has

---

[8] J.L. Siegrist (thesis) SLAC-225, 1979.

[9] J.D.Bjorken and S.J. Brodsky, Phys. Rev. D1:1416, 1970.

a multiplicity distribution chosen to fit our data above 7 Gev but with the particle momenta distributed according to Lorentz-invariant phase space, hence not jet-like. Transverse momenta relative to an arbitrary axis and to the sphericity axis are plotted. For events of infinite multiplicity these distributions would be the same, but for our average detected multiplicity of 4 the sphericity axis gives substantially lower transverse momenta. However the transverse momenta relative to the sphericity axis for the data are considerably lower than for this phase space model, which means there must be a real effect limiting the transverse momenta.

The effect is shown better in terms of the sphericity which is defined as the minimum of the sum of the squares of the transverse momenta, normalized to a maximum possible value of 1.0:

$$S = 1.5 \min \frac{\sum_{i=1}^{n} Pt_i^2}{\sum_{i=1}^{n} P_i^2}$$

The sphericity distributions for several center-of-mass energies are shown in Figure 2 and contrasted to the predictions of the phase space model.

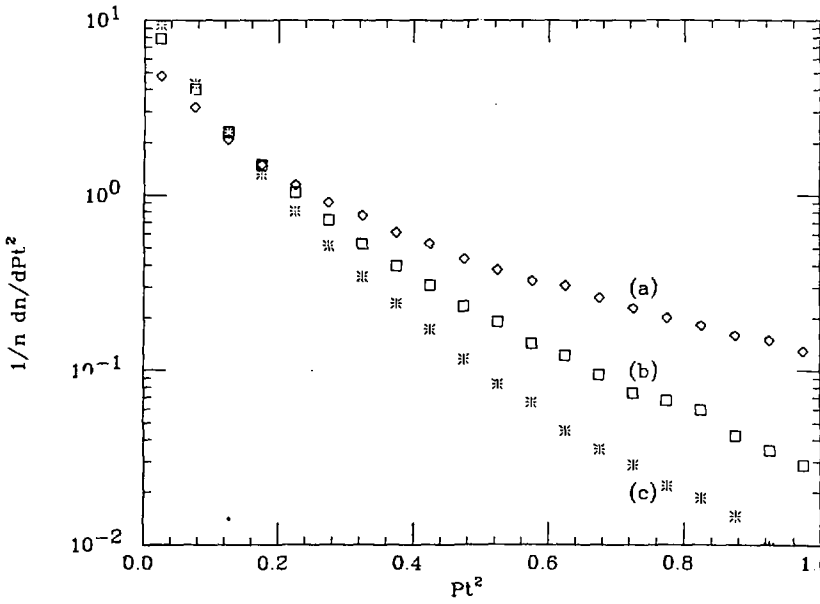

Figure 1: Observed Pt^2 Distribution.
a) Pt^2 relative to an arbitrary axis for all detected tracks of the phase space Monte Carlo.
b) Pt^2 relative to the observed sphericity axis for all detected tracks of the phase space Monte Carlo.
c) Pt^2 relative to the observed sphericity axis for the data.

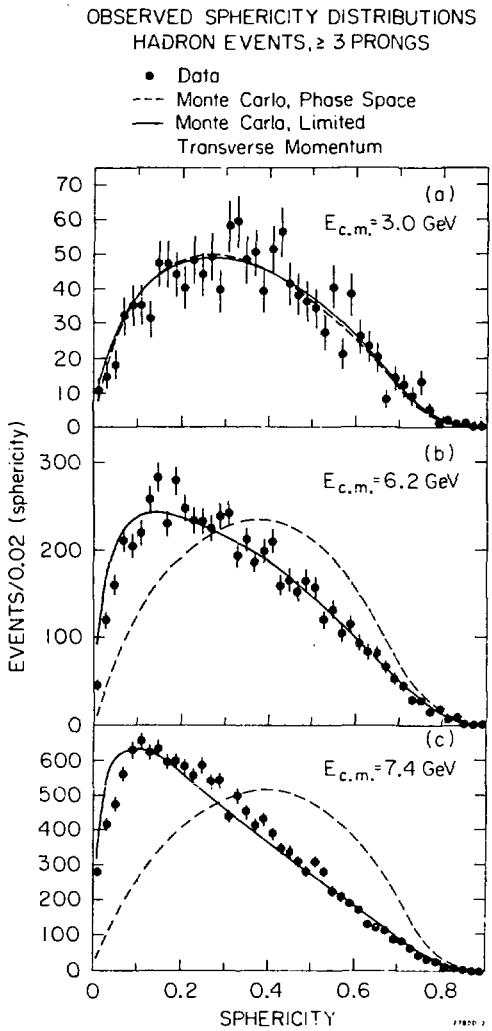

Figure 2: Observed Sphericity Distributions for data (points), jet model (solid curves) and phase space model (dashed curves) for center-of-mass energies (a) 3.0 GeV, (b) 6.2 GeV, (c) 7.4 GeV.

The data also disagree with the phase space model predictions for the distribution in scaled momentum $X = P/Pmax$ for $X>.4$ as shown in Figure 3. To show that the disagreement in sphericity is not due only to this excess of high momentum particles, the sphericity distribution is shown in Figure 4 separately for events in which there is no detected track of $X > 0.4$.

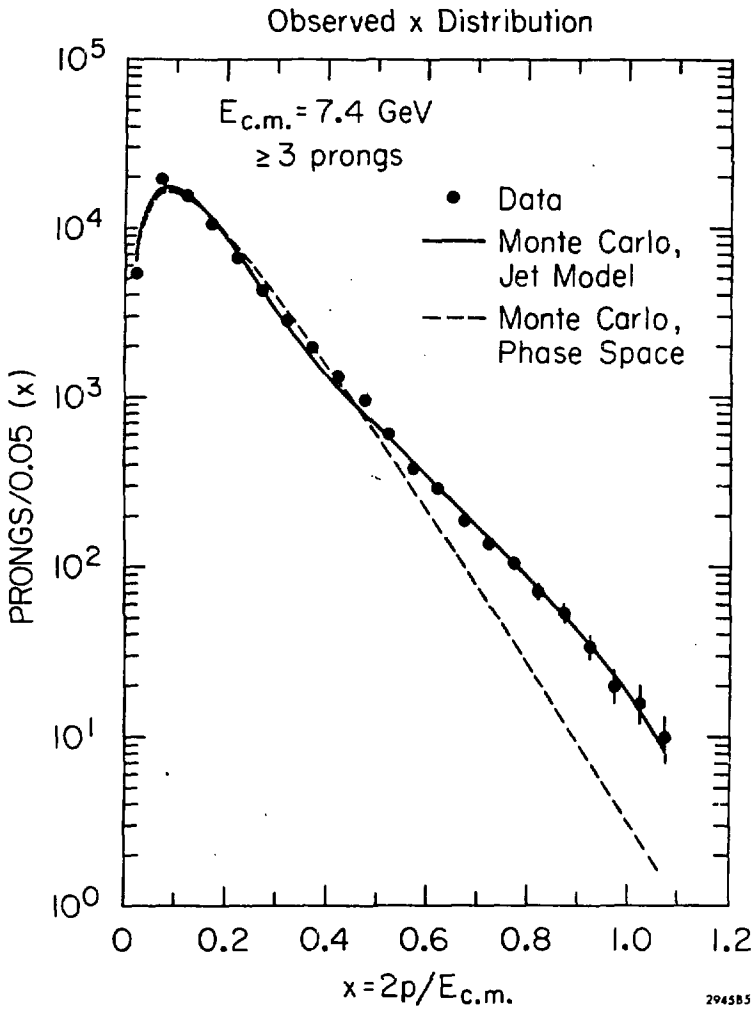

Figure 3: Observed X Distribution at 7.4 GeV center-of-mass energy for data (points), jet model (solid curve) and phase space model (dashed curve).

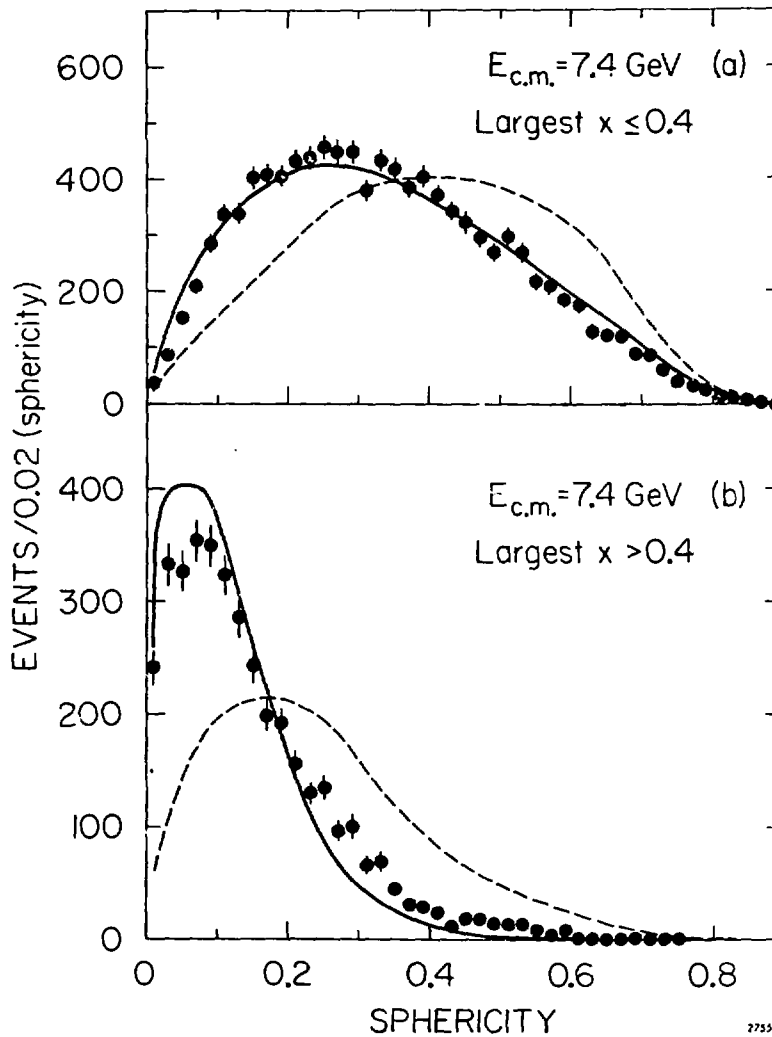

Figure 4: Observed Sphericity Distributions at 7.4 GeV center-of-mass energy for data (points), jet model (solid curve) and phase space model (dashed curve): (a) for events containing no detected track of X > 0.4, (b) for events with a detected track of X > 0.4.

1.2 THE JET MODEL

A very simple jet model was constructed to incorporate the limited transverse momentum. The program GENIS[10] was used to generate transverse momenta with a $\exp(-b\ Pt^2)$ distribution and longitudinal momenta according to Lorentz invariant phase space. All particles were assumed to be pions. The total multiplicity was chosen with a Poisson distribution. The average total multiplicity, the average fraction of pions that were neutral, and the transverse momentum parameter b were adjusted to fit the data. Initial state radiation was included as described in Appendix A. The resulting agreement with the data is excellent as shown in Figures 2 and 3. In the contrasting "phase space model", all three components of momenta were chosen according to Lorentz invariant phase space using the program GOGEN.[11]

1.3 ANGULAR DISTRIBUTION OF JET AXIS

The quarks and hence the jet axis should have the same $1+\cos^2\theta$ distribution as the muons in $e^+e^- \longrightarrow \mu^+\mu^-$, where θ is the polar angle with respect to the e^+ beam direction. Within the limited θ acceptance of the Mark 1 detector, this

---

[10] W. Kittel, L. Van Hove and W. Wojcik, Comp. Phys. Comm. 1:425, 1970. This program has since been replaced with the more efficient GENIUS: D. C. Carey and D. Drijard, J. Comp. Phys. 28:327, 1978.

[11] J. H. Friedman, J. Comp. Phys. 7:201, 1971.

angular distribution is very hard to determine. However it turns out that for some center-of-mass energies the electrons and positrons stored in SPEAR become polarized along the direction of the magnetic field of the bending magnets of SPEAR. In this case the angular distribution is

$$\frac{d\sigma}{d\Omega} \sim 1 + \alpha \cos^2\theta + \alpha P^2 \sin^2\theta \cos 2\Phi$$

where P is the magnitude of the polarization and Φ is the azimuthal angle about the beam axis measured from the plane of the storage ring. The polarization has a time dependence

$$P(t) = P_0 \; (1 - \exp(-t/\tau)).$$

The $\cos 2\Phi$ angular dependence was observed[12] in the $e^+e^- \longrightarrow \mu^+\mu^-$ reaction with $P_0{}^2$ = .76 +/- .05 and τ approximately 10 minutes at 7.4 GeV, indicating the existence of beam polarization at this energy. The $\cos 2\Phi$ dependence was also observed[13] for the jet axis: Figure 5 shows the Φ distribution of the jet axis at an energy where polarization does not occur and at 7.4 GeV where it does. The data with polarization are consistent with the prediction for the distribution of the detected jet axis for α=1.0 and the time-averaged value of P^2 = 0.47 as determined from $e^+e^- \longrightarrow$

---

[12] J.G. Learned et. al., Phys. Rev. Lett. 35:1688, 1975.

[13] G. Hanson et. al., Phys. Rev. Lett., 35:1609. 1975. G. Hanson et. al., SLAC-PUB-1814, 1976. Also in Tutzing Conf. 1976:313 (QCD 161:C49:1976) and Tbilisi Conf. 1976:B1 (QCD 161:H51:1976:v.2).

$\mu^+\mu^-$ data taken simultaneously. The best fit gives $\alpha = 0.97$ +/- 0.14. This angular distribution is also evident in the high momentum tracks[14]. Figure 6 shows the value of the inclusive α as a function of the scaled momentum X compared to the predictions of the simple jet model.

1.4 DETAILED JET PROPERTIES

The existence of jets in e^+e^- annihilation was established by the work we have summarized in this chapter. That work used only final state charged particles, without any particle identification. In this thesis, we extend the investigation of jets to include some of the heavy particles. We measure the total production of K^0s and ρ^0s, as well as their momentum distributions parallel and perpendicular to the jet axis. In addition, we repeat the earlier measurements of charged particle momenta, using Monte Carlo models which include heavy particle production to check for systematic errors.

Our data sample contains approximately 40,000 hadronic events taken with the SLAC-LBL magnetic detector (Mark 1) at the electron-positron storage ring SPEAR. These data were taken with beam energies ranging between 3.5 GeV and the maximum possible at SPEAR, 3.9 GEV. The average total

---

[14] R.F. Schwitters et. al., Phys. Rev. Lett. 35:1320, 1975.

center-of-mass energy for these data is 7.3 GeV. The Mark 1 detector has been replaced by the Mark II, which has better momentum resolution and somewhat larger solid angle. In addition, the Mark II has reasonable photon detection capabilities, which were almost entirely lacking with the Mark 1. However, high statistics and high energy are important in the study of jets. The discovery of charmed particles lead the Mark II collaboration to take most of their data at lower energies, leaving the Mark 1 data superior for jet studies in the SPEAR energy range.

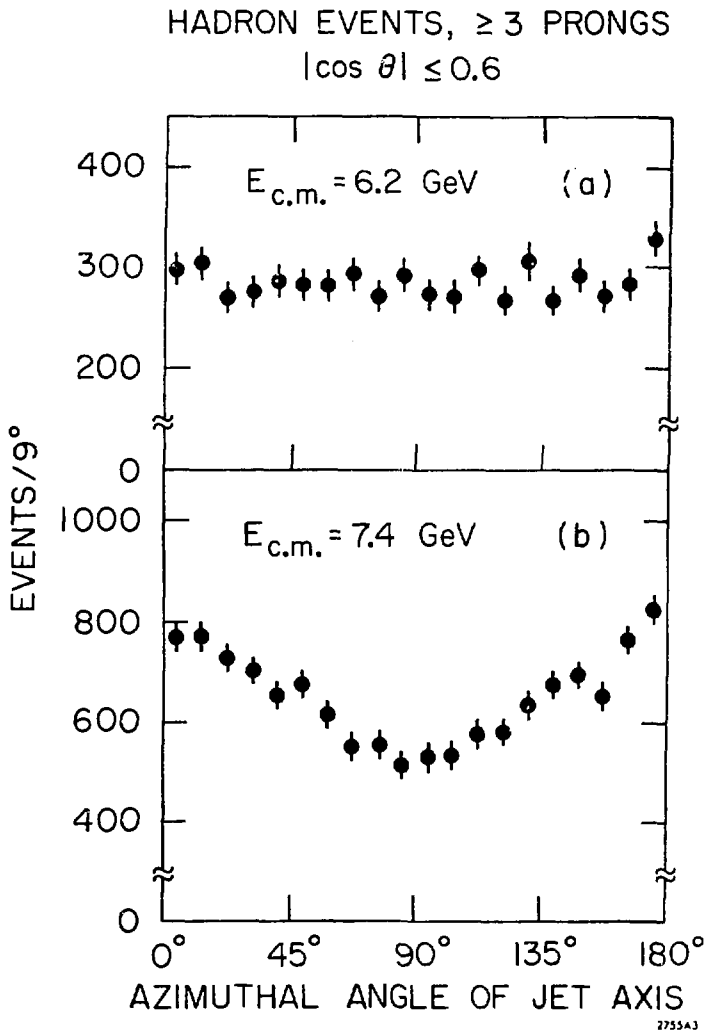

Figure 5: ϕ for jet axes with $|\cos\theta|<0.6$ for center-of-mass energies (a) 6.2 GeV and (b) 7.4 GeV.

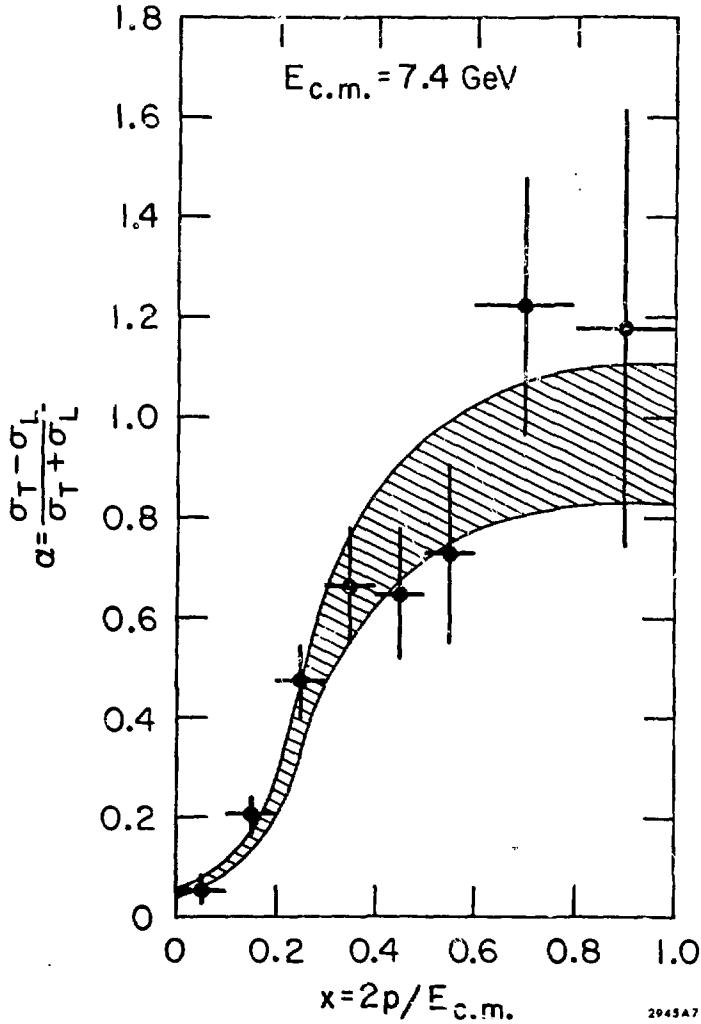

Figure 6: Observed inclusive α vs. X for particles with $|\cos\theta|<0.6$ in hadronic events at 7.4 GeV center-of-mass energy. The prediction of the jet model Monte Carlo simulation for a jet axis angular distribution with $\alpha=0.97+/-0.14$ is represented by the shaded band.

Chapter II

DETECTOR

The data discussed in this thesis were taken with the SPEAR magnetic detector (posthumously renamed the Mark 1) in 1975 and 1976. The detector had a .4 Tesla solenoidal magnetic field provided by 1.7 m radius coil with its axis on the beam line. Inside the magnet were proportional chambers and spark chambers which provided charged particle tracking over 73% of 4π sr. Scintillation counters just inside the magnet coil were used for time-of-flight measurements. A layer of lead-scintillator-sandwich shower counters outside the magnet coil were used to distinguish minimum-ionizing particles from particles which produce electromagnetic showers. Scintillation counters around the beam pipe ("pipe counters") were used in the trigger. In addition there were spark chambers outside the magnet return yoke and additional shielding to separate muons from hadrons, but they were not used in this thesis. Figures 7 and 8 show the size and placement of the various pieces of the Mark 1. Table 1 lists the thickness of the various parts.

The standard coordinate system was right-handed with the z axis parallel to the beam and the y axis vertical,

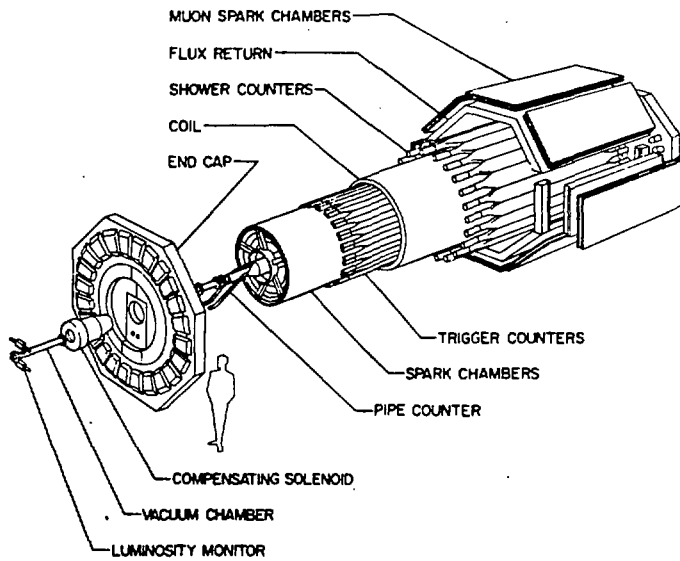

Figure 7: Mark 1 Detector

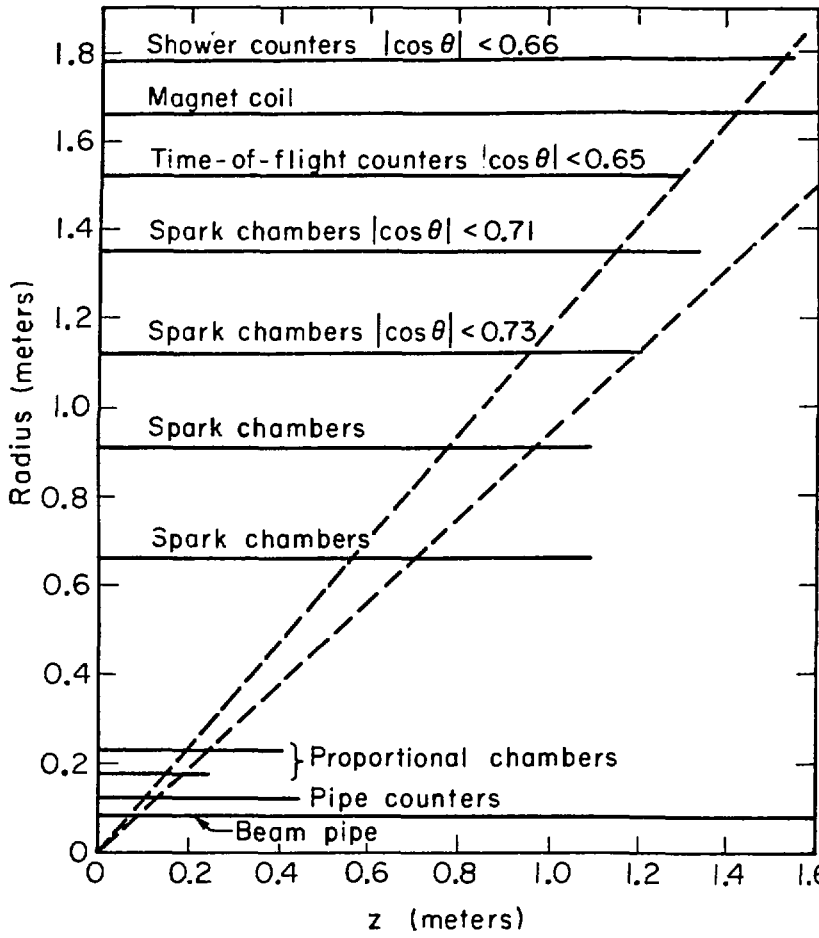

XBL807-3494

Figure 8: Mark 1 Detector
One-quarter view of Mark 1 detector showing radii and active lengths of measuring devices. The upper dotted line indicates the solid angle for TASH (limited by the length of the time-of-flight counters). The lower dotted line indicates the solid angle for charged particle detection (limited by the length of the third spark chamber module).

TABLE 1

MARK I DETECTOR COMPONENTS

(all dimensions in cm)

Item	Average Radius	Fraction of 4π Acceptance	Length (z)	Thickness	Fraction of Radiation Length	Fraction of Absorption Length
Beampipe	8.0	-	-	0.0273	0.016	0.002
Pipe Counters	12.0	0.83	90	1.37	0.033	0.020
MWPC1	17.3	0.82	±25	1.98	0.0066	-
MWPC2	22.4	0.88	±41	1.98	0.0066	-
WSC1	66	0.86	±110	3.8	0.0017	0.001
WSC2	91	0.77	±110	3.8	0.0017	0.001
WSC3	112	0.73	±120	3.8	0.0017	0.001
WSC4	135	0.71	±134	3.8	0.0017	0.001
TOF Counters	152.4	0.65	±130	2.5	0.060	0.037
Coil	166.4	0.74	±182.9	11.0	1.0	0.24
Shower Counters	178.4	0.66	±155	13.0	5.79	0.22
Flux Return	211	-	±183	20.0	11.4	1.17
Muon WSC	219	0.73	±234	5.7	0.22	0.07

parallel to the magnetic field of the bending magnets of SPEAR. The origin was at the center of the detector which was also the nominal intersection point of the e^+ and e^- beams. The angle θ was measured from the +z axis; ϕ was measured in the xy plane from the +x axis.

Each of the four spark chamber modules had two spark gaps, one with the wires strung at +/- 2 degrees to the beam, the other with wires at +/- 4 degrees. Since signals were read out on all four "planes" of wires, this gave two space points per module. The efficiency measured on-line was at least 90% per plane. The wire spacing was 1 mm, giving effective spacings in z of 29 mm and 14 mm.

The two proportional chambers were installed as close as possible to the beam pipe to improve the vertex reconstruction. All the wires ran parallel to the beam and only anode readout was used so there was no z information. There were 512 wires per chamber, giving wire spacings of 2.1 mm at a radius of 0.17 m and 2.8 mm at 0.22 m. The efficiency measured on-line was at least 90% per chamber.

More detailed descriptions can be found in the several theses on the Mark 1 which have preceded this one[15].

---

[15] Robert Hollebeek LBL-3874 (1975);
John Zipse LBL-4281 (1975);
J. Scott Whitaker LBL-5518 (1976);
James Wiss LBL-6725 (1977);
Petros Rapidis SLAC-220 (1979);
James Siegrist SLAC-225 (1979)

2.1 TRIGGER

The hardware trigger required combinations of signals in the various scintillation counters. A signal in the pipe counter was required to reduce cosmic ray background. In addition two charged tracks were required to produce signals in the time-of-flight counters and the shower counters. The use of the shower counters in the trigger was necessary to reduce backgrounds from non-annihilation events which were found to produce mainly low energy particles. Some of these could reach the time-of-flight counters, but most of them stopped in the 11 cm thick aluminum magnet coil before reaching the shower counters. To ensure that the shower counter signals were due to charged tracks, a shower counter signal was used only if one of the four nearby time-of-flight counters also fired; this combination was called a "TASH".

The TASH efficiency as a function of momentum is shown in Figure 9. This efficiency was measured from the data using events with three or more tracks. At high momentum the efficiency levels off to a value somewhat less than 1.0 because of counter inefficiency, due mostly to the cracks between the 24 shower counter modules. At low momentum it fails to reach its expected value of 0.0 because a low momentum track and a photon hitting the same counter could together make a TASH.

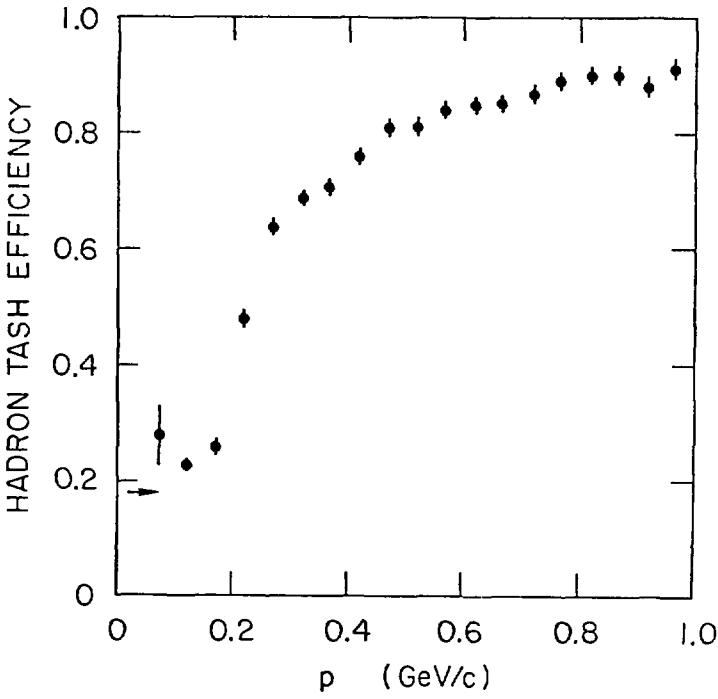

Figure 9: TASH efficiency as a function of momentum for charged particles with $|\cos\theta|<0.65$ in multi-hadron events. The arrow indicates the accidental rate.

Unfortunately this requirement of 2 TASHes also eliminated some annihilation events. Monte Carlo studies indicated that 65% of all hadronic events would have 3 or more charged tracks in the 73% solid angle of the detector with at least 150 MeV/c momentum transverse to the beam, and that 88% of these events would trigger.

2.2 TRACKING

The track-finding program required a track to have a signal on at least three of the four planes of three of the four spark chamber modules. Using the efficiency per plane of 90% this requirement gives an efficiency per track of 98.5%. To reach the third spark chamber module a track needed a minimum of 67 MeV/c momentum transverse to the beam. Since hand-scanning of events showed that some fake tracks were found with high curvature and that the spark chambers were less reliable for tracks far from normal incidence, a higher cut of 150 MeV/c was made. Tracks which did not pass within 60 cm in z and 15 cm in xy projection of the origin were discarded. The momentum resolution was approximately $\sigma/p = 2\%\ p$.

2.3 EVENT SELECTION

Only events with three or more detected tracks passing the above cuts were used. To ensure a valid trigger, at

least two of these tracks as reconstructed must point towards a time-of-flight counter and a shower counter that actually fired. A vertex was formed from all the tracks in an event. It is essentially the point which has the smallest mean distance-of-closest approach to all the tracks. Histograms of the vertex position are shown in Figure 10. If this vertex was further than 10 cm in z or 4 cm in xy projection from the origin, the event was assumed to be due to a collision of a beam particle with the beam pipe or with the residual gas in the pipe, and it was discarded. Further cuts were applied to the 3 and 4 prong events to reduce background from multi-prong Bhabhas ($e^+e^- \longrightarrow e^+e^-$ events in which one of the final state particles produced another particle by scattering or radiation). These cuts eliminated less than 3% of the events and are discussed in detail in the thesis of J. Siegrist.

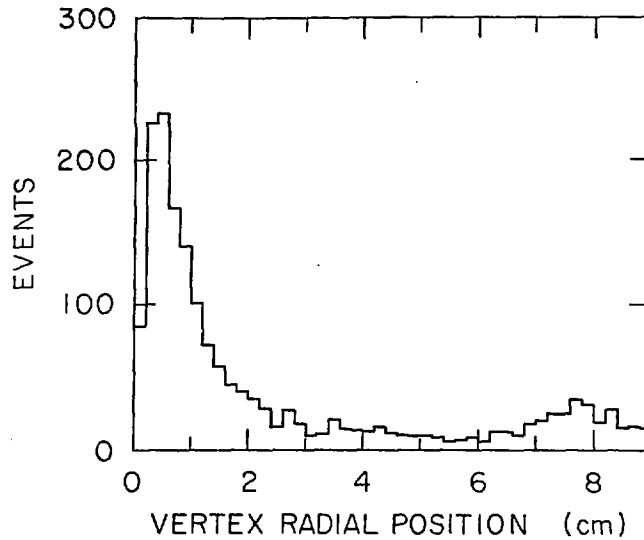

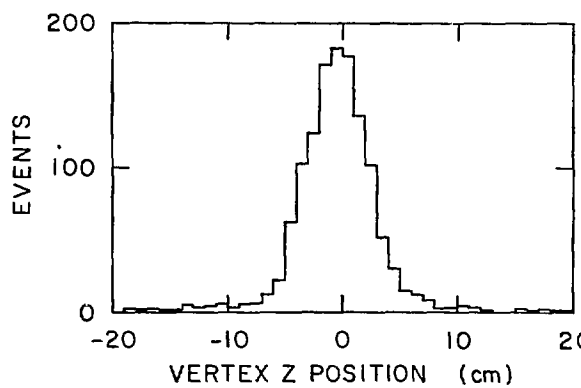

Figure 10: Vertex Position
(a) Radial distribution of event verticies.
(b) z distribution of event verticies for events with vertex radius < 4 cm.

2.4 MONTE CARLO DETECTOR SIMULATION

The mark 1 analysis of jets must depend on charged particles only, and about 25% of them are lost through the ends of the detector. This limitation has substantial effects on the analysis, which are described in detail in Chapter 3. In order to compare the data to a particular model it is necessary to have a Monte Carlo program to simulate the detector. The program used was HOWL, a multi-purpose program suitable for any detector using a solenoidal magnetic field and cylindrical geometry. It propagated each particle from its point of origin through the detector until it either passed outside or decayed. Along the way it paused at each specified layer of detector to do whatever was suitable. At the average radius of the beam pipe and the pipe counters multiple scattering and energy loss were applied to charged tracks and photons could convert into e^+e^- pairs. At each of the proportional chambers and spark chamber modules a "measured" point was generated using the appropriate measurement error. At the radius of the time-of-flight counters, "signals" in the phototubes at each end of the appropriate counter were generated. These signals included the propagation time along the counter and a Gaussian time error for each tube. At the shower counter radius the TASH efficiency of Figure 9 was used to decide whether to record a TASH for the track. The measured points for each track were then fit to a circle

in the xy plane and a straight line in z vs xy arclength to find a measured momentum and distance of closest approach to the origin. For tracks that hit a time-of-flight counter, a measured time-of-flight was calculated using the phototube signals. Thus the confusion caused when more than one track hits the same counter was automatically included. The events were then subjected to the same cuts as the data, as given above.

Chapter III

DETERMINATION OF JET AXIS

By "jet axis" we mean the direction of the quark before it fragments. Unfortunately we cannot detect the quark directly. However, we expect the hadrons to come out with small transverse momenta relative to the quark direction, so we can hope to approximate the quark direction by finding the axis which minimizes the hadron transverse momenta or some function thereof. In this chapter we investigate various techniques of approximating the jet axis, and the errors involved at our average total center-of-mass energy of 7.3 GeV.

3.1 SPHERICITY

The practice of finding the axis which minimizes the sum of the squares of the transverse momenta comes from a suggestion by Bjorken and Brodsky[16]. It is particularly convenient because the solution can be found by dialgonalizing a 3 X 3 matrix, a process which is both fast and reliable. One constructs a momentum analogue of the moment-of-inertia tensor

---

[16] J. D. Bjorken and S. J. Brodsky, Phys. Rev. D1:1416, 1970.

$$T_{ab} = \sum_{i=1}^{n} P_a P_b$$

where a and b refer to the 3 components of momentum and the sum is over all particles. The tensor is diagonalized giving the eigenvalues

$$T_{kk} = \sum_{i=1}^{n} P_k^2 .$$

T33 is conventionally chosen to be the largest of the three, and we can show that the corresponding eigenvector is the jet axis. Working in the coordinate system which diagonalizes T and expressing the longitudinal momentum Pl along some arbitrary axis N=(N1,N2,N3), we have

$$Pl = \sum_{a=1}^{3} P_a N_a$$

$$Pl^2 = \sum_{a=1}^{3} \sum_{b=1}^{3} P_a N_a P_b N_b$$

$$\sum_{i=1}^{n} Pl^2 = \sum_{a=1}^{3} \sum_{b=1}^{3} N_a T_{ab} N_b$$

$$= N_1^2 T_{11} + N_2^2 T_{22} + (1-N_1-N_2)^2 T_{33}$$

We have ordered the eigenvalues so that T33 > T22 > T11, so to maximize the sum of Pl^2, we maximize the coefficient of T33, which gives N1=N2=0. The axis found by this technique is called the sphericity axis, and a measure of "jetiness", sphericity, is defined from the eigenvalues

$$S = \frac{3}{2} \frac{T11+T22}{T11+T22+T33} = \frac{3}{2} \frac{\sum Pt^2}{\sum P^2}$$

where Pt is the momentum transverse to the sphericity axis.

3.2 THRUST AND SPHEROCITY

Some other techniques have been suggested which are meant to be less sensitive to the details of quark fragmentation by virtue of being linear rather than quadratic in momentum. One is to find the axis $\vec{N}$ which maximizes the directed momentum d:[17]

$$d(\vec{N}) = \text{sum } \vec{P}*\vec{N}\ \theta(\vec{P}*\vec{N})$$

where the sum runs over all particles and θ is the unit step function ($\theta(x>0) = 1$, $\theta(x<0) = 0$). Again we can avoid an analytical maximization procedure. We find the vector sum of momenta for each of the possible combinations of particles. The longest of these is in just the direction to maximize sum $\vec{P}*\vec{N}$. Since adding in any of the other particles would decrease its length, it must be that each of them has $\theta(\vec{N}*\vec{P})=0$ and is therefore properly eliminated from the sum, and N is the vector that maximizes the directed momentum. This axis has become known as the thrust axis, and the quantity thrust

$$T = 2 \max d(\vec{N}) \ / \ \text{sum } |\vec{P}|$$

is a measure of the "jetiness" of an event.

---

[17] First suggested by S. Brandt et. al., Phys. Lett. 12:57, 1964.
Revived by E. Fahri, Phys. Rev. Lett. 39:1587, 1977.
The name thrust comes from De Rujula et. al., Nucl. Phys. B138:387, 1978.

Another suggestion has been to find the spherocity axis by minimizing the spherocity S' which is proportional to

$$\frac{\text{sum } |Pt|}{\text{sum } |P|}$$

This technique finds the "wrong" axis in certain intuitively obvious cases[18] and has therefore fallen into disfavor. For example, consider two particles of equal momentum with an opening angle of 20 degrees. The thrust and sphericity axes both lie equidistant between the two particles. The spherocity has two equal minima, giving axes parallel to each of the two particles.

3.3 ANALYSIS OF SPHERICITY AXIS ERROR

We want to know how well these techniques reproduce the true jet axis. For this we use the limited-transverse-momentum phase space model which generates particles according to phase space multiplied by a matrix element $|M|^2 = \exp(-\text{sum } Pt^2/R^2)$ which limits the momentum transverse to a given axis. This axis is then the true jet axis, corresponding to the direction of a quark which fragments with this matrix element. Since the model limits Pt rather than minimizing it, the axis found by any of the above techniques will be somewhat different from the true axis, even if all particles are detected.

---

[18] S. Brandt and H. D. Dahmen, Z. fur Phys. C1:61, 1979.

For studying the jet axis error, we plot as a function of θ the fraction of events that have their true jet axes within angle θ of their sphericity axes. The solid line in Figure 11 shows this distribution for the limited-transverse-momentum all-pion Monte Carlo. Here all the particles that come from the primary vertex were used in determining the sphericity axis. Only events that have no initial state radiation were used. These are the conditions we will henceforth refer to as the "pure Monte Carlo". Since there are no decays or missing particles, the error is entirely due to the kinematics and represents a lower limit to the error we can expect from the data if the whole kinematic region of the model is accepted. (There are some selection criteria that will achieve a smaller jet axis error at the price of biasing the sample of events -- for example the requirement of a high momentum particle discussed later.)

The dashed line in Figure 11 shows the jet axis error plot for the same model but with only detected particles used to determine the jet axis. In this case all detected events are included, regardless of initial state radiation. This is referred to as the "detected Monte Carlo". Here the jet axis error is much larger, as we expect since we detect charged particles over only 73% of the solid angle and neutrals not at all, so that a substantial fraction of the energy is lost.

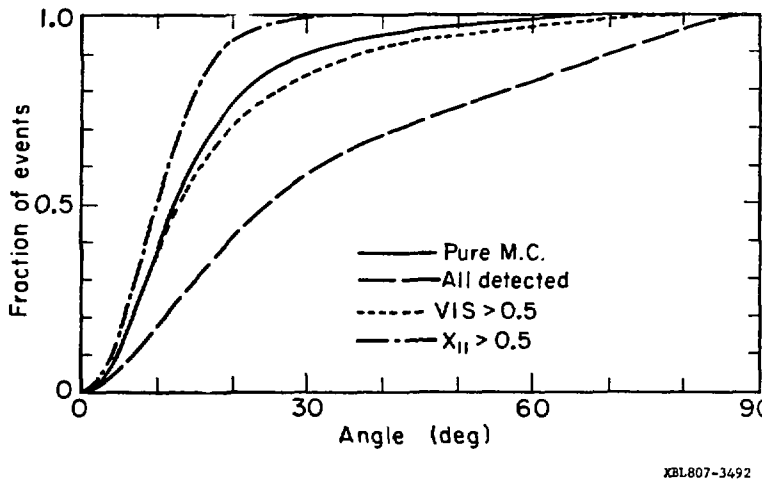

Figure 11: Sphericity Axis Error.
Fraction of events that have their true jet axis within angle θ of their sphericity axis.

3.3.1 Visible Energy Cut

Figure 12 is a plot of the data for the ratio of visible energy (calculated assuming pion masses) to the nominal center-of-mass energy. The average is 43%.

We would expect that events with most of the energy detected would have a smaller jet axis error than those where most of it is lost. Figure 13 is a plot of the average jet axis error as a function of the visible energy fraction. If we look only at events where at least half of the energy is detected (32% of all detected events), the jet axis error is comparable to that of the pure Monte Carlo. The distribution is shown in Figure 11.

To see what biases are introduced by this cut we plot in Figure 14 various averages taken over all the primary vertex particles as a function of the visible energy fraction. The events with high visible energy have larger momenta and lower multiplicity and sphericity, while the transverse momenta remain unchanged. As we raise the cut on visible energy, the error on the jet axis decreases, but the biases resulting from the cut increase. We have decided that requiring at least half of the energy be detected is a reasonable compromise. The Monte Carlo is used to co[illegible]t for the resulting bias.

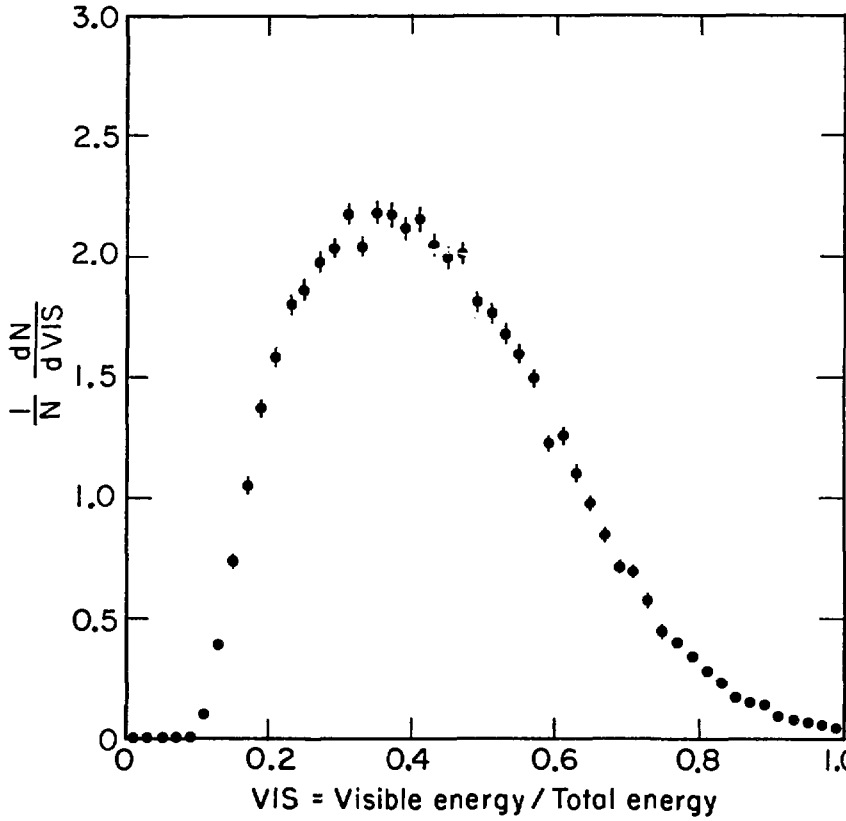

XBL807-3493

Figure 12: Visible Energy / total energy for data, assuming all tracks are pions.

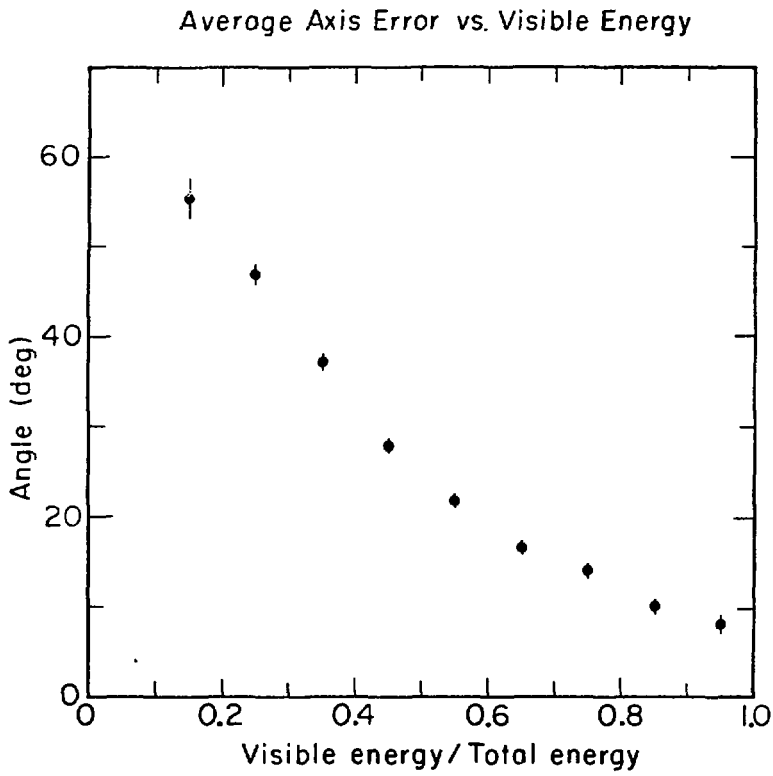

XBL807-3491

Figure 13: Average Sphericity Axis Error vs. visible energy fraction.

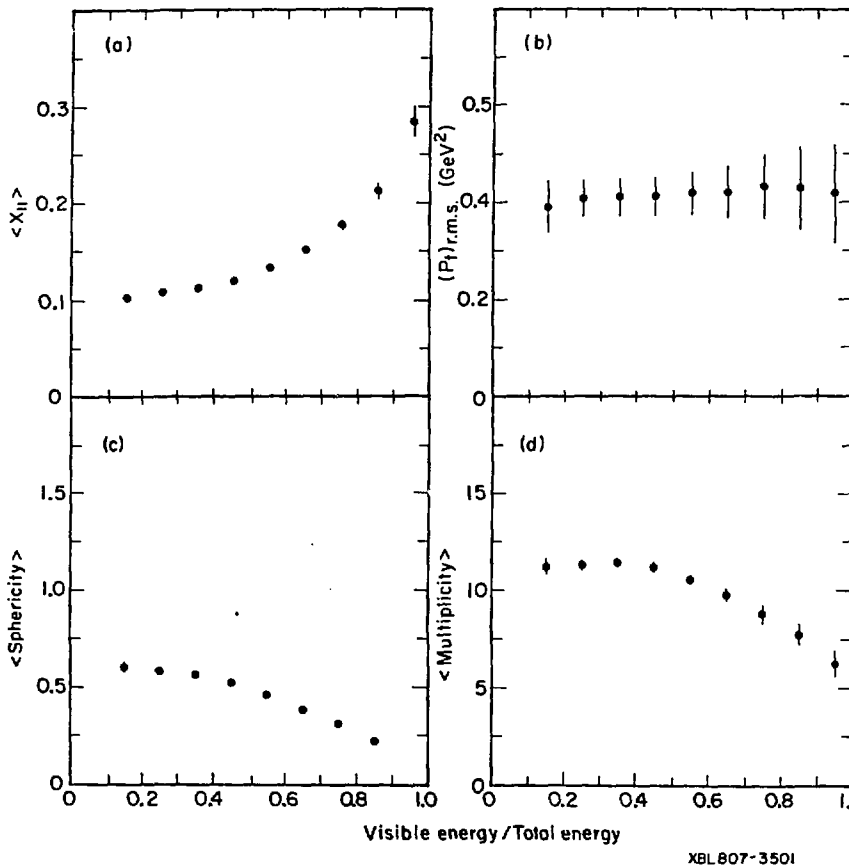

Figure 14: Average Event Properties vs. visible energy fraction.
a) average produced X||.
b) root-mean-square value of produced Pt.
c) average produced sphericity.
d) average produced multiplicity.

3.3.2 High Momentum Track Cut

The jet axis error is also smaller in events that have a high momentum track. In Figure 15 we show the average angle between the true jet axis and the detected sphericity axis as a function of the largest X|| in the event. Requiring a high momentum particle would obviously bias the momentum distribution, but this effect should be minimal for applications where we can look only at tracks in the opposite jet from the "trigger" particle. To see if this is true in our model, we look again at produced primary particles, this time considering each half of the event separately. The separation is made according to the produced jet axis. In Figure 16 we show the average X|| and the root-mean-square Pt of primary vertex particles as a function of the highest produced X|| in the opposite jet. The average X|| is fairly strongly affected by the requirement of a high momentum track in the opposite jet, but the transverse momentum in quite constant. Twelve percent of the detected jets have a track of X||>.5 opposite them. The jet axis error distribution with this requirement is even better than for the pure Monte Carlo, as shown in Figure 11.

We have investigated the jet axis errors using thrust instead of sphericity. Since the results were quite similar, with the average error slightly larger, we use only

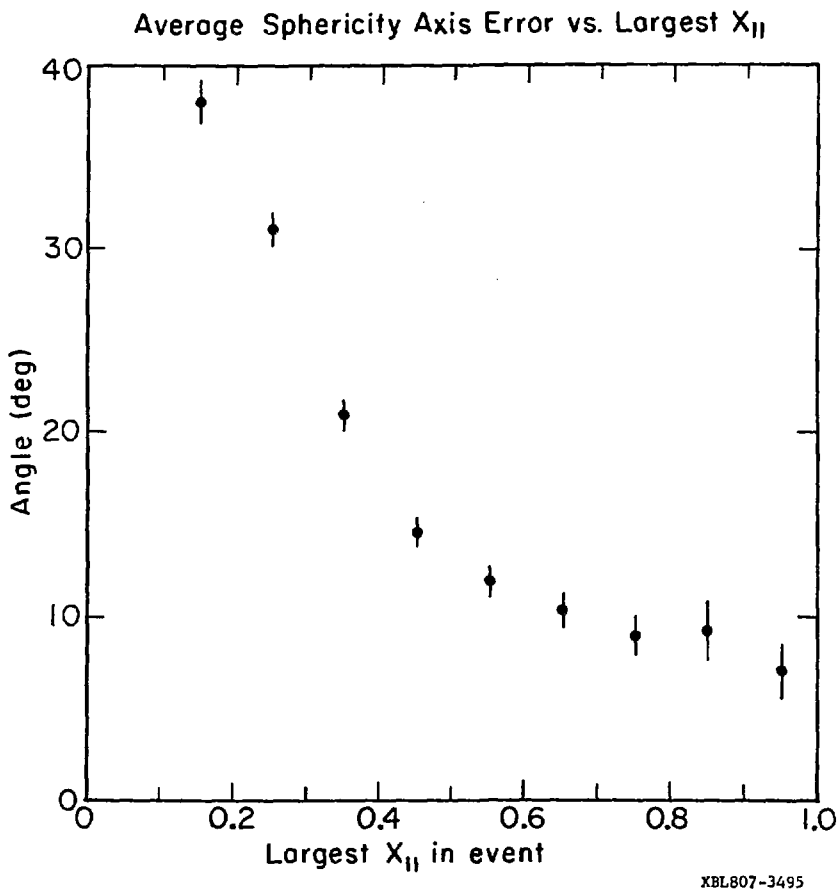

Figure 15: Average Jet Axis Error vs. Largest $X_{\parallel}$ in opposite jet.

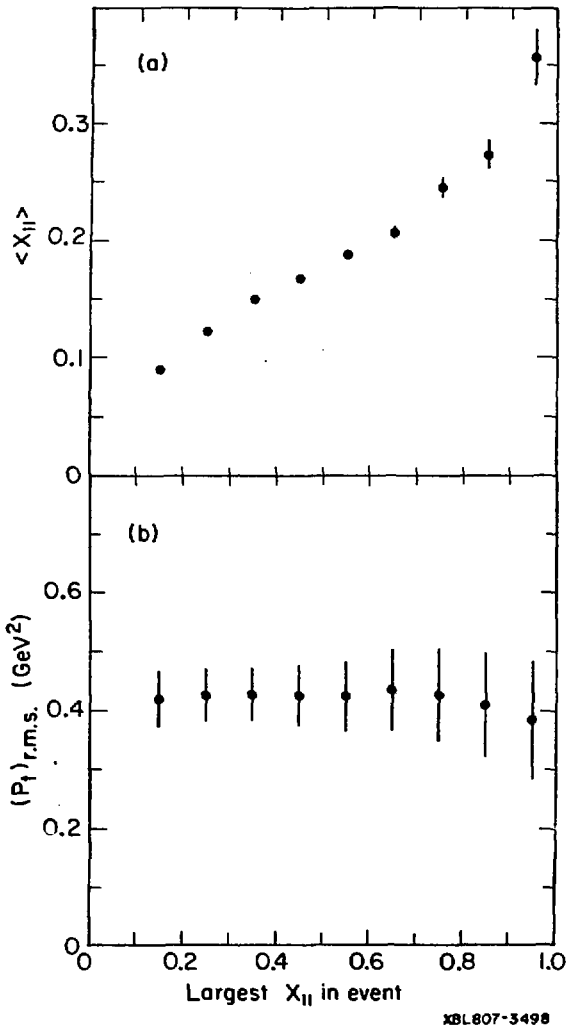

Figure 16: Average Event Properties for $X_{\parallel}$ Cut
a) average produced $X_{\parallel}$.
b) root-mean-square value of produced Pt.

sphericity in the following chapters. The effects of the jet axis errors on the momentum distributions we measure will be shown in the next chapter.

Chapter IV

CHARGED PARTICLE DISTRIBUTIONS

The primary $q\,\bar{q}$ pair produced in e^+e^- annihilation fragment into the hadrons we can observe. This fragmentation process cannot be understood with current theoretical ideas. However we can observe the results of that process in the distributions of hadron momenta parallel and perpendicular to the quark direction. The variables to be measured here are the scaled momentum parallel to the jet axis:

$$X_{||} = \frac{|\vec{P} * \vec{N}|}{E_{beam}}$$

where $\vec{N}$ is a unit vector along the jet axis, and the square of the momentum transverse to the jet axis:

$$Pt^2 = (\vec{P} \times \vec{N})^2$$

The uncorrected distributions in $X_{||}$ and Pt^2 are shown in Figure 17 for the approximately 45,000 events which passed our cuts (described in Chapter 2). These events were taken between 7.0 and 7.8 GeV total center-of-mass energy.

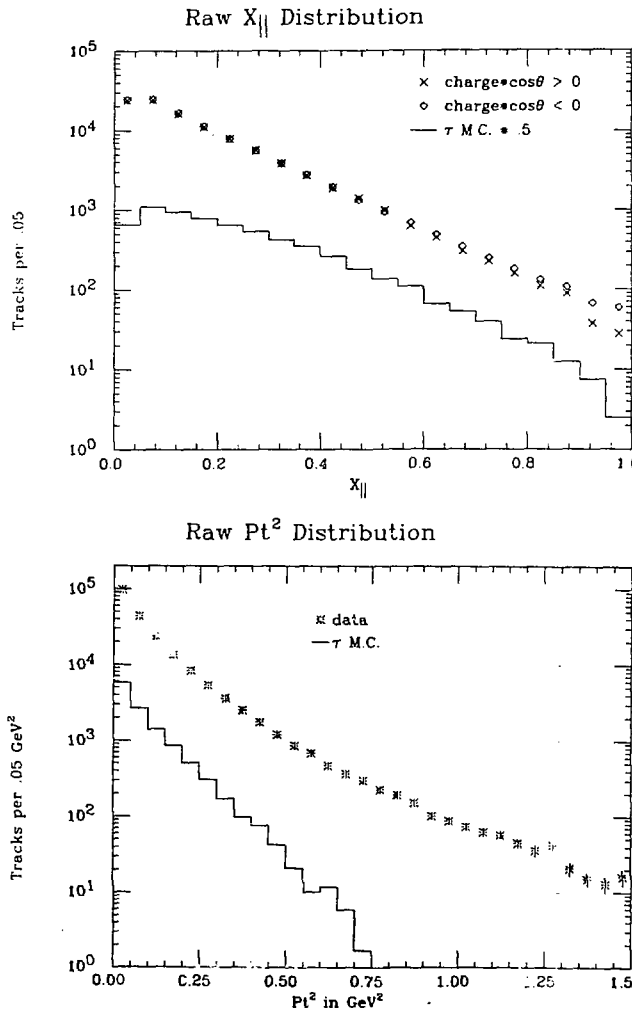

Figure 17: Raw Distributions in $X_{||}$ and Pt^2
a) Detected tracks per .05 $X_{||}$ for data (points) and Monte Carlo prediction for contribution from tau events (histogram). The data are plotted separately for charge*cosθ < 0 and > 0 to show the contribution at high $X_{||}$ from multi-prong Bhabha events.
b) Detected tracks per .05 Pt^2 (in GeV^2) for data (points) and τ Monte Carlo (histogram).

4.1 METHOD OF EFFICIENCY CALCULATIONS

The Monte Carlo was used to calculate corrections for the Mark 1 detection inefficiency, for the effects of initial state radiation, and for the error in determining the jet axis.

Each Monte Carlo event was passed through a simulation of the detector as described in Chapter 2 to obtain measured momenta. The Monte Carlo events were subjected to the same event selection criteria as were the data. The sphericity axis was found in the same way as for the data.

The details of the Monte Carlo simulation of initial state radiation are given in Appendix A. Events were generated with the correct center-of-mass energy distribution and given the corresponding Lorentz boost. It is conventional to display a given distribution as it would have been if there had been no radiation. Unfortunately it is not possible to eliminate the radiative events from the data since we measured neither the total hadronic energy nor the presence of a bremsstrahlung photon which in general traveled down the beam pipe. Instead we calculated the efficiency by comparing the Monte Carlo detected events to those Monte Carlo events which were produced with no radiation. Thus the radiation was in effect divided out.

The error in the jet axis was dealt with similarly: the momenta in detected events were relative to the measured jet axis; the momenta in produced events were relative to the produced jet axis.

Several models were used to choose the hadrons for the Monte Carlo. The efficiency was calculated for each one separately to check for model dependence in the result. The models are described briefly here. Greater detail is given in Appendices B and C.

The simplest model was the all-pion limited-transverse-momentum model. All particles were chosen to be pions. The multiplicity was chosen according to a Poisson distribution with the average (10.5) adjusted to reproduce the average momentum per particle observed in the data. The fraction of the pions that were chosen to be neutral (.5) was adjusted to reproduce the average observed charged multiplicity. Momenta were generated with the program GENIUS[19] according to Lorentz invariant phase space multiplied by a matrix element which limited momentum transverse to the jet axis:

$$|M|^2 = e^{-\mathrm{sum}\,(Pt^2 / R^2)}$$

---

[19] the SLAC version of the program described in D. C. Carey and D. Drijard, J. Comp. Phys. 28:327, 1978. The program is from a tape given to Roger Chaffee by D. Carey and slightly modified by Roger and myself.

The parameter κ was adjusted to reproduce the observed average transverse momentum (κ=0.55).

An alternate model was the udsc Feynman-Field model[20]. For the hadronic events the initial $q\bar{q}$ pair were chosen to be u, d, s, or c in ratios of the squares of their charges. Each was fragmented according to the Feynman-Field prescription. The two jets were joined and the momenta adjusted to achieve energy and momentum conservation. The fraction of strange quarks in the sea and the vector/pseudo-scalar ratio for the hadrons were adjusted to agree with the measured K^0 and ρ^0 fractions. The average transverse momentum of the sea quarks was adjusted so that the hadrons in the Monte Carlo reproduced the average hadron transverse momentum observed in the data. The remaining parameters of the model were left as specified by the authors. Particles decayed according to the standard values of their lifetimes and branching ratios.

A model intermediate between these two was the udsc limited-transverse-momentum model. The multiplicity and momenta were chosen as in the all-pion limited-transverse-momentum model. The particular hadrons were chosen to be pions, rhos, kaons, charmed particles, etc. as in the Feynman-Field model.

---

[20] A. Seiden, Phys. Lett. 68b:157, 1977.
A. Seiden, T.L. Shalk, and J.F. Martin, Phys. Rev. D 18:3990, 1978.
R. D. Field and R. P. Feynman, Nucl. Phys. B136:1, 1978.

Careful consideration must be given to the question of which particles should be included in the list of produced particles which were used in the efficiency calculations. This chapter is concerned with the measurement of charged particle momenta, but which charged particles? It would be unrealistic to pretend to be measuring charmed particle momenta when we observe only the decay products. A D^+ that decayed to $K^{*0}\rho^0$ is represented in the produced list by the resulting $K^-\pi^+\pi^+\pi^-$. On the other hand we must be careful to avoid double counting. If the K^- decayed the resulting muon would not also be included in the produced list, although it might be included in the detected list. In the case of a photon that converted in the beam pipe to an e^+e^- pair, the e^+ and e^- would not be included in the produced list. In summary, "charged particles" was interpreted to mean charged pions and kaons and prompt leptons.

The Monte Carlo was also used to generate $e^+e^- \longrightarrow \mu^+\mu^-$ events[21]. The resulting detected momentum distributions, normalized to the same luminosity as the data, were subtracted from the raw data. This magnitude of this subtraction is illustrated in Figure 17.

---

[21] The τ decay modes were: 23.0% $\rho\nu$, 22.6% continuum, 16.4% $e\nu\nu$, 16.0% $\mu\nu\nu$, 10.4% $\pi\nu$, 9.3% $A1\nu$, 1.5% $K^*\nu$, and 0.8% $K\nu$.

We present our momentum spectra normalized to the number of hadronic events. Thus the efficiency is the ratio of the track detection probability to the event detection probability, and can be greater than one. The final formula for a corrected momentum distribution is

$$C_i = \frac{d_i - t_i}{e_i \, (D - T) \, b_i}$$

where C_i = corrected $\frac{1}{N_{ev}} \frac{dn}{dx}$ in bin i

$e_i = \frac{o_i}{p_i} \frac{P}{O}$

d_i = # of detected tracks in bin i (data)

t_i = # of detected tracks in bin i (M.C.)

D = # of detected events (data)

T = # of detected events (M.C.)

b_i = bin size

o_i = # of detected tracks in bin i (hadronic M.C.)

p_i = # of produced $\pi^{\pm}, K^{\pm}$, and prompt $e^{\pm}$ and $\mu^{\pm}$ in bin i in events with no initial state radiation (hadronic M.C.)

O = # of detected events (hadronic M.C.)

P = # of produced events with no initial state radiation (hadronic M.C.)

4.2 MOMENTA PARALLEL TO THE JET AXIS

Despite cuts designed to eliminate multi-prong Bhabha events, some still remain in the data. These events are mostly forward scattering, so that the e^+ were mostly in the +z hemisphere and the e^- in the -z hemisphere. The contamination is obvious in Figure 17a where the raw X|| distribution is plotted separately for positive and negative values of charge*cosθ.

The data, subject to the requirement that charge*cosθ<0 (and multiplied by 2) and with the tau contribution removed, are shown in Figure 18 for three different conditions: (a) all tracks, (b) tracks in events where at least half of the nominal center-of-mass energy has been detected in charged tracks (assuming pion masses), and (c) tracks for which the opposite jet contains a track of X||>.5. The later two requirements reduce the error in the jet axis, and thus in X||, as demonstrated in Figure 19 where we plot for detected Monte Carlo tracks the scaled momentum parallel to the detected sphericity axis vs. the scaled momentum parallel to the true jet axis. Since the produced distribution used in calculating the efficiency is the same in all three cases, the bias by the opposite jet and visible energy cuts will be corrected for if the Monte Carlo is in sufficiently good agreement with the data. Superimposed on the data in Figure 18 are the results of the Feynman-Field Monte Carlo,

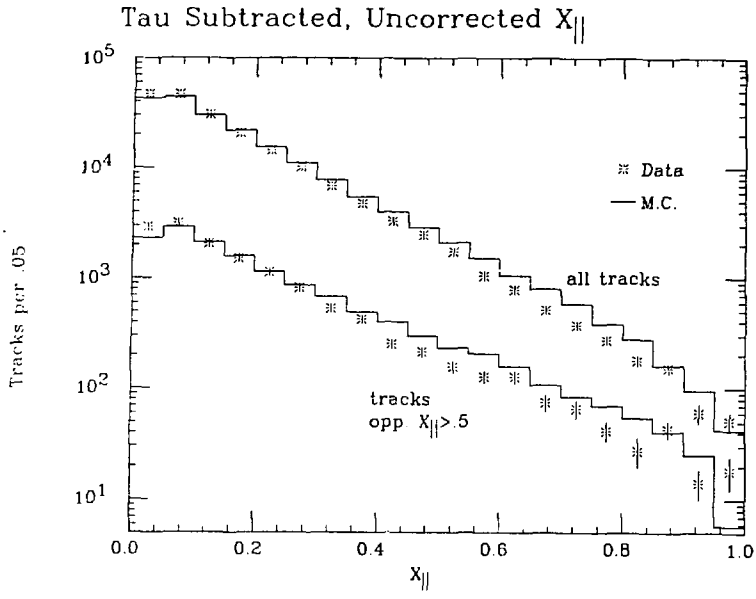

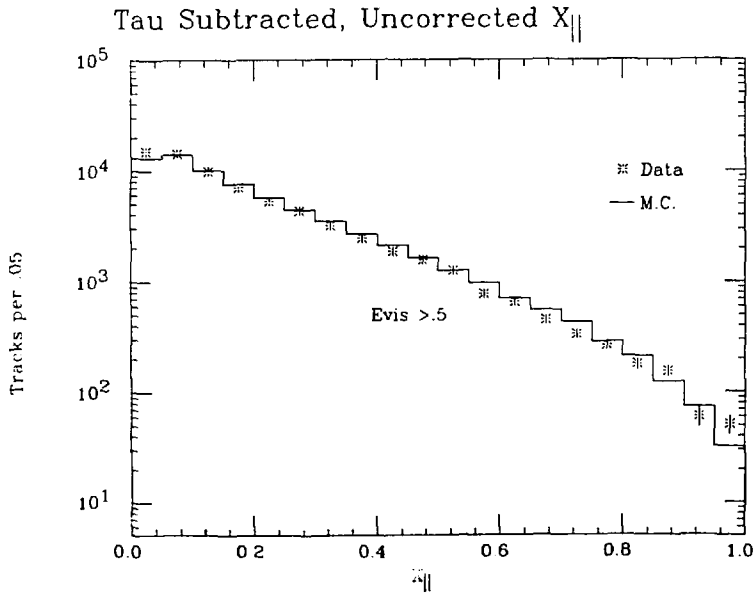

Figure 13: Uncorrected, Tau Subtracted $X_{||}$ for data and Feynman-Field Monte Carlo.

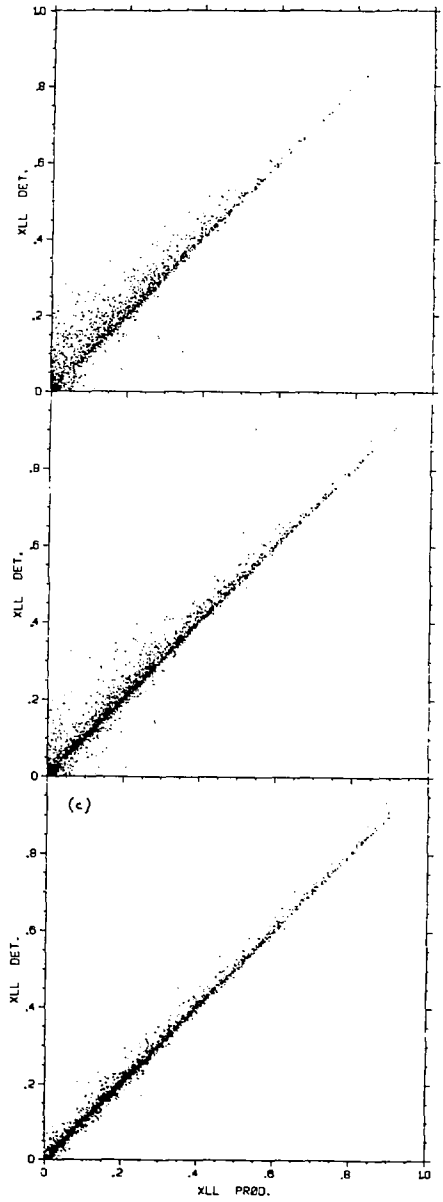

Figure 19: Error in $X_{\parallel}$ due to error in jet axis for (a) all events, (b) events in which at least half of the energy is detected, and (c) for tracks opposite a track of $X_{\parallel}>.5$.

normalized to the same number of tracks. The all-pion and udsc limited-transverse-momentum models gave similar results.

The efficiencies as a function of X|| are shown in Figure 20 for the three cases. we have calculated the efficiencies separately for the all-pion model and the Feynman-Field model. The disagreement between the two models was somewhat larger than the statistical error except at the highest momentum. we averaged the efficiencies from the two models and assigned errors which cover the range of disagreement.

The corrected distributions are shown in Figure 21. The results obtained using all events and using events with at least half of the energy detected are in good agreement, but differ from those obtained using tracks opposite a high momentum particle. Since the data and the Monte Carlo agreed better for the other two cases than for the requirement of a high momentum particle, we use only the results from all events and those with at least half of the energy detected in our final distribution. The results from those two methods were averaged and assigned errors which cover the slight disagreement between them. The values are given in Table 2.

The charged particles we have measured here come from many sources: various heavy particle decays as well as the primary vertex. We would like to separate out those coming

TABLE 2

$X_{\parallel}$

$X_{\parallel}$	1/Nev dn/d$X_{\parallel}$
.00 - .05	39. ± 4.
.05 - .10	24. ± 4.
.10 - .15	15. ± 2.
.15 - .20	9.5 ± 1.5
.20 - .25	6.7 ± 1.1
.25 - .30	4.8 ± 0.7
.30 - .35	3.4 ± 0.4
.35 - .40	2.5 ± 0.3
.40 - .45	1.8 ± 0.2
.45 - .50	1.39 ± 0.15
.50 - .55	1.07 ± 0.07
.55 - .60	0.66 ± 0.08
.60 - .65	0.53 ± 0.06
.65 - .70	0.35 ± 0.04
.70 - .75	0.28 ± 0.05
.75 - .80	0.24 ± 0.04
.80 - .85	0.16 ± 0.04
.85 - .90	0.18 ± 0.03
.90 - .95	0.10 ± 0.04
.95 - 1.0	0.13 ± 0.11

dn / d$X_{\parallel}$ per event for all charged particles

from the primary vertex, as it is those which reflect directly the quark fragmentation process, and to which discussions of scaling etc. apply. To do so would require subtracting charged particles from all other sources. In subsequent chapters we investigate K^0 and ρ^0 production. However there are many other possible sources which we are unable to measure. In particular, we know that charmed particle decays must contribute a substantial fraction of the charged particles we observe. We show the effect of charmed particles by plotting in Figure 22 the charged

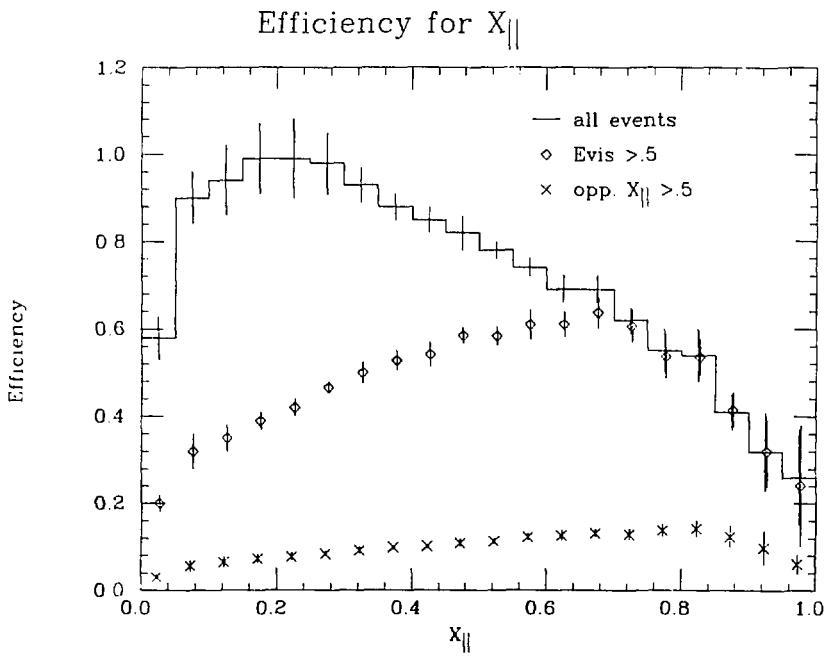

Figure 20: Efficiency for $X_{||}$

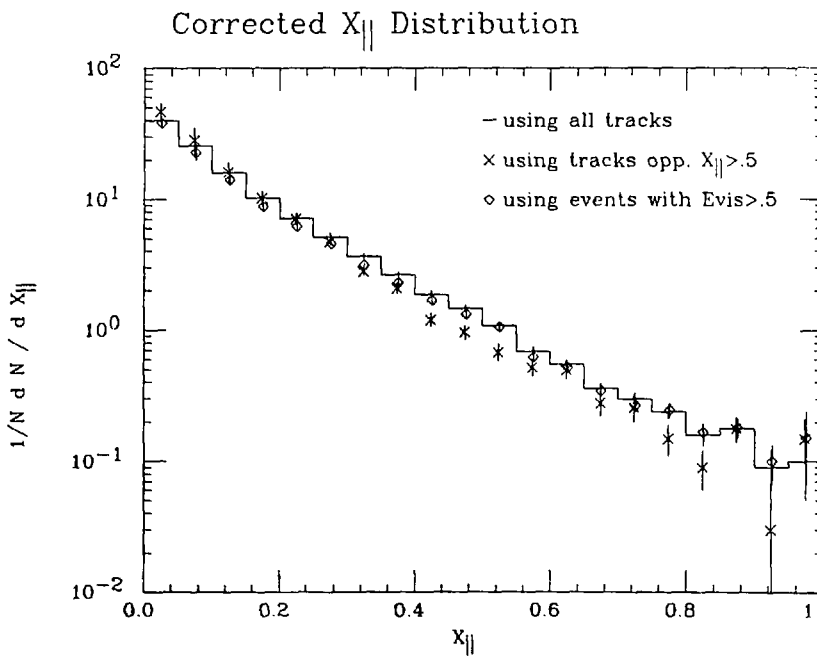

Figure 21: Corrected $X_{||}$ Distribution for final-state charged particles.

particle momentum distribution separately for events in which the primary quarks are charm and in which they are up, down, or strange. The two distributions are quite different, a difference we expect to be energy-dependent. This illustrates the importance of including heavy particle decays when testing a model of quark fragmentation. The effect of decays is shown again in Figure 23, where we compare the X|| distribution of all primary particles to that of the final state charged hadrons.

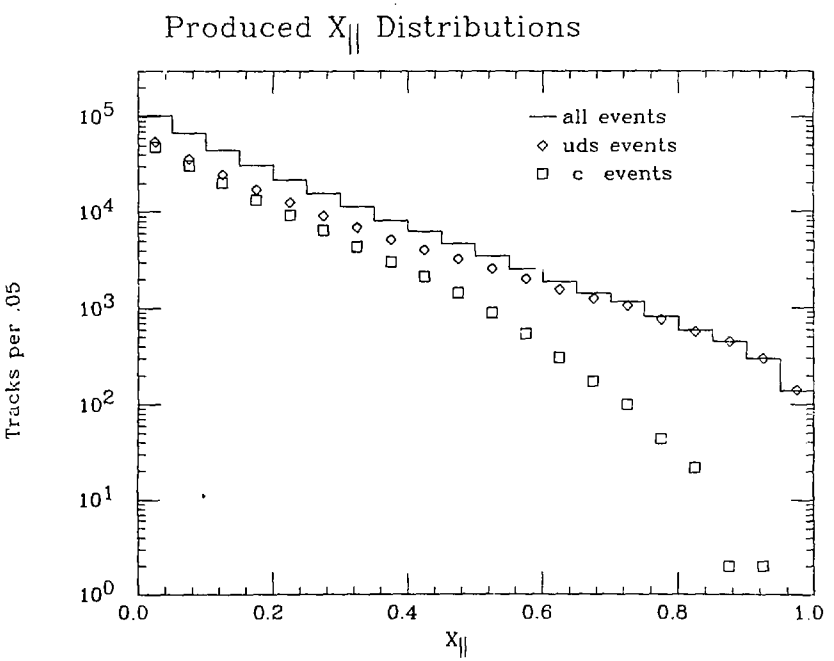

Figure 22: $X_{||}$ in Feynman-Field Model for final-state charged particles.

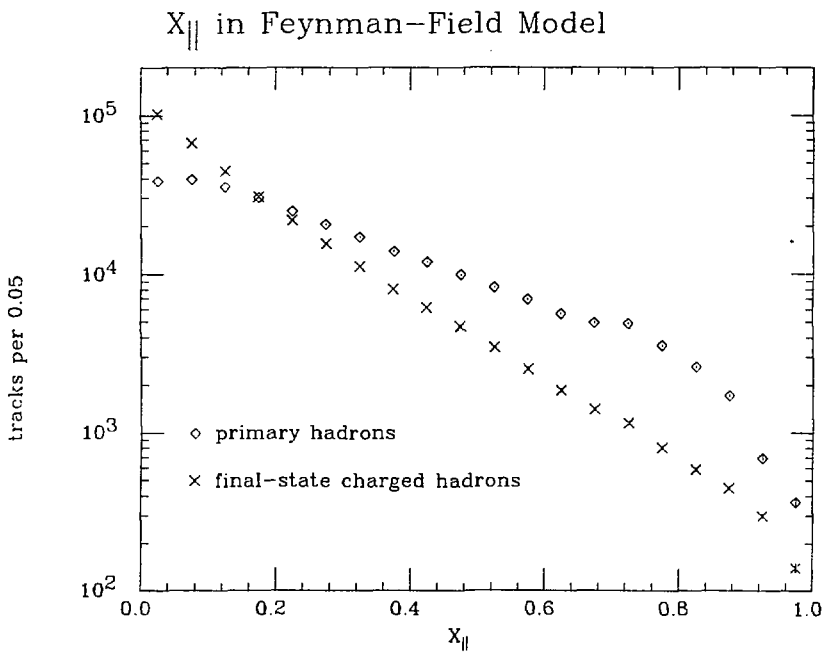

Figure 23: $X_{\|}$ of Primary Hadrons compared to $X_{\|}$ of final state hadrons in Feynman-Field Model.

4.3 MOMENTA TRANSVERSE TO THE JET AXIS

The raw distributions in Pt^2 measured relative to the sphericity axis are shown in Figure 17b for the data and the tau Monte Carlo. In Figure 24 we show the tau-subtracted data for the three cases: all events, events in which at least half of the energy was detected, and tracks opposite a track of $X||>.5$. Superimposed on the data are the detected distributions from the Feynman-Field Monte Carlo. In Figure 25 we compare the data to three different Monte Carlo models: the Feynman-Field model, the all-pion model with matrix element $|M|^2 = \exp(-Pt^2/.55^2)$, and the all-pion model with matrix element $|M|^2 = \exp(-Pt/.3)$. None of the three models gives really good agreement. The $Pt^2/.55^2$ model fits the low momentum region but falls below the data at high momentum. The other two models fit the high momentum region but are above the data near $Pt^2 = .5$ GeV^2.

The efficiency was calculated separately for the three models and the three data selection cases and the results compared. The efficiencies from the Feynman-Field model are shown in Figure 26. The three cases agreed well for the same model, but there was significant model dependence. The error bars in the final distribution, which is shown in Figure 27 and listed in Table 3, cover the variations seen. Since the errors are dominated by the model dependence, no improvement in precision can be made by combining bins. One

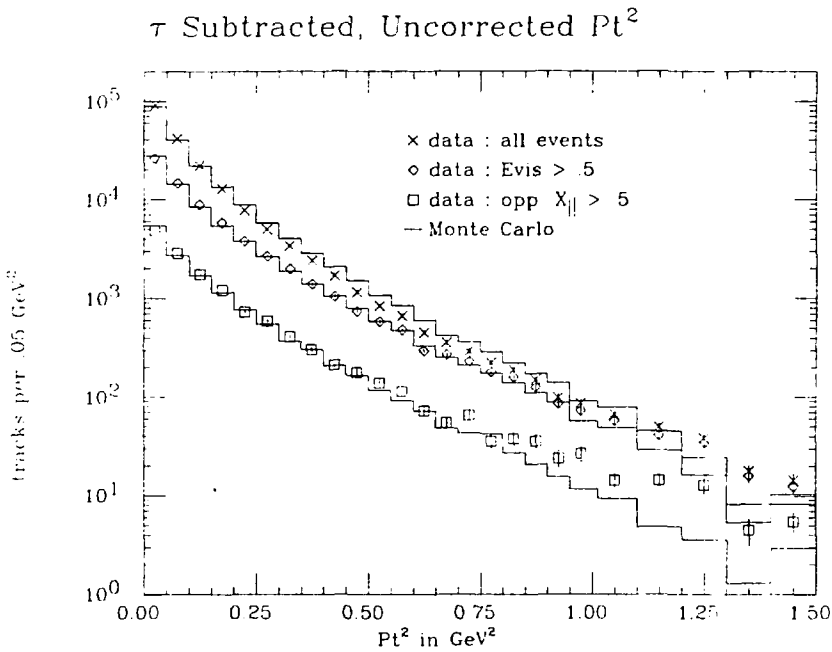

Figure 24: Tau subtracted, Uncorrected Pt^2

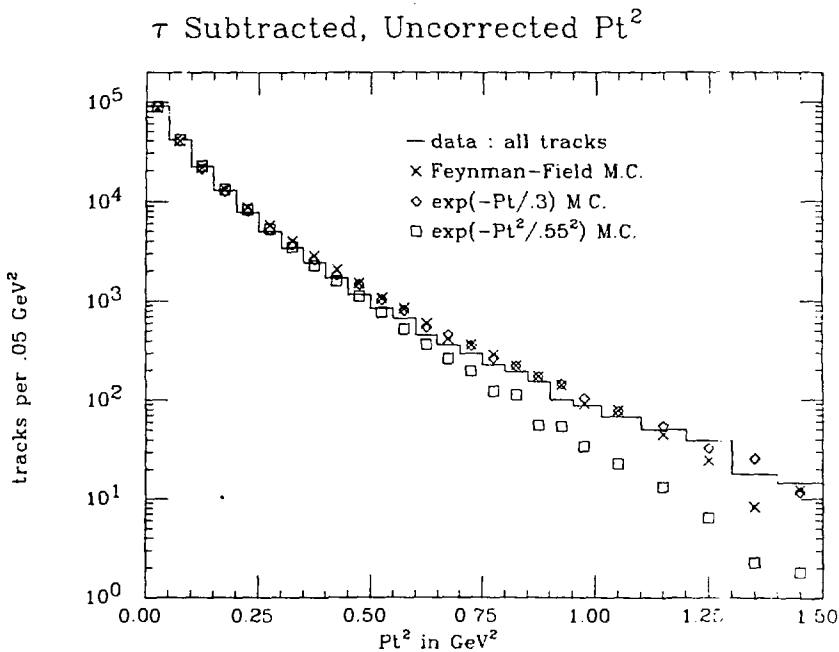

Figure 25: Comparison of Data and Monte Carlo. The Monte Carlo and the data have the same number of events. Thus the statistical errors, omitted on the graph for the sake of clarity, can be determined from the numbers themselves.

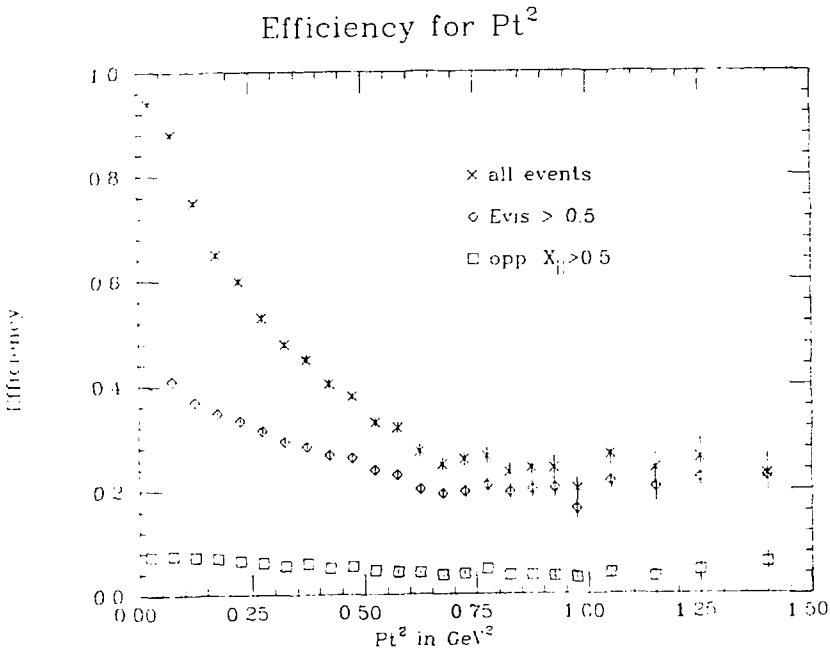

Figure 26: Efficiency for Pt^2 obtained using Feynman-Field model.

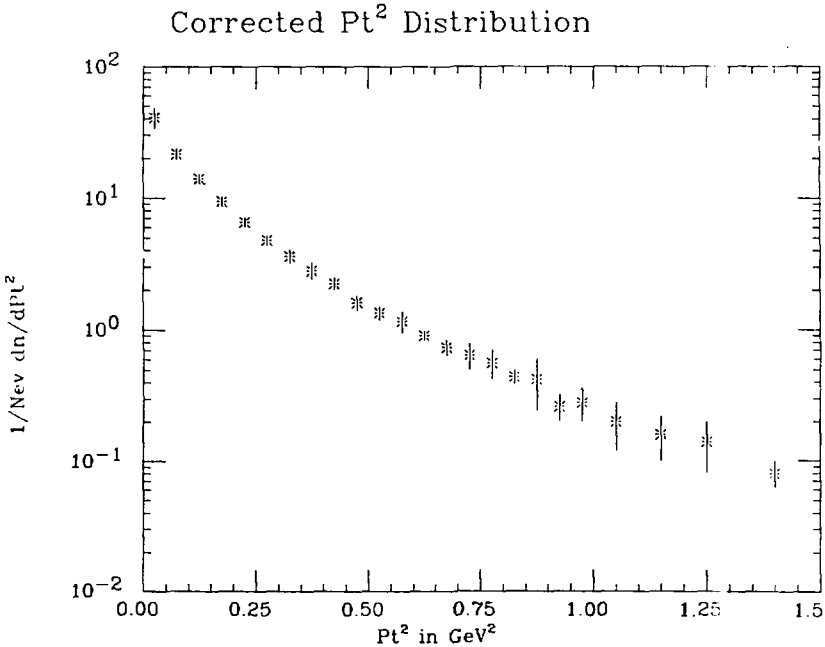

Figure 27: Corrected Pt^2 Distribution for final-state charged particles.

should also note that the track-by-track error on Pt^2 is very large, as shown in Figure 28, so that any small-scale structure in the true distribution would not be visible in the corrected distribution.

TABLE 3

Pt^2

Pt^2 (GeV^2)	$1/Nev\ dn/dPt^2$
.00 - .05	41. ± 7.
.05 - .10	21.6 ± 1.6
.10 - .15	14.0 ± 0.6
.15 - .20	9.4 ± 0.6
.20 - .25	6.6 ± 0.4
.25 - .30	4.8 ± 0.4
.30 - .35	3.6 ± 0.4
.35 - .40	2.8 ± 0.4
.40 - .45	2.2 ± 0.2
.45 - .50	1.6 ± 0.2
.50 - .55	1.3 ± 0.2
.55 - .60	1.2 ± 0.2
.60 - .65	0.90 ± 0.08
.65 - .70	0.74 ± 0.10
.70 - .75	0.64 ± 0.14
.75 - .80	0.56 ± 0.14
.80 - .85	0.44 ± 0.06
.85 - .90	0.42 ± 0.18
.90 - .95	0.26 ± 0.06
.95 - 1.0	0.28 ± 0.08
1.0 - 1.1	0.20 ± 0.08
1.1 - 1.2	0.16 ± 0.06
1.2 - 1.3	0.14 ± 0.06
1.3 - 1.5	0.08 ± 0.02

dn / dPt^2 per event for all charged particles

In Figure 29 we show the charged particle Pt^2 distributions from the Feynman-Field model for charmed and

non-charmed events separately. In this version[22] of the model, charmed particles always contain a primary quark. Since the primary quarks by definition have no transverse momentum, charmed particles are produced with lower average transverse momentum than most other primary vertex particles. However this difference is not visible in the charged particle transverse momenta, which are nearly the same in charmed and non-charmed events. In Figure 30 we compare the Pt^2 distribution for primary hadrons and for final state charged hadrons in the Feynman-Field model.

In this chapter we have measured the momentum parallel and perpendicular to the jet axis for final-state charged particles. In subsequent chapters we will compare the charged particle distributions to those for K^0s and ρ^0s, which are two of the possible sources for the charged particles we have observed here.

---

[22] The original proposal by Feynman and Field was to give the primary quarks some transverse momentum. Then all primary hadrons would have the same Pt distribution. However, since the direction of the primary quarks is by definition the true jet axis, our primary quarks always have 0. Pt.

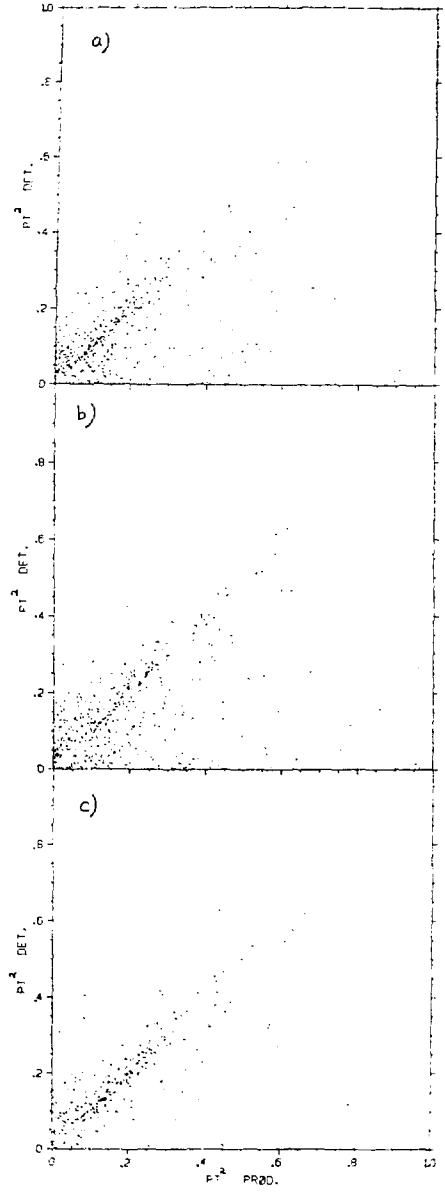

Fig. 28: Error in Pt^2 due to error in jet axis for (a) all events, (b) events in which at least half of the energy is detected, and (c) for tracks opposite a track of $x_{\parallel} > .5$.

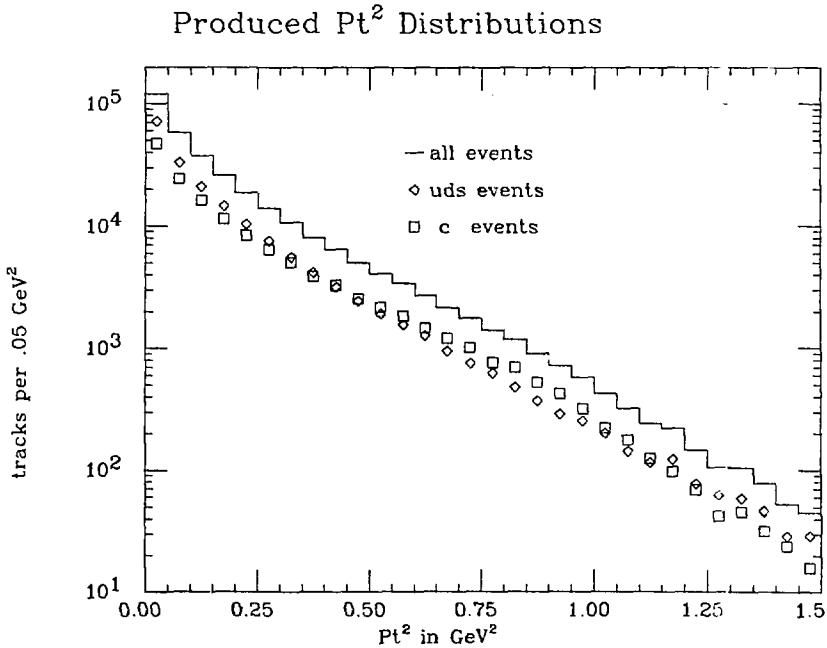

Figure 29: Pt^2 in Feynman-Field Model for final-state charged particles.

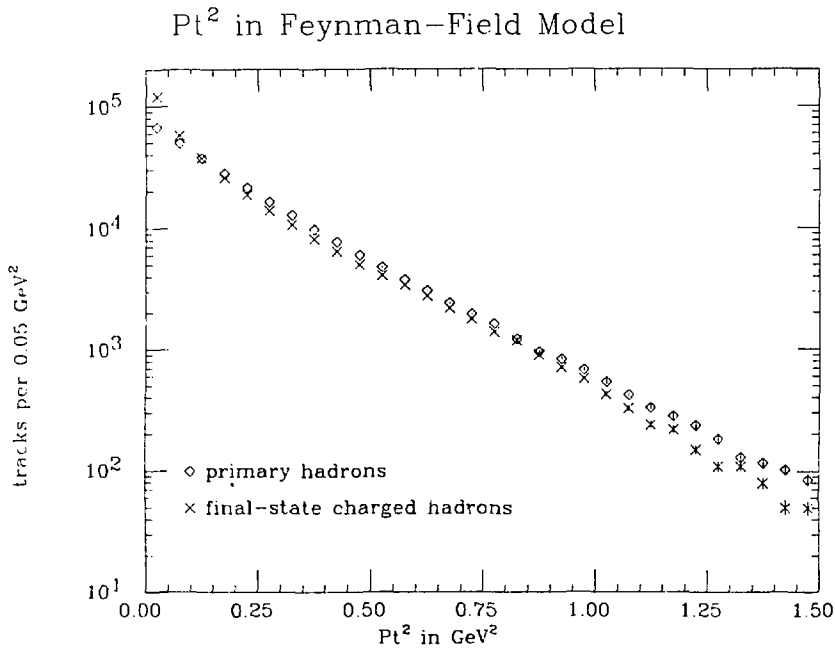

Figure 30: Pt^2 of Primary Hadrons compared to final state charged particles in Feynman-Field model.

Chapter V

K^0 PRODUCTION

The production of strange particles compared to that of non-strange particles gives us our only indication of the behavior of strange quarks compared to that of up and down quarks. Since the QED coupling of quarks to photons is proportional to the square of the quark charge, we expect the primary quark pair in e+e- annihilation to be up, down, strange and charmed in the ratio 4 : 1 : 1 : 4, so that only 10% of hadronic events start out with strange quarks. The 40% of events that start with charmed quarks will give strange particles in the charmed-particle decays, for a total of 50% of hadronic events with two strange quarks. Additional strange quarks may come from the sea. A common expectation[23] is that u,d,s and c quarks are pulled from the sea in the ratio 2:2:1:0. At an average multiplicity of 11 hadrons per event, this would give an average of approximately 5 strange particles per event. If no strange quarks were pulled from the sea there would be on average one strange particle per event. These expectations are subject to an error comparable to the discrepancy between

---

[23]for example Field and Feynman, Nucl. Phys. B136:1, 1978.

the expected and measured values of the total cross section: R = 2.0 vs. 2.6 below charm threshold and R = 3.33 vs. 4.3 at 7.3 GeV.

The cross section for inclusive kaon production has been measured by the Markl, Lead Glass Wall, DASP, and PLUTO collaborations.[24] These measurements in the form of

$$R_{K^0} = \frac{\sigma(e^+ e^- \longrightarrow K^0 X)}{\sigma(e^+ e^- \longrightarrow \mu^+\mu^-)} \quad \text{or} \quad R_{K^\pm} = \frac{\sigma(e^+ e^- \longrightarrow K^\pm X)}{\sigma(e^+ e^- \longrightarrow \mu^+\mu^-)}$$

are presented in Figure 31 as a function of the total center of mass energy. The region from 3.9 to 5.0 GeV, where the total cross section is rapidly varying, has been omitted for clarity. All groups have corrected for their detection efficiency. All but the PLUTO collaboration have corrected for the undetectable part of the momentum spectrum. The PLUTO collaboration estimated this loss to be 10%; their results have been increased by that amount before being included in Figure 31 . Only K_S can be detected; the total K^0 production is calculated with the assumption that an equal number of K_S and K_L are produced. Within the measurement errors, charged and neutral kaons are produced equally. In Figure 32 the charged and neutral data are combined to give the average number of kaons per event.

---

[24] Vera Luth et. al., Phys. Lett. 70B:120,1977.
Piccolo, Peruzzi, Rapidis et. al., Phys. Lett. 86B:220, 1979.
DASP collaboration: Brandelik et. al., Phys. Lett. 67B:363, 1977.
PLUTO Collaboration: Burmester et. al., Phys. Lett. 67B:367, 1977.

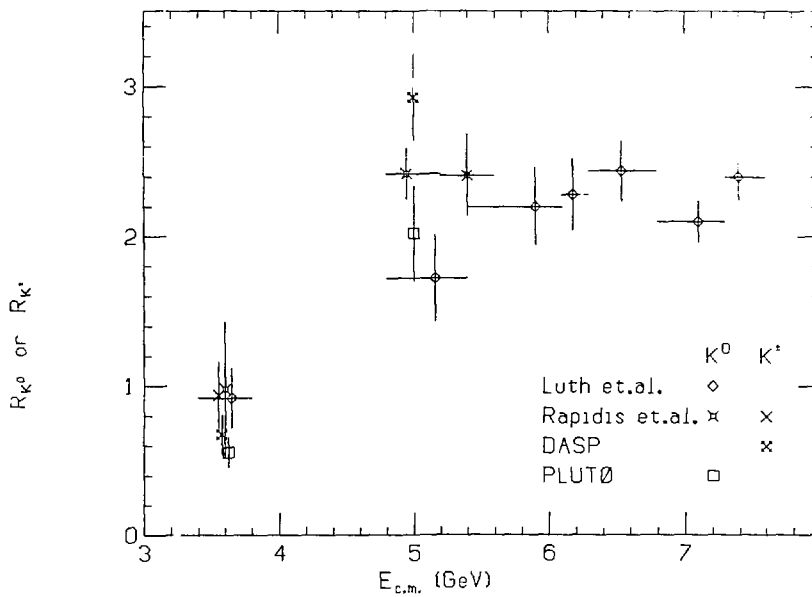

Figure 31: R(K) vs. center-of-mass energy (neutral and charged kaons separately).

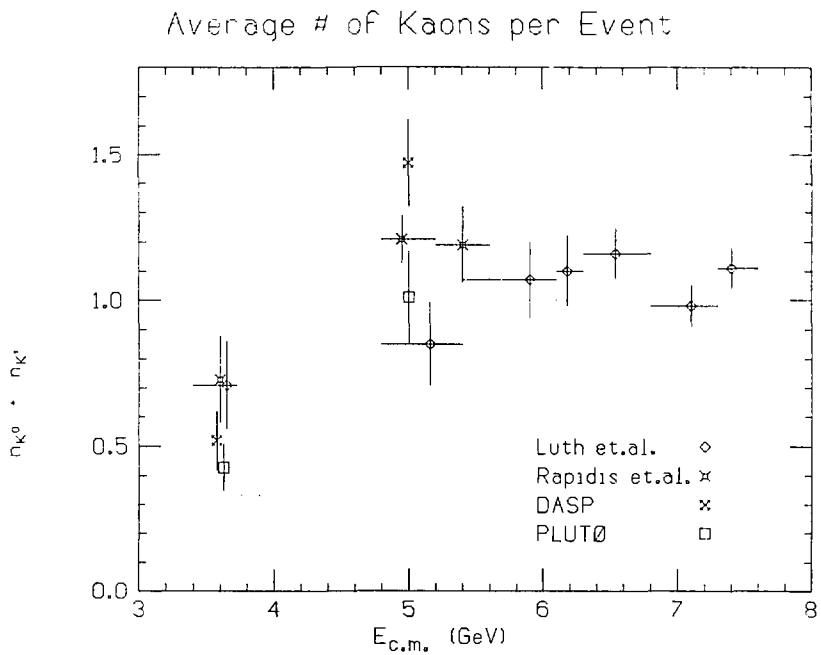

Figure 32: Average number of kaons per event vs. total center-of-mass energy (neutral and charged kaons summed). The dotted lines indicated the expected level of strange particle production from the primary s and c quarks alone.

below charm threshold 1/6 of the primary quarks should be strange so that the average number of kaons per event would be 1/3 if no strange quarks were pulled from the sea. The Mark I data point near 3.6 GeV includes the region of the 3.77 resonance. The other groups' points are taken at 3.6 GeV (although they are plotted here slightly to either side so they can be seen) and are therefore completely below charm threshold; the average measured value is 0.50 +/- 0.06. The Mark II collaboration has measured[25] the average number of lamdas (including anti-lamdas) to be 0.027 +/- 0.004 at 3.6 GeV. The kaons and lamdas together give 0.53 +/- 0.06 strange particles per event, which is above the 0.33 expected from the primary quarks alone, although the significance is questionable due to the disagreement between experiments. At 5 GeV the average measured kaon multiplicity is 1.16 +/- 0.06 and the average lamda multiplicity is 0.044 +/- 0.006. This sum is also somewhat higher than the 1.0 expected from the primary quarks alone.

It is interesting to estimate the relative probability of pulling a strange quark pair from the sea, although the result is subject to large errors due to the discrepancy in R and the uncertainty in the average hadron multiplicity. If all particles were pions, the total multiplicity would have to be approximately twice the charged multiplicity to

---

[25] G. S. Abrams et. al., Phys. Rev. Lett. 44:10, 1980.

account for the unobserved energy.[26] If resonance production were large, the number of hadrons at the primary vertex might be substantially less. In Table 4 the results are given for the extreme assumptions: 1) total multiplicity is twice the charged multiplicity, 2) total multiplicity is equal to the charged multiplicity.

TABLE 4

Estimate of Strange Sea Quark Fraction

Ecm (GeV)	3.6	5.0	7.3
N = 2 Nch	.013+/-.004	.011+/-.003	.005+/-.003
N = Nch	.030+/-.009	.026+/-.008	.011+/-.006

Errors quoted are statistical only. These results are strongly dependent on the assumption that 40% of primary quarks are charm and 10% are strange.

In Figure 33 we show the number of K^0s per event in the Feynman-Field model at 7.3 GeV as a function of the strange quark fraction in the sea. The model for D decay that we use in the Feynman-Field model produces slightly more neutral than charged kaons so that we get slightly more than 0.5 K^0 per event with no strange quarks in the sea. The

---

[26] J.L. Siegrist, SLAC-225 (thesis), 1979.

best agreement with the data is obtained with no sea quarks in this model. The average multiplicity at the primary vertex is 5.3 in this model, so that 20% strange sea component gives only 1.2 K^0s per event. This is a factor of two larger than the measured value of 0.53 +/- 0.03.

Despite the uncertainties involved, it is clear that the strange sea component is only a few percent, both above and below charm threshold.

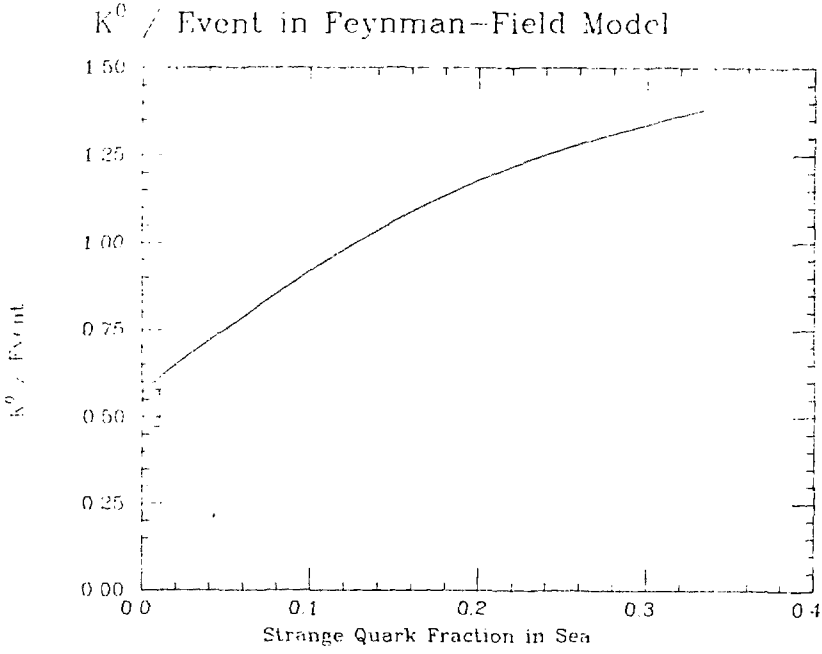

Figure 33: K^0 Production in Feynman-Field Model. The average number of K^0s per event in the Feynman-Field model at 7.3 GeV vs. the fraction of sea quarks that are strange. The measured value of 0.53 +/- 0.03 is indicated.

5.1 K^0 SELECTION

Simply making all $\pi^+\pi^-$ mass combinations gave a clear K^0 signal over a large background (Fig. 34). This background was considerably reduced by taking advantage of the finite K^0 lifetime. A 200 MeV/c K^0 travels an average of 1 cm before decaying and a 3 GeV/c K^0 travels an average of 16 cm; both are large compared to our vertex reconstruction resolution of a few millimeters.

All pairs of oppositely charged tracks were examined. The tracks were projected onto the xy plane and the two points of intersection of their two circles were found. If the tracks didn't intersect in xy projection the pair was discarded as a K^0 candidate. Since the increased resolution contributed by the proportional chambers was essential to the K^0 analysis, any intersection lying outside the first proportional chamber was discarded. Only .1% of the pairs had two intersections remaining; for those cases the one at the smaller distance from the beam was used.

The individual track momenta at the K^0 vertex were calculated. If the K^0 vertex was inside the beam pipe, corrections were made for the expected energy loss in the pipe. The K^0 momentum vector and mass and the position vector of the K^0 vertex relative to the beam were calculated.

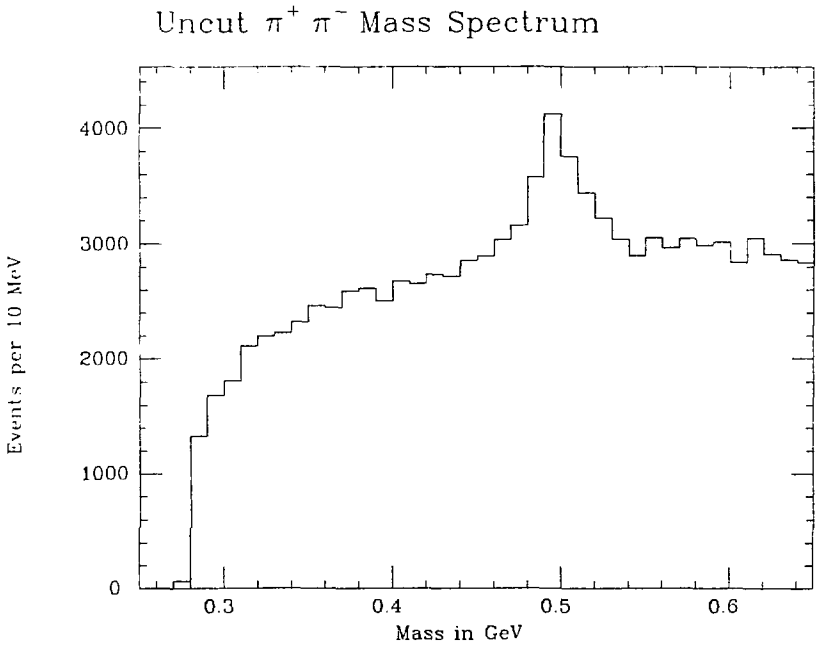

Figure 34: Uncut $\pi^+\pi^-$ Mass Distribution

Pairs with mass between .48 and .52 MeV were used as K^0s and side-bands of .44-.46 and .54-.56 MeV were used for the background subtraction.

A K^0 candidate was kept only if the distance in xy projection of the K^0 vertex from the beam was greater than 1 cm and also greater than 3 standard deviations from 0.0. The standard deviation was calculated from the opening angle δ between the two tracks and the position error per track of 1 mm:

$$\sigma = 1 \text{ mm} / (\text{sqrt}(2) * \sin(\delta))$$

This radius cut removed 67% of the background and 31% of the signal.

The position and momentum vectors were required to be parallel to within 90 degrees. This cut alone removed 50% of the background and 8% of the signal. A tighter cut on the angle would give a somewhat lower but less flat background. The angle and radius cuts together removed 83% of the background and 34% of the signal. The data with both of these cuts are shown in Figure 35. After all the cuts, 2197 K^0s are left in the peak.

The cuts used above are illustrated in Figure 36 by plotting the cut quantity separately for the background-subtracted K^0 and for the background region. The radial and z position of the primary vertex for events containing K^0s are shown in Figure 37 to demonstrate that

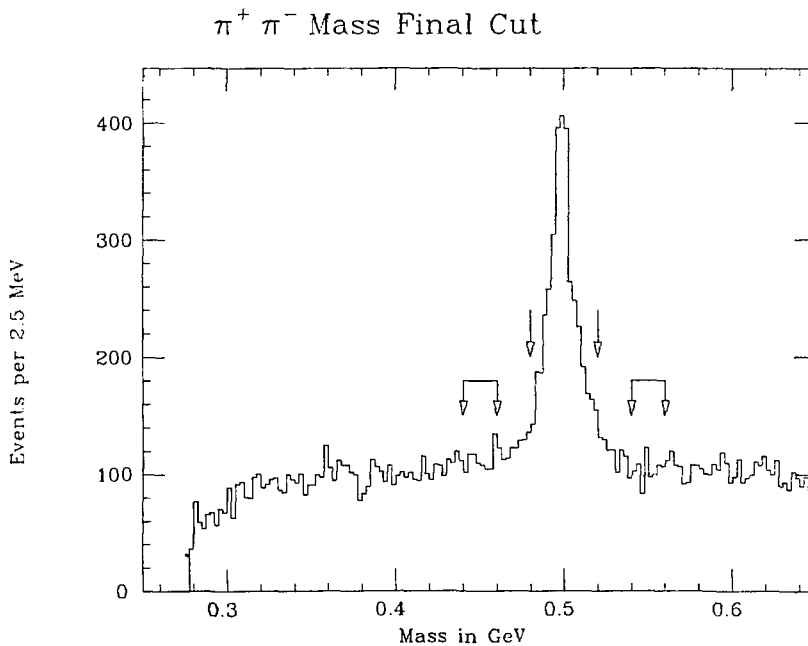

Figure 35: $\pi^+\pi^-$ Mass Distribution with Final Cuts

the K^0 decay products (which were included in the primary vertex fit) did not pull the primary vertex outside our cuts of 4 cm and 10 cm respectively.

Events with their primary vertex within 10 cm in z from the beam crossing point were used as signal. Those between 20 and 30 cm away were subtracted as background.

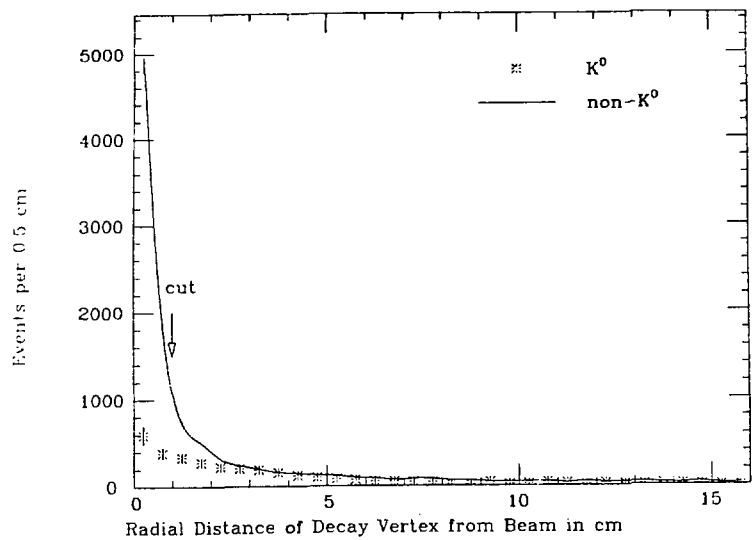

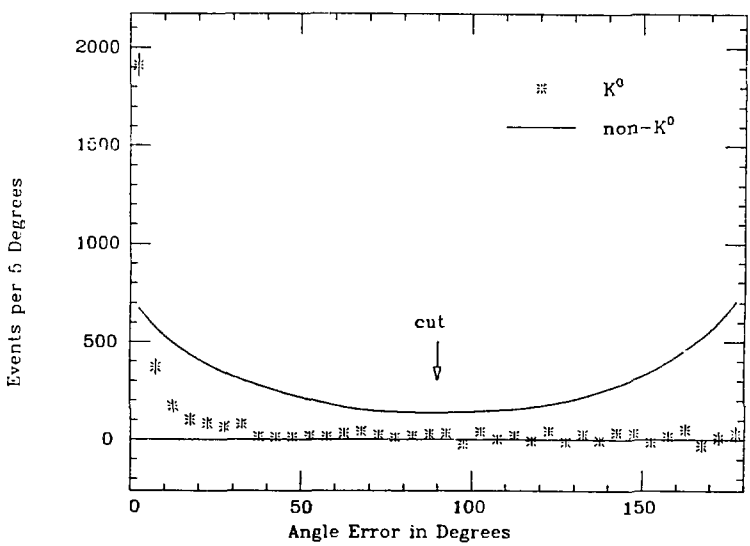

Figure 36: Plots of cut quantities for background-subtracted K^0 and for side-bands:
a) radial distance of decay vertex from beam.
b) angle between position and momentum vector.

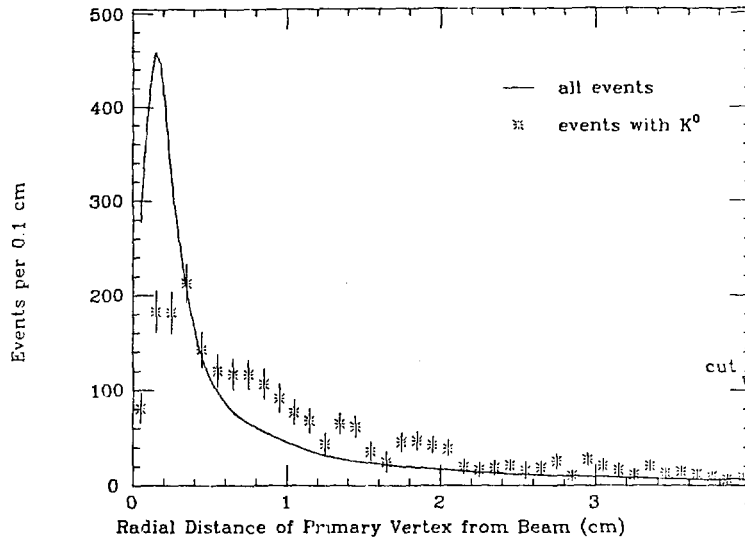

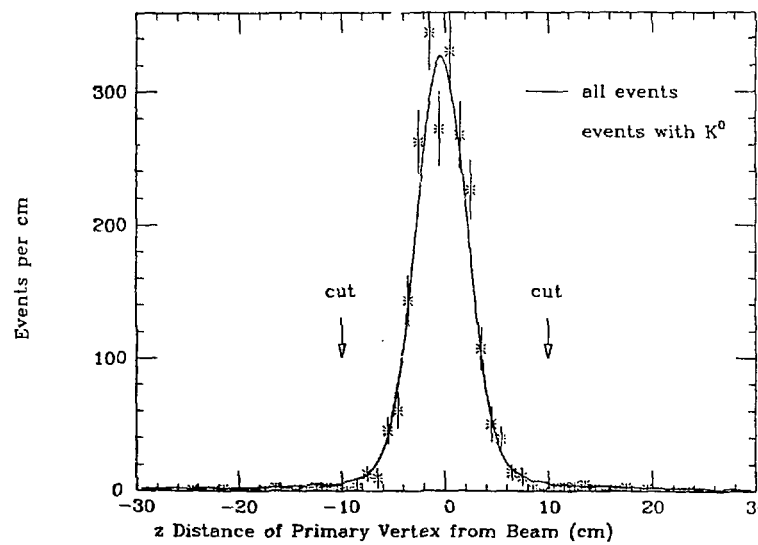

Figure 37: Primary vertex position for events containing a K^0 and for all events:
a) radial distance of primary vertex from beam.
b) z position of primary vertex.

5.2 K^0 MOMENTUM DISTRIBUTIONS

The momentum parallel and perpendicular to the jet axis was calculated for each $\pi^+\pi^-$ pair. Background-subtracted distributions of K^0 momenta were made by plotting $X||$ and Pt^2 with amplitude +1 for each pair with mass in the signal region (.48-.52 GeV) and with amplitude -1 for each combination in the side-bands (.44-.46 and .54-.56 GeV).

Two models for K^0 production were used to calculate the K^0 detection efficiency. The first was the Feynman-Field model, in which the strange sea quark fraction was set to 2% in approximate agreement with the data. The second was a modified version of the all-pion limited-transverse-momentum phase space model in which each event contained one K^0. Events were generated with each model and subjected to the same K^0 selection criteria as the data. The efficiency included the effects of initial state radiation and the error in the jet axis, as described in detail in the previous chapter. The two models agreed within the statistical errors for the efficiency as a function of $X||$. The was disagreement as large as 20% in some regions of Pt^2; the error bars were increased accordingly. The results from the two models were averaged and are shown in Figure 38.

The corrected K^0 distributions in $X||$ and Pt^2 are compared to those for all charged particles in Figure 39. (The charged particle distributions were divided by 10 for

convenience in comparison.) Above $X_{||}=.15$ and $Pt^2=.2$ GeV^2 the K^0 and charged particle distributions have roughly the same slope. The entire K^0 Pt^2 distribution is well fit by the form

$$d\,n\,/\,d\,Pt^2 = A\,\exp\,(-B\,Pt^2)$$

with B=4.6 +/- 0.2. This is in good agreement with the B=4.3 +/- 0.5 found in e^- p scattering.[27] Such agreement is surprising, since the e^- p data is below charm threshold, while most of our K^0s come from charmed particle decays. The K^0 distributions are in good agreement with the Feynman-Field model, as shown in Figure 40. However, one should note that since most of the K^0s come from D decay, this is as much a test of the D decay model as of the Feynman-Field model.

In Figure 41 we compare the momentum distributions in the Feynman-Field model of K^0s in events in which the primary quarks are (a) u or d, (b) strange, and (c) charm.

---

[27] I. Cohen et. al., Phys. Rev. Lett. 40:1614, 1978.

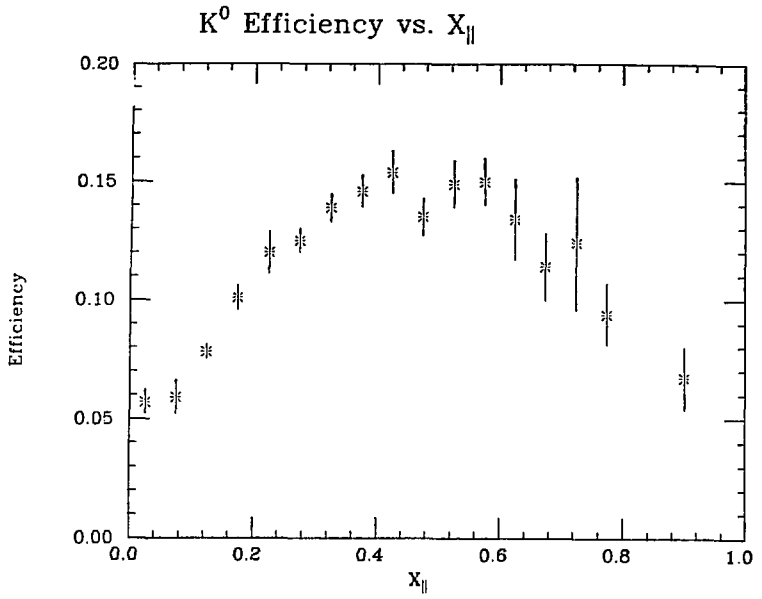

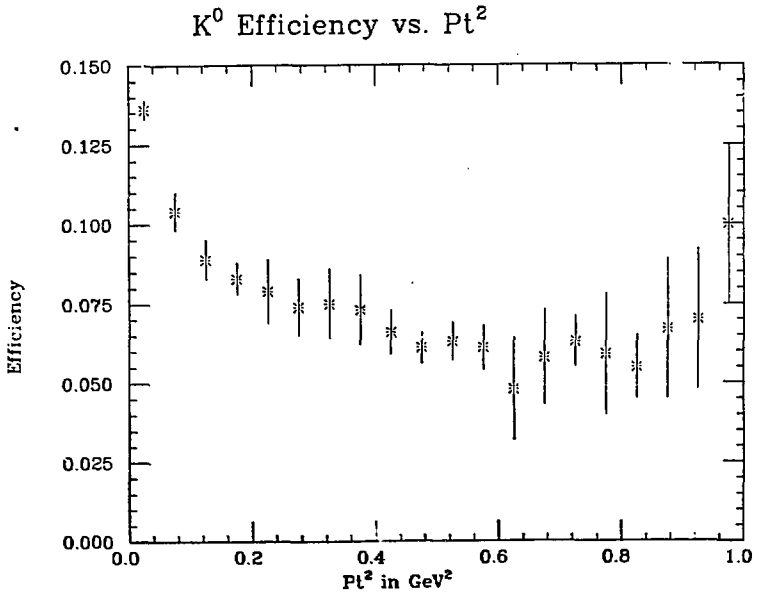

Figure 33: K^0 Efficiency as a function of $X_{||}$ and Pt^2.

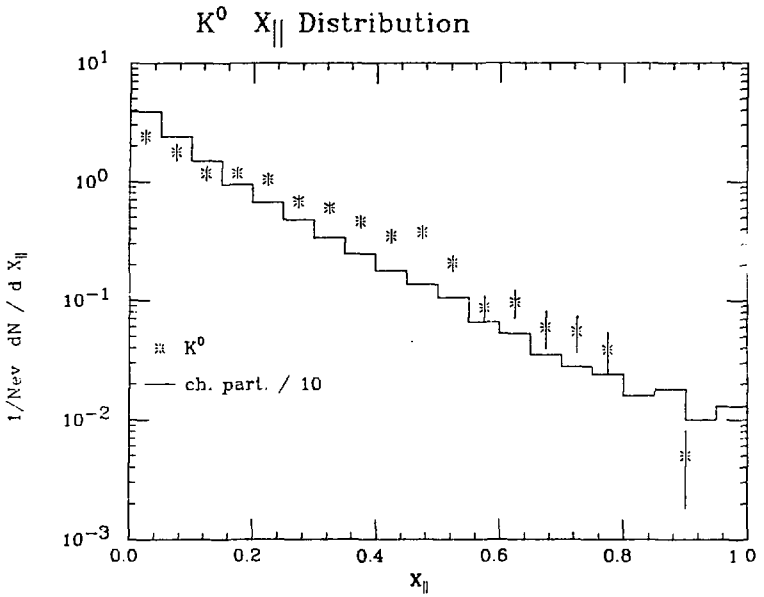

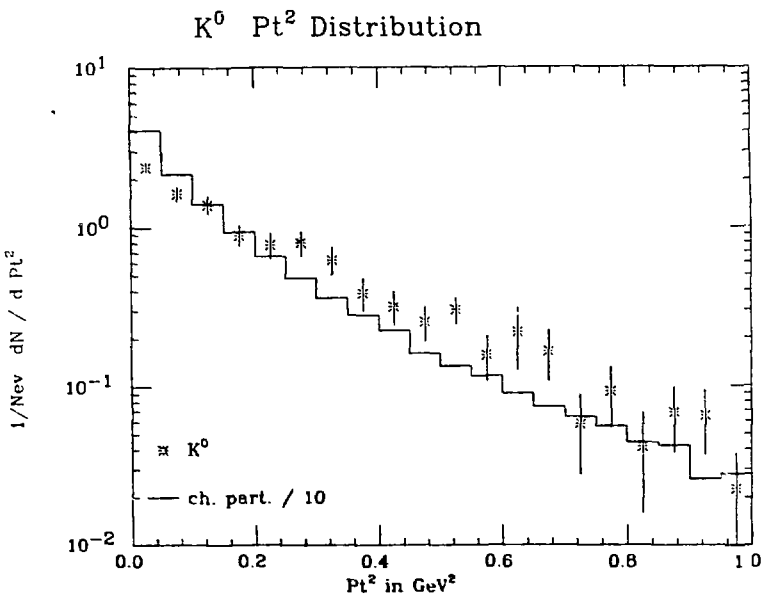

Figure 39: K^0 Momentum Distributions corrected for detection efficiency, initial state radiation, and jet axis errors.

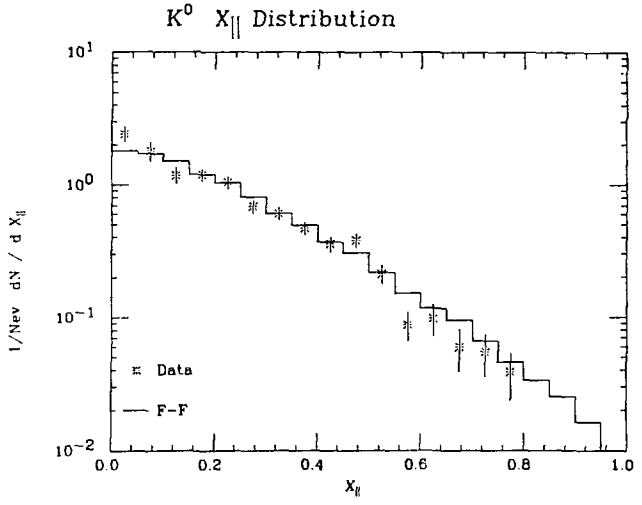

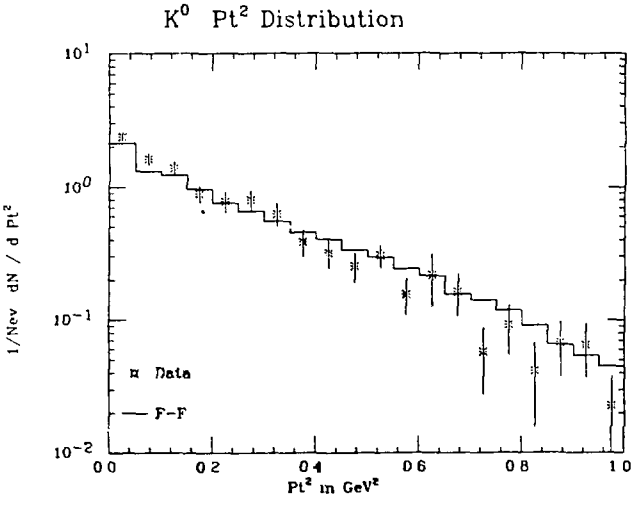

Figure 40: K^0 Momentum Distributions for data (points) and Feynman-Field model (histogram).

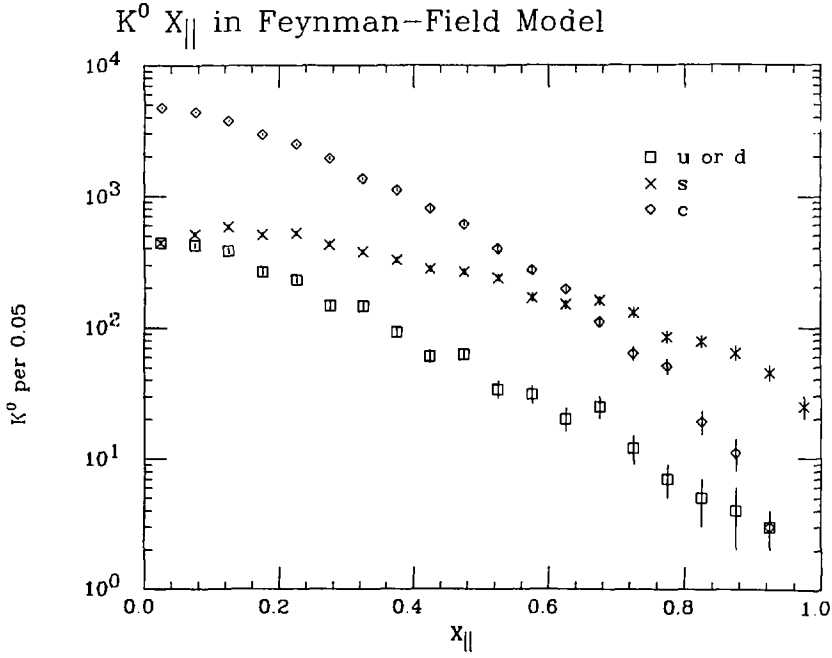

Figure 41: K^0 Sources.
K^0 momentum distributions from events in which the primary quarks are (a) u or d, (b) s, (c) c.

Chapter VI

ρ^0 PRODUCTION

When the available energy is large compared to a pion or a rho mass one might expect pion and rho production to be approximately equal. Naive spin statistics suggest that spin 1 particles would be produced three times as frequently as spin 0 particles. Measurement of rho production is one step towards any eventual understanding of fragmentation of quarks into hadrons. It may also have a significant impact on any study of charge correlations or leading particle effects, which can be created or diluted by resonance decays. Since high statistics are required for measurement of rho production, it will be some time before the work presented here can be replaced by results at higher energy.

Measurements were made of the average number of ρ^0s per event and of the ρ^0 X|| and Pt^2 distributions. The ρ^0 was observed in its decay to $\pi^+\pi^-$. All charged particles were assumed to be pions and the invariant mass was calculated for all pairs of opposite sign. The resulting mass distribution is shown in Figure 42a. The mass distribution was also plotted separately for 10 bins in X|| of the di-pion system from 0.0 to 1.0 and 10 bins in Pt^2 from 0.0 to 1.0 GeV^2. Then adjacent bins in which the signal was weak

were combined to allow a statistically significant result. The mass distributions for the final choice of bins are shown in Figure 42b-1.

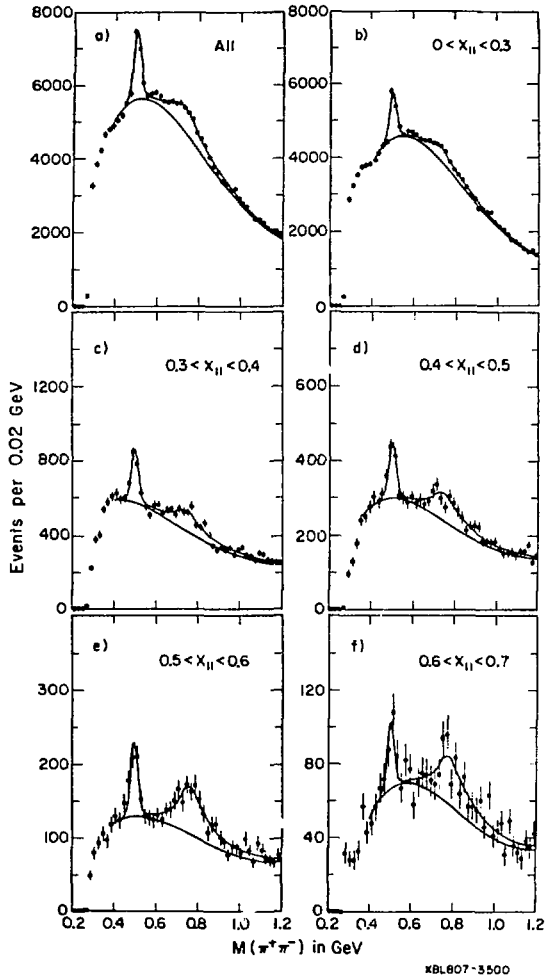

Figure 42: $M(\pi^+\pi^-)$ for various mass bins. The histograms are the data. The curves are the results of fitting the data to a polynomial background + Gaussian K^0 peak + Breit-Wigner ρ^0 peak (Method 3).

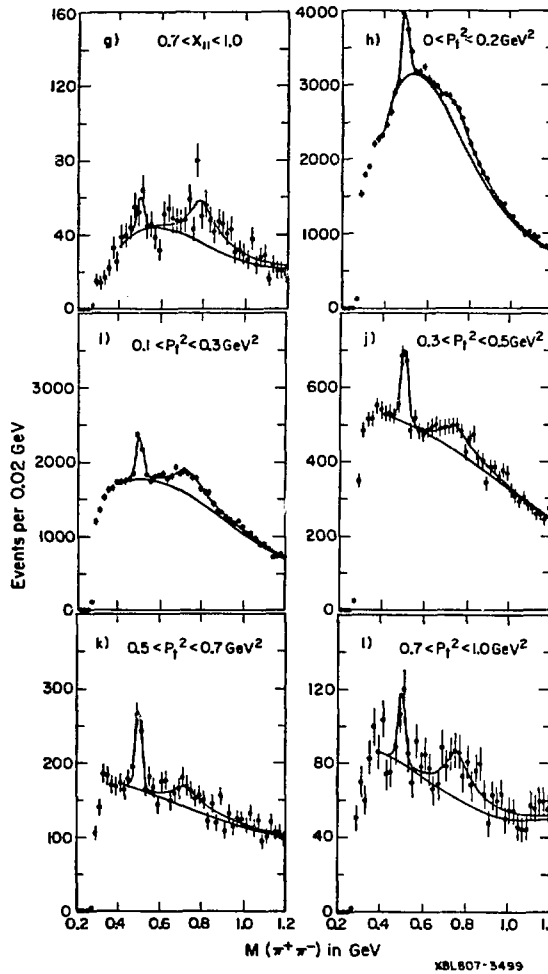

Figure 42: $M(\pi^+\pi^-)$ for various mass bins. The histograms are the data. The curves are the results of fitting the data to a polynomial background + Gaussian K^0 peak + Breit-Wigner ρ^0 peak (Method 3).

6.1 BACKGROUND DETERMINATION

The large width of the ρ^0 and the large background under it make the determination of the shape of the background both difficult and important. Several methods were tried and the resulting ρ^0 yields compared. The good agreement between methods gives confidence in the result.

6.1.1 Method 1

One would like to measure the background from the data itself. One possibility is the mass distribution of same sign pion pairs. Another is the mass distribution of opposite sign pairs, one of which has been rotated through an arbitrary angle (restricted to be within the solid angle of the detector). The first of these is necessarily biased towards high multiplicity events by the requirement of charge conservation; the second lacks the restrictions of momentum conservation. A distribution that avoids these difficulties, but also lacks the connection with reality, is the $\pi^+\pi^-$ mass distributions obtained from the Feynman-Field Monte Carlo. This model includes production of several resonances, some of which may produce peaks in the $\pi^+\pi^-$ mass distribution. For example, the $K^{*0}(890)$ appears as a peak near 670 MeV. In order to obtain the background from this model we have excluded the true ρ^0 signal from the $\pi^+\pi^-$ distribution; all other combinations were included.

Each of the three background forms was used in turn and the results were compared. In each case the background was normalized to the data in the region .9 to 1.2 GeV and then subtracted from the data. None of the three background forms is good enough to leave behind only a ρ signal; however they do take out most of the background. The same-sign background is compared to the data in Figure 43.

The subtracted data was then fit with a Breit-Wigner plus a first or second degree polynomial to accommodate the remaining background. The form of the Breit-Wigner used was[28]

$$BW = \frac{2}{\pi} \frac{M_0 M \Gamma}{(M^2 - M_0^2)^2 + (M_0 \Gamma)^2}$$

with

$$\Gamma = \Gamma_0 (M_0/M) (k/k_0)^3$$

where M_0 is the nominal ρ mass and Γ_0 its nominal width; k is the momentum of the pion in the ρ center-of-mass when the ρ has mass M; k_0 is that momentum at mass M_0.

The fit obtained with the same-sign pion subtraction is shown in Figure 44a with a straight line background and in Figure 44b with a quadratic background. In these fits the ρ

---

[28] J.D. Jackson, Nuovo Cim. 34:1644, 1964.

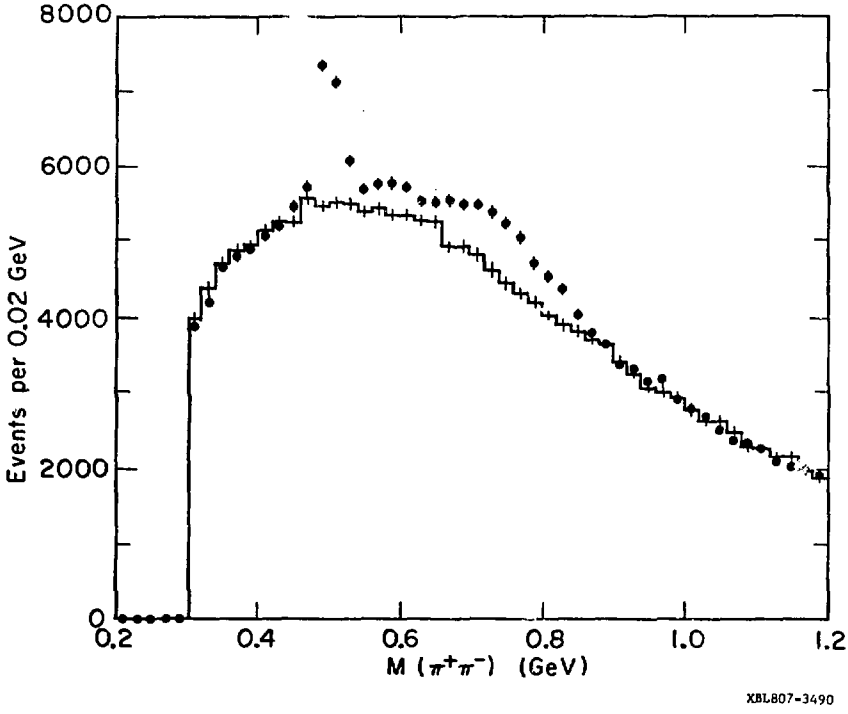

Figure 43: Same-Sign Background (histogram) normalized to the $\pi^+\pi^-$ mass distribution (points) in the region .9 to 1.2 GeV.

mass and width were fixed at the standard values of 776 and 155 MeV respectively. It is clear that the observed ρ has a lower mean mass. Allowing the mass to vary gives a best fit value of 746 +/- 5 MeV (Figure 44c). This discrepancy is present throughout this analysis, although the preferred mass increases somewhat with the momentum of the ρ. Since the K^0 shows no such deviations, the effect cannot be due to a problem with the momentum scale or the energy loss corrections. Further discussion of the mass problem is given in a later section.

Fits were performed in each of the momentum bins with each of the three background forms, with the ρ mass fixed and variable, and with first and second degree polynomials added to the Breit-Wigner. The results were averaged and assigned errors that encompass the variations found from fit to fit.

6.1.2 Method 2

Several previous measurements[29] have used an exponential background which also multiplies the Breit-Wigner peak. The data above 560 or 600 MeV were fit with the form

$$\exp (-B M - C M^2) * (A + D BW)$$

---

[29] for example:
Deutschmann et. al., Nucl. Phys. B103:426, 1976.
Higgins et. al., Phys. Rev. D19:65, 1979.

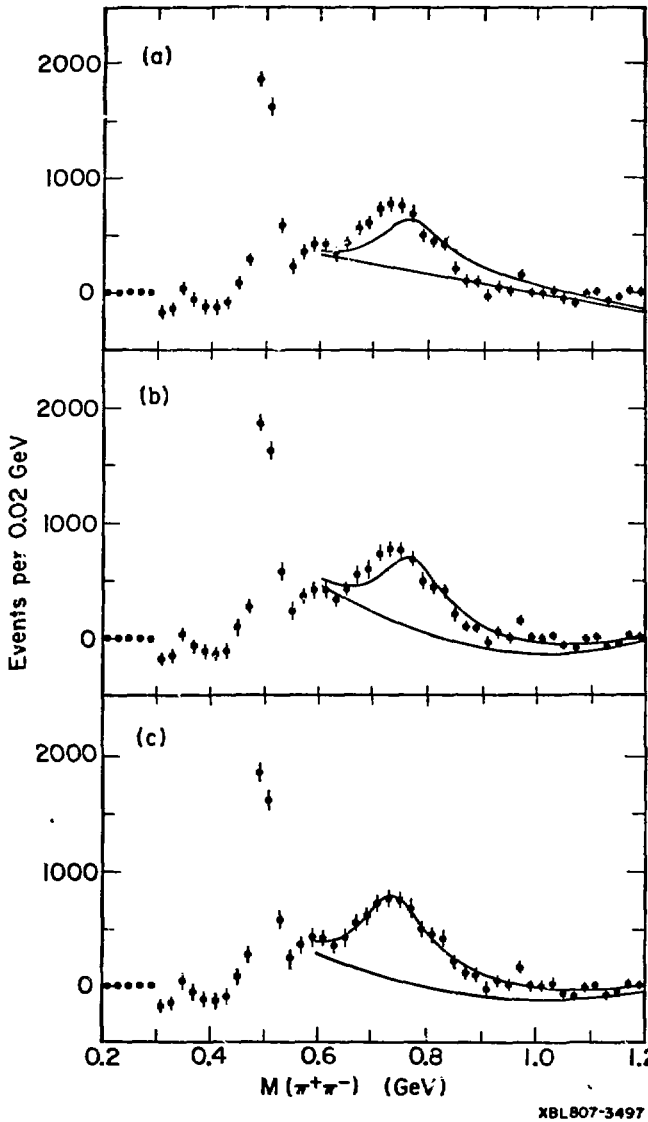

Figure 44: Fits to ρ mass with same-sign background. The histograms are the M($\pi^+\pi^-$) data with the same-sign pion pair background subtracted. The curves are the results of the fits as described below:
a) straight line background and ρ mass fixed at 776 MeV.
b) quadratic background and ρ mass fixed at 776 MeV.
c) quadratic background and ρ mass free.

where BW is the Breit-Wigner form as given above and A,B,C and D are free parameters of the fit. This form deviates from the data rapidly below about 600 MeV. The fit is improved if the data is first corrected using the mass-dependent efficiency obtained with the all-pion Monte Carlo. Therefore this correction was made for each momentum range and fits were performed between 600 and 1200 MeV.

The multiplying of the Breit-Wigner by the background is intended to approximate the effect of the phase space suppression of the production of high-mass ρs. The peak of the Breit-Wigner is shifted down slightly, but not enough to agree with the data using a nominal mass of 776 MeV. In Figure 45 fits are shown with the ρ mass fixed at 776 MeV (a) and allowed to vary (b). The best fit value was 753 +/- 5 MeV.

The stability of the fits was investigated by repeating them with different starting values and by varying the mass range of the fit. Errors were assigned which covered the range of variation seen from fit to fit as well as the statistical error.

The efficiency obtained from the all-pion Monte Carlo is not necessarily a good representation of the ρ^0 efficiency. Therefore we multiply the results obtained in this section by the all-pion efficiency to give raw ρ^0 yields which can be compared to those obtained with the other methods.

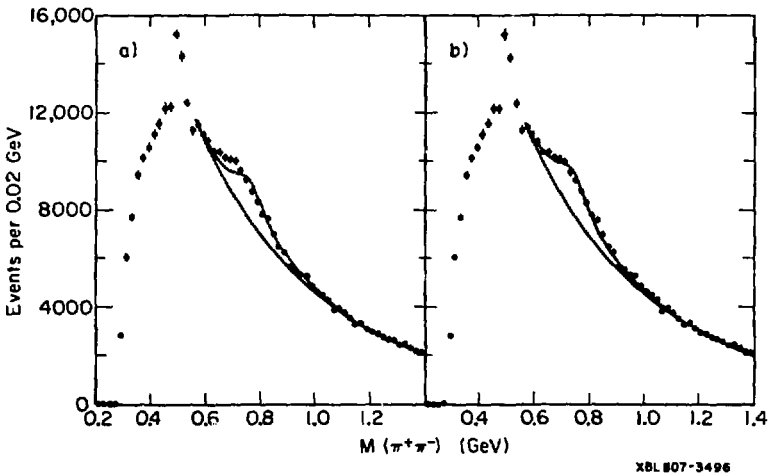

Figure 45: Fits to ρ mass with exponential background. The histograms are the efficiency-corrected data for all pairs. The fits were performed according to method 2.
a) ρ mass fixed at 776 MeV.
b) ρ mass free.

3.1.3 Method 3

It was decided that a more flexible background shape which could carry the fit below the K^0 was needed. The mass range from 340 to 1200 MeV was fit with a fourth order polynomial background plus a Gaussian K^0 peak and the Breit-Wigner ρ^0 peak. The polynomial

$$C0\ T0 + C1\ T1 + C2\ T2 + C3\ T3 + C4\ T4$$

was formed from the first five Chebyshev polynomials:

$$T0 = 1$$

$$T1 = x$$

$$T2 = -1 + 2\ x^2$$

$$T3 = -3x + 4\ x^2$$

$$T4 = 1 - 8\ x^2 + 8\ x^4$$

with x normalized to range from 0. to 1. over the mass range of the fit. The free parameters of the fit were the coefficients C0 through C4, the amplitude of the Gaussian peak, and the amplitude and mass of the Breit-Wigner peak.

The stability of the fits was investigated by repeating them with different starting values and by varying the mass range of the fit. Errors were assigned which covered the range of variation seen from fit to fit as well as the statistical error. In some momentum bins satisfactory fits were obtained without the fourth order term; in those cases that result was included in the average and error.

The appropriateness of the fourth-order polynomial was investigated with Monte Carlo data. Good fits were obtained to the detected mass distribution from the all-pion Monte Carlo. When this distribution was fit with the polynomial background plus a Breit-Wigner, the resulting "ρ^0" yields were small and consistent with zero. The parameter controlling vector particle production in the Feynman-Field Monte Carlo was adjusted so that the total ρ^0 yield agreed approximately with the ρ^0 yield obtained from the data (in a previous iteration of this whole process). The fits performed to the data were repeated on a comparable number of events from the Feynman-Field model. The results of the fits were compared to the true numbers of detected ρ^0s. The discrepancies found were comparable to the errors we quote for the data.

Typical fits are shown for each momentum bin in Figure 42.

6.2 RESULTS

The results obtained with the three methods above are gratifyingly consistent. The X|| and Pt^2 distributions are shown separately for the three methods in Figure 46.

The results of methods 1, 2 and 3 were averaged together and assigned errors that cover the full variation of all three methods. The contribution of the heavy lepton to the

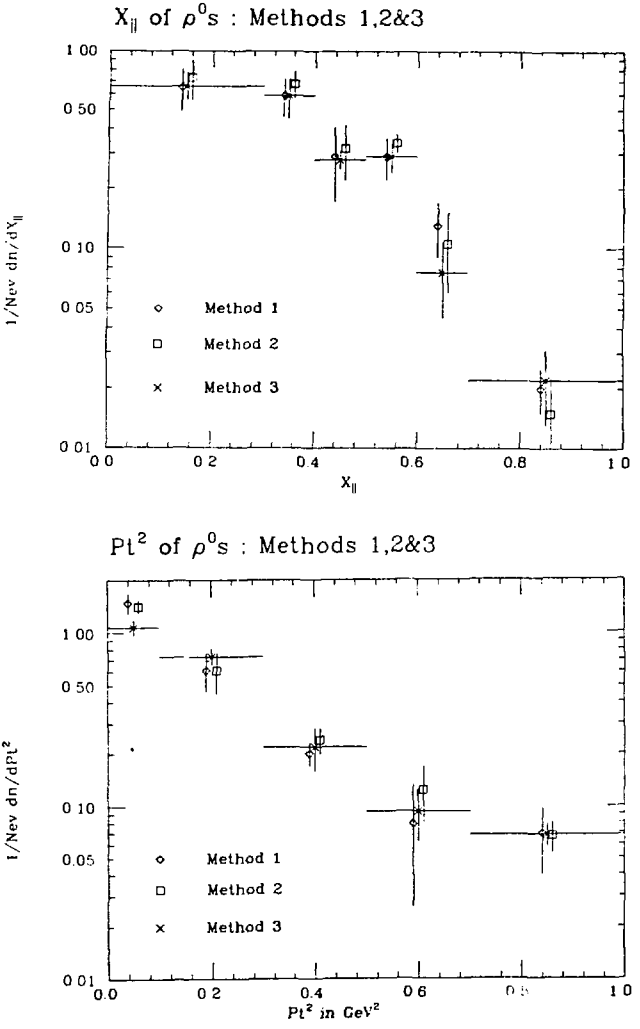

Figure 46: Comparison of Methods 1,2&3

ρ^0 production was estimated using the Monte Carlo and subtracted. The ρ^0s from the taus come from its A1 decay mode, which has been assumed to be 10% +/- 5%, with 100% of the A1s decaying to $\pi\pi\pi$. We have assigned 100% errors to the resulting ρ^0 momentum spectrum. Approximately 3% of all detected events are tau events. This subtraction is small compared to the errors in the fits; we do it explicitly for the sake of clarity. The numbers are given in Table 5.

TABLE 5

ρ^0 Production

bin	ρ^0 yield	tau	efficiency	ρ^0/event
all	8603 ± 1767	517	.52 ± .06	.39 ± .09
0.< X|| <.3	5186 ± 1736	109	.51 ± .06	.8 ± .3
.3< X|| <.4	1535 ± 471	104	.50 ± .07	.7 ± .3
.4< X|| <.5	801 ± 398	98	.55 ± .08	.4 ± .2
.5< X|| <.6	822 ± 260	81	.52 ± .08	.38 ± .13
.6< X|| <.7	262 ± 215	81	.57 ± .10	.11 ± .09
.7< X|| <1.	150 ± 123	44	.55 ± .10	.02 ± .02
0.< Pt^2 <.1	4315 ± 1295	273	.67 ± .10	1.5 ± .5
.1< Pt^2 <.3	3093 ± 1019	177	.49 ± .06	.75 ± .26
.3< Pt^2 <.5	756 ± 228	50	.36 ± .05	.25 ± .11
.5< Pt^2 <.7	338 ± 260	14	.34 ± .04	.12 ± .09
.7< Pt^2 <1.	306 ± 139	2	.29 ± .04	.08 ± .10

The raw ρ^0 yield, the predicted number of ρ^0s from tau decays, and the ρ^0 detection efficiency are given for all momenta and in bins of longitudinal momentum (in units of the beam energy) and in bins of transverse momentum in GeV^2. The corrected total ρ^0 production and the dn/dX|| and dn/dPt^2 are normalized to the efficiency-corrected number of produced hadronic events (tau events excluded).

The ρ^0 detection efficiency was calculated using two different production models. The first was the Feynman-Field model. The second was a modification of the all-pion model in which every event had one ρ^0. The results agreed within the statistical errors. A 10% uncertainty was added to the statistical errors to allow for the difference in trigger efficiency between these two models and the all-pion model.

The corrected $X||$ and Pt^2 distributions are shown in Figure 47. For comparison the figure includes the same distributions for all charged particles multiplied by 0.5. It is seen that the $X||$ distributions have approximately the same shape above $X||=0.3$. The Pt^2 distributions are consistent with having the same slope above $Pt^2 = .1\ GeV^2$. However the charged particle distribution is steeper at low Pt^2, whereas the ρ^0 distribution can be fit by a single exponential:

$$dn/dPt^2 = A \exp (- B\ Pt^2)$$

with $B = 5 +/- 1$.

Charged particles at low momentum can come from ρ decay, as well as K^0, eta, omega, and charmed particle decays. The multitude of sources means it is not possible to measure the distribution of primary pions. It is also not known how many of the ρs themselves may have come from higher mass particles. In the version of the Feynman-Field model used here, ρ^0s can come from the primary vertex or from eta'

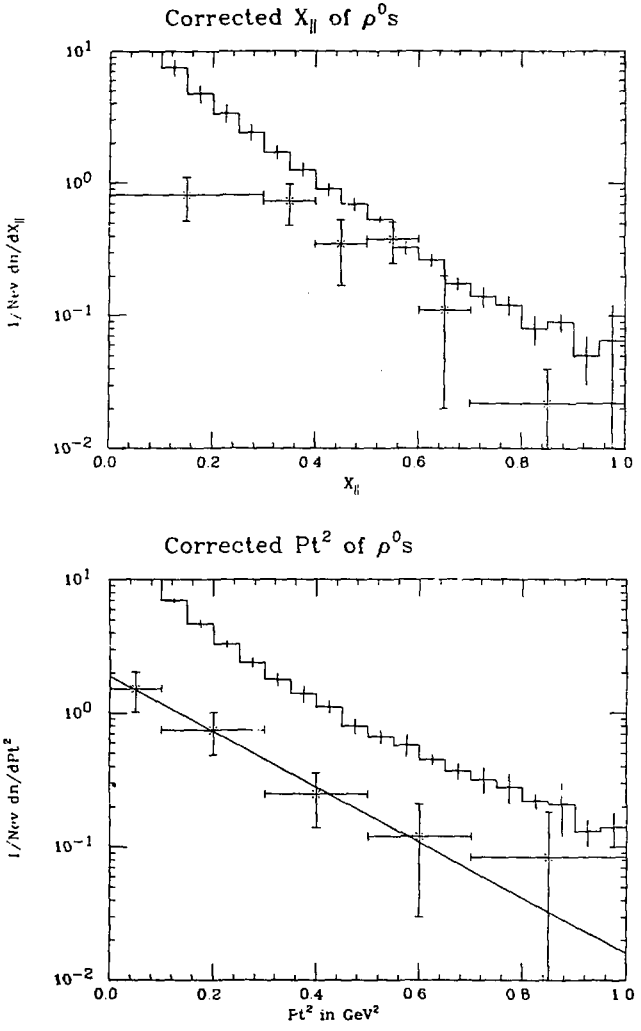

Figure 47: Corrected $X_{\parallel}$ and Pt^2 of ρ^0s.
The points are the corrected data for the number of ρ^0s per event per unit of X|| or per GeV of Pt^2. The histograms are the corrected X|| and Pt^2 distributions for all charged particles, multiplied by 0.5. The straight line is the fit: exp $(-5\ Pt^2)$.

decay, but not from charmed particle decay. An input ratio of 1:4 of vector particles to pseudo-scalar particles at the primary vertex produced approximate agreement with the measured total ρ^0 production. The average number of ρ^0s per event in the model as a function of the vector particle fraction V (V = vector / vector + pseudo-scalar) is shown in Figure 48 and compared to the data. In Figure 49 the model X|| and Pt^2 distributions are compared to the data. The Pt^2 distributions are in good agreement. The X|| distribution of the model is approximately exponential while the data has significantly fewer ρ^0s at low momentum. However the Feynman-Field model is not really designed to operate at these low energies. A slight change in the method of terminating each jet can reduce the number of ρ^0s at low momentum to give somewhat better agreement with the data. The data above X||=.3 are consistent with the commonly used equal vector and pseudo-scalar production. (The ρ^0 momentum distributions are not significantly changed by the increase in the vector particle fraction.) Therefore equal vector and pseudo-scalar production is in disagreement with the data only at low momentum. Without a more sophisticated model to fit the entire momentum spectrum, we cannot say whether 0.2 or 0.5 is preferred for the vector particle fraction.

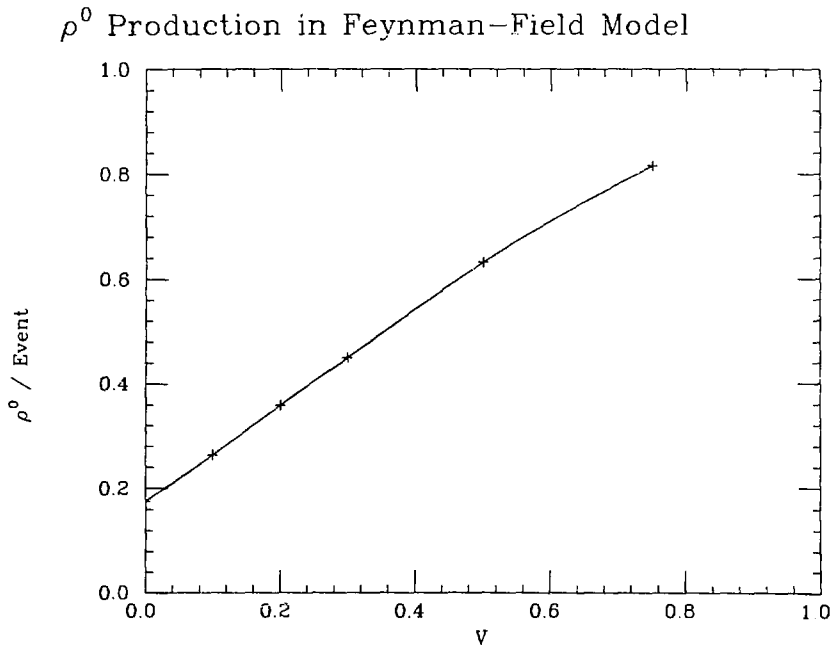

Figure 48: ρ^0 production in the Feynman-Field Model. Results from the Feynman-Field model for the number of ρ^0's per event as a function of the vector particle fraction parameter.

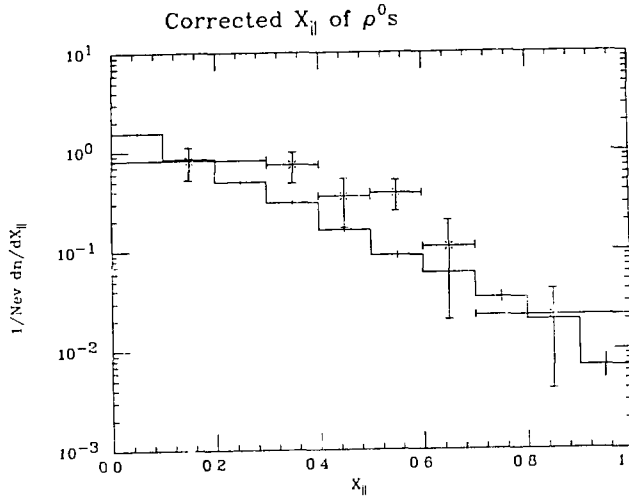

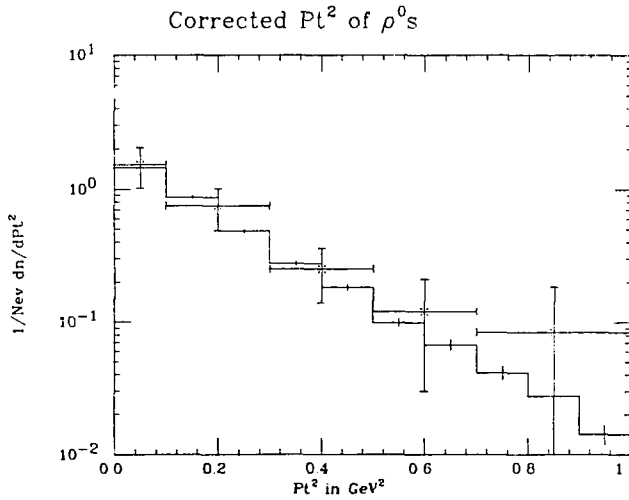

Figure 49: ρ^0 Momenta in Feynman-Field Model. The points are the corrected data. The histograms are the results of the model with the value .20 for the vector particle fraction at the primary vertex.

6.3 COMPARISON WITH PREVIOUS MEASUREMENTS

6.3.1 Mass

The accepted[30] value of the ρ^0 mass is 776 +/- 3 MeV. The effect of ρ-ω interference in the $\pi^+\pi^-$ decay mode is small[31]. However several experiments have observed the ρ^0 at approximately 750 MeV.[32] Jackson[33] has suggested that a broad resonance such as the ρ can be expected to appear with different peak values in different reactions. T. Fields and R. Singer discuss[34] a possible explanation of the low ρ mass in terms of the limited phase space available at each step of the chain decay of a heavy fireball. They suggest that the effect might be larger for lower momentum ρs.

A possible problem with our ρ fits is the presence of a K^{*0} in the $\pi^+\pi^-$ mass distribution just below the position of

---

[30] "Reviews of Particle Properties", Particle Data Group, Phys. Lett. 75B:1, 1978.

[31] W.W.M. Allison et. al. Phys. Rev. Lett. 24:618,1970. P.J. Biggs et. al., Phys. Rev. Lett. 24:1201,1970.

[32] Raja et. al. Phys. Rev. D16:2733, 1977. ($p\bar{p}$ at 100 GeV/c)
Alborow et. al., Nucl. Phys. B155:39, 1979. (pp at $\sqrt{s}$ = 23.6 to 63.0 GeV)
Ermilova et. al., Nucl. Phys. B137:29, 1978. ($p\bar{p}$ at 22.4 Gev/c)
Singer et. al., Phys. Lett. 60B:385, 1976. (pp at 205 GeV/c)

[33] J. D. Jackson, Nuovo Cim. 34:1644, 1964.

[34] T. Fields and R. Singer ,"Mass of the ρ^0 in NN Annihilation" in the Proceedings of the 4th International Symposium on Nucleon-Antinucleon Interactions, Syracuse, 1975, ed. by T.E.Kalogeropolous and K.C. Wali.

the ρ. To investigate this possibility, the data was re-analyzed using the time-of-flight information. Each charged particle was assigned a pion weight. If the particle had no time-of-flight information, the weight was 0. Otherwise the difference was calculated between the expected time-of-flight for a pion of that momentum and the measured value. The weight was

$$W = \exp\ (-.5\ \Delta T\ /\ \sigma\ ),$$

where σ is the resolution of the time-of-flight system, which was 0.4 ns for this data. Each combination of oppositely charged tracks was plotted weighted with the product of the two pion weights. All the fits described in section 1 were repeated on the weighted data, and the corresponding efficiencies were calculated. The resulting corrected X|| and Pt^2 distributions agreed with those obtained in section 1 within the errors quoted. The best fit values for the ρ^0 mass were also in agreement with those obtained with the unweighted plots. Monte Carlo studies indicate that the time-of-flight weighting would substantially reduce the K^{*0} contamination in the $\pi^+\pi^-$ mass spectrum. Since the weighting did not affect our results, we conclude that the K^{*0} is not a problem.

6.3.2 Rate

Our average number of ρ^0s per event corresponds to

$$R(\rho^0) = \sigma(e^+e^- \longrightarrow \rho^0\ X)\ /\ \sigma(e^+e^- \longrightarrow \mu^+\mu^-) = 1.7 +/- 0.4.$$

The PLUTO collaboration[35] reports a value for $R(\rho^0)$ of about 1 +/- .2 from 4.1 to 5.0 GeV center-of-mass energy. A plot of $R(\rho^0)$ vs. center-of.mass energy is shown in Figure 50. $R(\rho^0)$ is increasing with energy. Using the Mark 1 results[36] for the total hadronic cross section and the average charged multiplicity, we can translate the Mark 1 and PLUTO results for $R(\rho^0)$ into the relative numbers of ρ^0s and charged particles. The results are .06 +/- .01 at 3.6 GeV, .05 +/- .01 at 5.0 GeV, and .07 +/- .02 at 7.3 GeV; this is consistent with a constant ratio. We can also translate the PLUTO results into the average number of ρ^0s per event and then compare the Mark 1 and PLUTO results with those from inelastic anti-neutrino proton scattering.[37] As shown in Figure 51, the results from the anti-neutrino experiment are consistent with the e^+e^- experiments.

6.3.3 Momentum Distributions

A review by Kirk et. al.[38] of non-strange heavy meson production in hadron collisions (where Pt is measured

---

[35] J. Buerger, Moriond Conf. v.2:133, 1978.

[36] J.L.Siegrist, "Hadron Production by e^+e^- Annihilation at Center-of-Mass Energies Between 2.6 and 7.8 GeV", SLAC-225, 1979. (Thesis)

[37] M. Derrick et. al. ANL-HEP-PR-79-41, COO-3066-137, PU-487; Nov. 1979.

[38] H. Kirk et. al., Nucl. Phys. B128:397, 1977.

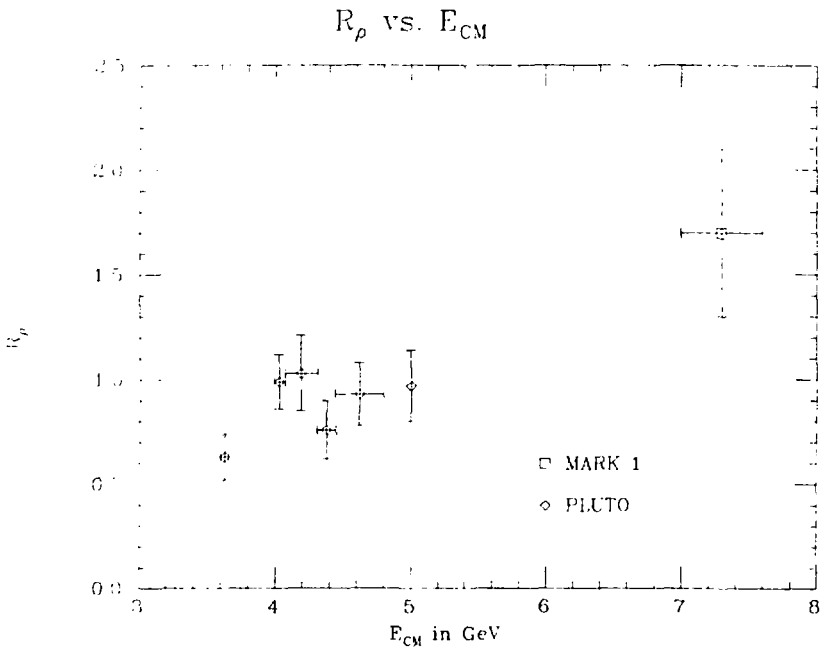

Figure 50: $R(\rho^0)$ vs. E_{CM}.

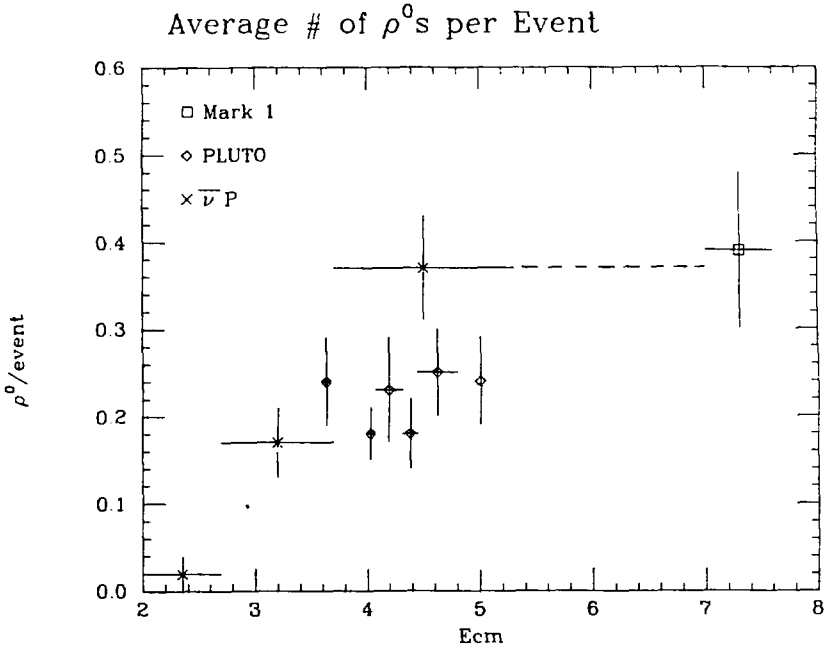

Figure 51: ρ^0 Production vs. Ecm.
Average number of ρ^0s per event vs. Ecm from Mark 1.
$R(\rho^0)/R$ vs. Ecm from PLUTO.
Average number of ρ^0s per events vs. W from inelastic anti-neutrino scattering.

relative to the beam axis) with beam momenta ranging from 6 to 205 GeV/c reports that they can all be fit by the form

$$dn/dPt^2 = A \exp (-b\ Pt^2)$$

with $b = 3.4 +/- .1\ (GeV/c)^2$. Our value of 5 +/- 1 gives a steeper slope, but the error is large.

Our Pt^2 distribution is compared to that from the anti-neutrino experiment, for which the average W was 3.4 GeV, in Figure 52. Here Pt is measured relative to the quark direction in both experiments. The results are roughly consistent.

We know of no other data on X|| of ρ^0s. PLUTO has measured the distribution in x_E = E / Ebeam between 3.6 and 5.0 GeV. This can be transformed into a distribution in X = P / Pmax, which is approximately X|| for large momenta. The anti-neutrino experiment measured the distribution in Z = E / Emax, where the energies are measured in the lab frame. Again, for large momenta, this should be approximate X||. The Z distribution of ρ^0s was also measured in inelastic muon-nucleon scattering.[39] All of these results are compared in Figure 53. The agreement on an absolute scale of such a wide range of experiments is quite remarkable. This is an indication that the process of quark fragmentation is independent of the source of the quark.

---

[39] C. del Papa et. al., Phys. Rev. Lett., 40:90, 1978.

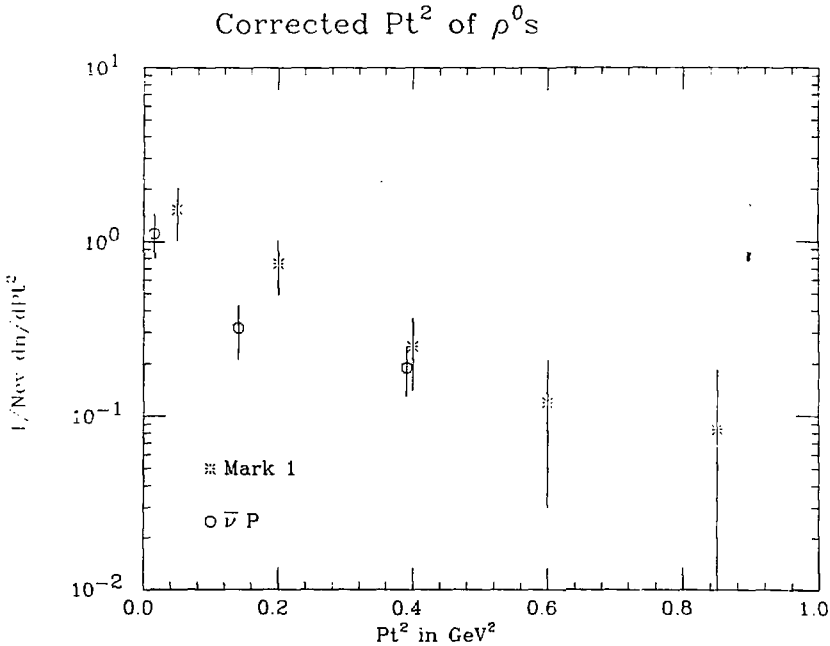

Figure 52: Pt^2 distribution of ρ^0s in e^+e^- annihilation at Ecm=7.3 GeV and in inelastic anti-neutrino scattering at $\langle W \rangle$ = 3.4 GeV.

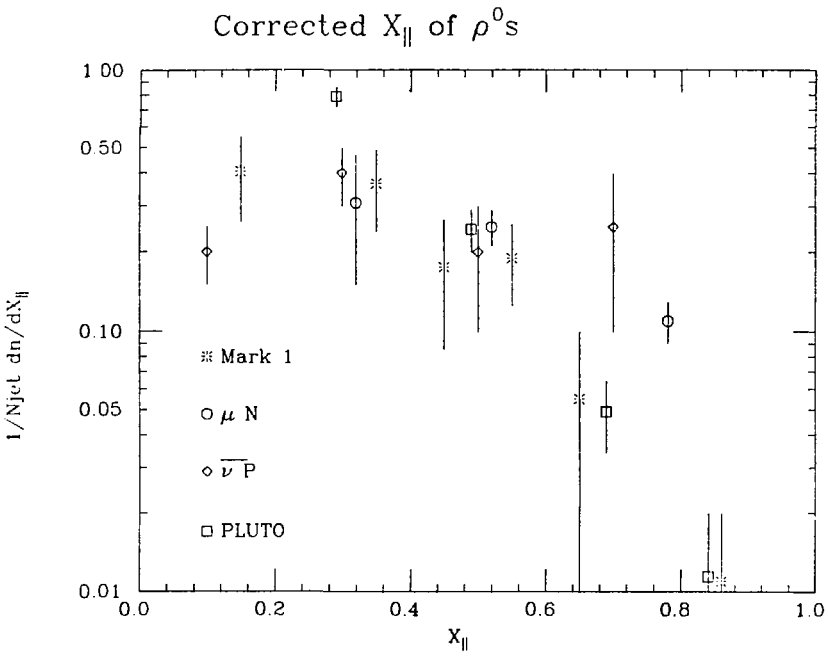

Figure 53: $X_{\parallel}$ Distribution of ρ^0s in e^+e^- annihilation at 7.3 GeV from Mark 1;
X distribution from 3.6 to 5.0 GeV from PLUTO;
Z distributions from anti-neutrino and muon scattering at <W> = 3.4 GeV.

Chapter VII

CONCLUSION

The data taken with the Mark 1 detector at SPEAR have demonstrated the existence of jets. The angular distribution of these jets, along with the nearly constant value of R above charm threshold, provide strong support for the existence of the reaction $e^+e^- \longrightarrow q\,\bar{q}$ as the underlying mechanism in hadron production in e^+e^- annihilation. The SPEAR results have been strikingly confirmed in the much higher energy data taken recently at PETRA. In addition to very clear evidence for two jet events, the PETRA data indicate the existence of some three jet events, where the third jet is presumably the result of the fragmentation of a high energy gluon radiated from one of the quarks.

The study of the reactions $e^+e^- \longrightarrow q\bar{q}$ and $e^+e^- \longrightarrow q\bar{q}g$ has a problem in that we observe not the quarks and gluons themselves, nor even necessarily the hadrons produced directly from the quarks and gluons, but the long-lived decay products of these hadrons. Thus twice removed from the reaction of interest, one is dependent on models of the intervening processes. We have in the Feynman-Field model a phenomenalogical parameterization of the quark fragmentation process, which predicts momentum distributions as well as

particle types. The decay properties of most particles are well known, but to date the study of charmed particle decays has concentrated on exclusive decay channels, and we know nothing, for example, about inclusive ρ^0s in D meson decay. In e^+e^- annihilation, charmed particle decays provide a substantial fraction of the final state particles we observe. In particular, it appears that most of the kaons come from charm decay, so that the K^0 momentum distributions reflect the charmed particle momenta generated in quark fragmentation folded with the K^0 momentum generated in charmed particle decays. The resulting distributions from our model agree well with the data. The ρ^0 distributions are not in such good agreement, but, lacking information on the contribution of charmed particles here, we don't yet know how to interpret this disagreement. In addition, the Feynman-Field model is intended for higher energies, where particle masses are not important. The relatively small number of ρ^0s observed at low momentum may be an effect of the small phase space available for producing heavy particles, an effect which is not included in the model.

These difficulties are unfortunate, but at present unavoidable. However, the real point of this thesis is not the model but the data, which is now available for comparison to any improved models which may be developed in the future. Although the present thrust of high energy physics lies in studying the quarks and gluons, work in

which the necessity of looking at hadrons is regarded as a nuisance, we hope that some attention will be turned in the future to an understanding of how quarks turn into hadrons, and that this thesis is a step in that direction.

Appendix A

RADIATIVE CORRECTIONS

In e+e- annihilation either of the initial state particles can emit a photon before the annihilation. Then the e+e- annihilate at a reduced center-of-mass energy and in a center-of-mass frame which is no longer at rest in the laboratory frame of reference. For example, in two jet events, the two jets are not colinear in the laboratory frame. To include these effects in our Monte Carlo, we must generate events with the correct photon distribution. Fortunately the initial state radiation is described[40] by well-understood Quantum Electrodynamics (QED).

To third order in α, the total cross section consists of a radiative part that has a final state photon and a non-radiative part with no final state photon:

$$\sigma_{tot}(s_0) = \sigma_r(s_0) + \sigma_{nr}(s_0).$$

The relevant Feynman diagrams are shown in Figure 54 . The non-radiative part is obtained from the second and fourth order graphs (g2 and g4) :

---

[40] Bonneau and Martin, Nucl. Phys. B27:381, 1971.

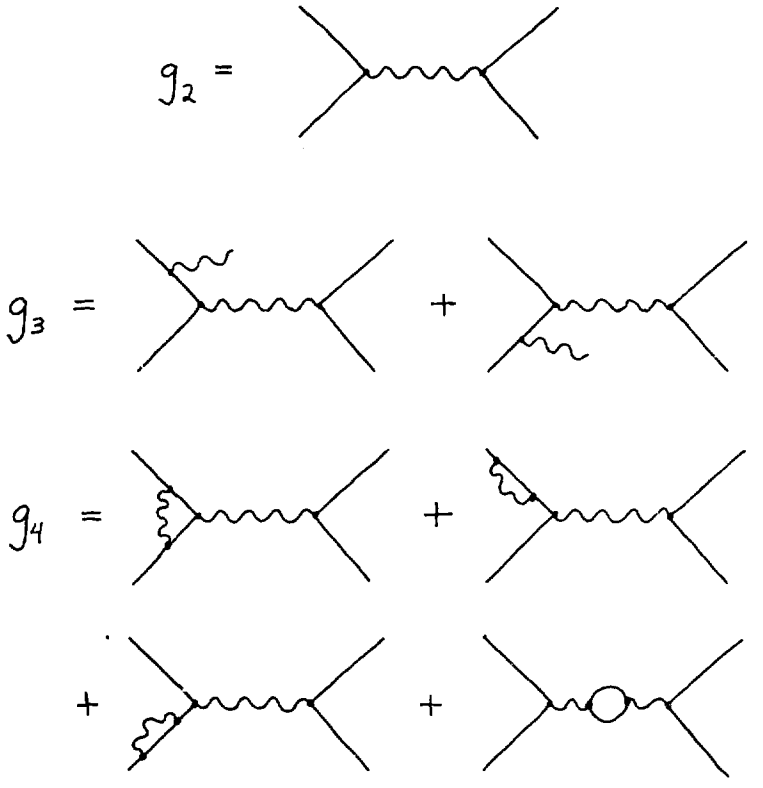

Figure 54: Feynman graphs for $e^+e^- \longrightarrow q\,\bar{q}$

$$\sigma_{nr}(s_0) = | g2 + g4 |^2$$

$$= | g2 |^2 + 2 \, Re \, (g2 * g4)$$

$$= \sigma_0(s_0) + 2 \, Re \, (g2 * g4)$$

where σ_0 is the total cross section calculated to second order. The radiative part is obtained from the third order graphs (g3) :

$$\sigma_r(s_0) = | g3 |^2$$

$$= t \int_0^{Eb} \frac{dQ}{Q} \left(1 - \frac{Q}{Eb} + \frac{Q^2}{2 \, Eb^2}\right) \sigma_0(s')$$

$$t = \frac{2\alpha}{\pi} \left(-1 + 2 \ln \frac{2 \, Eb}{Me} \right)$$

s' is the square of the e+e- center-of-mass energy after radiation; Eb is the nominal beam energy. The integral diverges at its lower limit. This divergence is cancelled by a divergence in the g2 * g4 terms of the non-radiative part. Since emission of very low energy photons is not detectable, we change the lower limit of the integral to Qmin=.01*Eb and transfer to the non-radiative cross section that part of the radiative cross section involving photons of energy less than Qmin. Then

$$\sigma_{nr}(s_0) = (1 + \delta') \, \sigma_0(s_0)$$

$$\delta' = \frac{2\alpha}{\pi}\left(\frac{\pi^2}{6} - \frac{17}{36}\right) + t\left(\frac{13}{12} + \ln\frac{Qmin}{Eb}\right)$$

We approximate the strong forward peaking of the bremsstrahlung process by putting the emitted photons exactly parallel to the electron and positron alternately. Then $s' = s_0(1-Q/Eb)$. The expression for the total cross section at a given energy involves the cross section at all lower energies. However, when the photon carries off a substantial fraction of the energy the large Lorentz boost sends all the particles down the beam pipe so that such events are never detected in an experiment like the Mark 1. In practice, we need not generate events with s' below 1 GeV^2. This gives an upper limit to the photon energy of $Qmax = Eb\ (1 - 1\ Gev^2/s_0)$. This neatly avoids the uncertainties in the cross section at low energies.

For each event we choose a photon energy Q by picking a random number X between 0 and 1 and solving

$PQ(Q) = X*PQ(Qmax)$

for Q, where

$$PQ(Q) = \sigma_0(s_0)\ (1 + \delta')\quad \text{for } Q < Qmin$$

$$PQ(Q) = \sigma_0(s_0)\ (1 + \delta') +$$

$$t\int_{Qmin}^{Q} \frac{dQ}{Q}\left(1 - \frac{Q}{Eb} + \frac{Q^2}{2\ Eb^2}\right)\sigma_0(s')$$

for Qmin < Q < Qmax.

Actually, we cannot solve the equation analytically, so we create an array PQ(IQ) with Q/Eb = 100.*IQ. Then find IQ so that

PQ(IQ-1) < X < PQ(IQ) and interpolate:

$$\frac{Q}{Eb} = .01 \left(IQ-1+ \frac{PQ - PQ(IQ-1)}{PQ(IQ) - PQ(IQ-1)} \right)$$

This binning would smooth out the fluctuations in R, so instead of using the measured cross section in calculating PQ(Q), we assume a cross section equal to a constant times 1/s. Then when a Q is chosen, it is weighted with R(s')/Rmax, i.e. events are kept with probability R(s')/Rmax, where Rmax is the highest value of R between 1 GeV^2 and s_0.

To get efficiencies for calculating the total cross section, etc., it is not sufficient to use the ratio of detected events to produced events. Convention has it that we are to determine not σ but σ_c, the second order cross section. Our data corresponds to those Monte Carlo events, both with and without radiated photons, which are detected. Since the non-radiative part of the cross section is $(1+\delta')\sigma_0$, the efficiency is

$$\text{eff} = (1+\delta') \frac{\text{\# of detected events}}{\text{\# of events produced with no radiation}}$$

The number of events produced as a function of s'/s_0 for $s_c=(7.3\ \mathrm{GeV})^2$ are given in Table 6 along with the corresponding detection efficiency.

TABLE 6

Initial State Radiation.

s'/s_0	# events produced	efficiency
0.-.1	256	0.00
.1-.2	170	.03
.2-.3	140	.14
.3-.4	189	.27
.4-.5	151	.34
.5-.6	196	.41
.6-.7	232	.47
.7-.8	317	.51
.8-.9	501	.56
.9-.99	1701	.60
1.0	6147	.61
total	10000	

Distribution in effective center-of-mass energy for a typical Monte Carlo run of 10000 events. The efficiency quoted for a given range of s' is the fraction of events produced with that s' which pass the standard analysis cuts described in Chapter 2.

An inclusive efficiency is obtained by binning the produced and detected particles in the appropriate variable. For example, for the K^0 momentum spectrum

$$\mathrm{eff}_{K^0}(p) = (1+\delta')\ \frac{\#\ \text{of } K^0\text{'s detected with momentum } p}{\#\ \text{of } K^0\text{'s produced with momentum } p \text{ in events with no radiation}}.$$

Figure 55 shows the effect of radiation on the jet axis. The angle of bend in the produced jet axis when transformed to the lab frame is plotted vs s'/s_0.

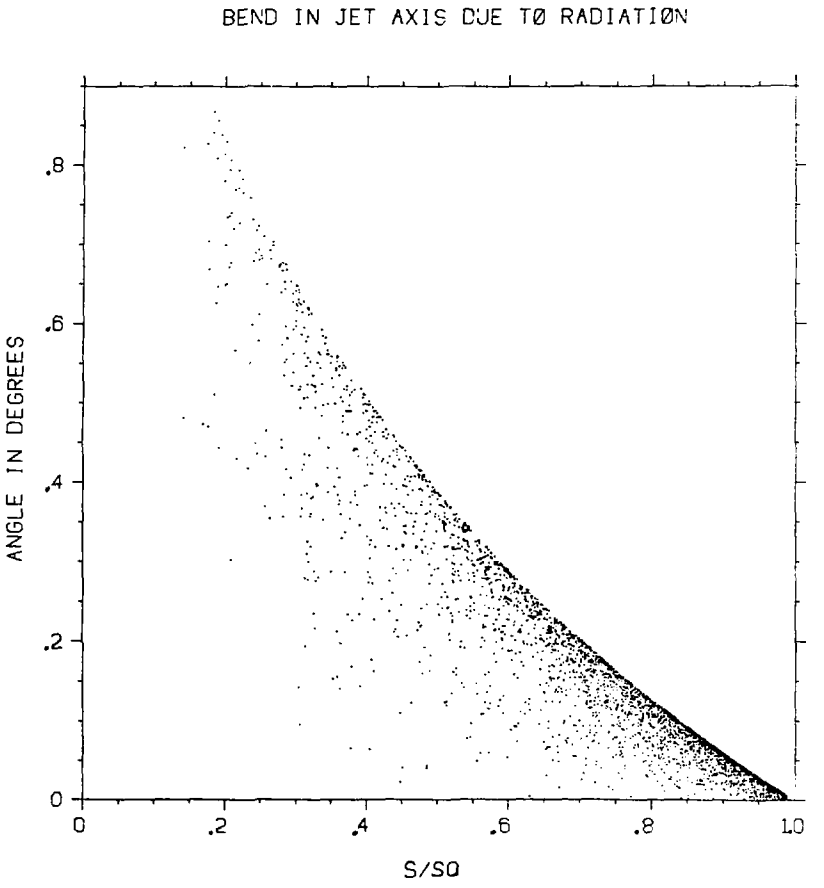

Figure 55: Effect of Radiation on Jet Axis
Detected events from a typical Monte Carlo run at 7.3 GeV. Only events with initial state radiation are included. For each event the 2 produced jet axes are transformed to the lab frame. The angle of non-colinearity is plotted vs s'/s_0.

Appendix B

LIMITED TRANSVERSE MOMENTUM MODEL

LIMPT generates events according to phase space multiplied by a matrix element that limits momentum transverse to the jet axis. When the matrix element is chosen to be Gaussian it gives the jet model that was used in the discovery of jets at SPEAR.

Event generation starts with a call to RADIAT to select an initial state 4-vector taking into account the probability of photon emission from one of the initial leptons. If the user has asked for tau production by setting MPARAM(5) = 1, the cross section used in calculating the radiation probability is the total hadronic cross section plus the tau cross section. Otherwise it is just the hadronic part.

The choice between a hadronic event and a tau event is made according to the ratio of the tau cross section to the total cross section at this (radiated) energy. If the decision is made in favor of the tau, control is passed to subroutine TAUPRD to accomplish it. Otherwise we proceed.

The hadrons are selected according to one of the various possible techniques (called submodels). The selection of the submodel is made by the input value of MPARAM(2). I usually use submodel 6 but I will briefly describe them all here for completeness.

If MPARAM(2) = 0, then we generate a fixed state with the particles given by the contents of NCHTY(3,40) in the common block CNPROD which must be set by the user in subroutine INIT. The first index is the charge: 1 = -1, 2 = 0, 3 = + 1; the second index is the particle type as described in the common block XMCHTY.

If MPARAM(2) = 1, then we generate an all-pion state Poisson in number of pi+ with average = XPARAM(1) and Poisson in number of pi0 with average = XPARAM(1)*XPARAM(7).

If MPARAM(2) = 2, then we generate an all-pion state Poisson in number of pi's with average = XPARAM(1). The pi's are made neutral with probability XPARAM(7).

If MPARAM(2) = 3, then we generate a general state of pions, kaons, nucleons, etas, etc. The total multiplicity is Poisson with average = XPARAM(1). The selection of particles is done in subroutine SELECT. Particles are chosen from among classes of differing strangeness and baryon number. The present classes and their weights are:

pions and etas	1-sum of others
kaons	XPARAM(11)

nucleons	XPARAM(12)
neutrinos	XPARAM(14)
rho's	XPARAM(15)
omega's	XPARAM(16)

Particles are chosen in pairs from the first 3 classes and singly from the last 3. Due to the effects of the conservation laws, the weights are not exactly equal to the achieved particle fractions.

Within each class, particles are chosen according to input random numbers, but the charge of the final state is constrained to 1 or 0. The final particle is selected to balance charge.

XPARAM(7) = fraction of pi0's in the pion/eta class

XPARAM(10) = fraction of eta's in the pion/eta class

XPARAM(8) = fraction of K0's in the kaons class

XPARAM(9) = fraction of n's in the nucleon class

rho's are chosen 1/3 neutral

If MPARAM(2) = 4, then we generate a general state exactly as in submodel 3. However when an event is discarded because of its phase space weight we will return to SELECT to choose a new state. This means that the particle fractions that come out in the end are influenced by their relative phase space weights.

If MPARAM(2) = 5, start with an all-rho state of poisson multiplicity with mean = XPARAM(1)/2. make them charged or

neutral with neutral fraction = XPARAM(7). make some of them into pion pairs, with XPARAM(15) of the rhos remaining as rhos. in this way the final state multiplicity is independent of the rho fraction.

If MPARAM(2) = 6, generate quarks and make them into hadrons (taken from Feynman-Field model [Nucl. Phys. B136:1, 1978]).

The quark flavor at the gamma --> q qbar vertex (IQUARK) is chosen with probability proportional to the quark charge squared. MPARAM(4) is the index of the highest mass quark to make here with 1=u, 2=d, 3=s, 4=c, 5=b, and 6=t.

The hadron multiplicity NP is chosen according to a Poisson distribution, with the mean (AVMULT) determined by XPARAM(1). AVMULT is corrected for the center-of-mass energy and for the excess multiplicity from the primary quark:

```
AVMULT = XPARAM(1) + 4.8 * ALOG (SQRTS/TECM)
                   - 2. * AVMQ(IQUARK).
```

SQRTS is the center-of-mass energy after radiation and TECM is the nominal center-of-mass energy. AVMQ is zero except for heavy quarks. For the charmed quark it is the average D decay multiplicity minus 1.

To make the NP hadrons we add NP-1 q-qbar pairs from the sea to the primary q qbar. u-ubar and d-dbar pairs are

chosen with equal probability. The probabilities for s-sbar and c-cbar pairs are equal to XPARAM(3) and XPARAM(4) respectively. Starting with the primary quark, we work our way down the quark chain making hadrons out of each adjacent q and qbar. Thus charge, strangeness, etc. are automatically conserved. For neutral combinations SU(3) mixing is used to choose between the three possible hadrons. The spin is chosen to be 0 or 1 with spin 1 having probability XPARAM(6). To keep the multiplicity under control, vector particles and etas count as two particles. This means we must remove a q-qbar pair from the chain for each such hadron made, and this is done in such a way as to not disturb the conservation laws. Quark pairs will also be deleted if we run out of energy.

Now we are ready to generate the 4-vectors by calling the SAGE subroutine GENIUS, which is so named because it produces limited-transverse-momentum phase space so much more efficiently than anything which was written previously. (Actually it was given that name at SLAC. The authors Carey and Drijard [JCP 28:327, 1978] called it GENLON in the Fermilab program package NVERTX. It was obtained by Roger Chaffee and installed as part of the SLAC copy of SAGE.) Even so, it is not perfect, so it assigns each event a weight equal to the correct probability divided by the

actual probability. To obtain an unbiased sample of events, we determine the maximum possible weight and then keep events with probability equal to their weight divided by the maximum weight. The maximum weight is an unknown function of the center-of-mass energy, the multiplicity, and the particle masses. The maximum weight is found once for each multiplicity and event type ITYPEV (which is always 1 except for submodel 6, for which it is IQUARK) by generating MPARAM(3) events in each class. (If MPARAM(3) is less than 0 all events are kept.) The maximum weight is corrected for energy by

```
WTMAXT = WTMAX(NP,ITYPEV) * (TECM/SQRTS)**2
         * ( ALOG10(SQRTS) / ALOG10(TECM) )**(NP-2)
```

This formula was obtained from the infinite-energy limit of the longitudinal phase space integral given in Byckling and Kajantie [Particle Kinematics, p.192, John Wiley & Sons Ltd., London, 1973]. However it is only approximate at our energies. Due to this and the unknown dependence on masses, we protect ourselves from horrid inefficiencies by resetting the maximum weight after MPARAM(3) unsuccessful tries to the highest in those MPARAM(3). For submodel 3, every time an event is discarded we go back and select new hadrons keeping the same multiplicity. For all other models we retain the same particles until an event is kept.

LIMPT takes advantage of the various matrix elements available in GENIUS.

If MPARAM(1) = 5 the matrix element squared is

|M|**2 = exp (-NP/(NP-1) sum Pt**2 / R**2), R = XPARAM(5).

If MPARAM(1) = 51 it is

|M|**2 = exp (- sum |Pt| / R), R = XPARAM(5).

If MPARAM(1) = 52 it is

|M|**2 = product (m**2 / (m**2 + sum Pt**2))**R,

R = XPARAM(5), m = XPARAM(17).

If MPARAM(1) = 53 it is

|M|**2 = exp (- sum P1**2/R1**2 - sum P2**2/R2**2),

R1 = XPARAM(5), R2 = XPARAM(17).

GENIUS uses the z axis to calculate Pt; i.e. the jet axis is along z. Now we choose a jet axis according to the distribution

d sigma ~ 1.+ alpha*cos(theta)**2

```
+ alpha*polsq*cos(2phi)*sin(theta)**2
```

where alpha = XPARAM(2) and the beam polarization squared polsq = XPARAM(13), theta is the angle to the beam, and the beam polarization is along phi = 90 degrees.

The event is rotated by an arbitrary angle about the z axis, then rotated to the chosen jet axis, and then boosted to the lab frame.

The parameters for the LIMPT model, the usual values used to fit the 7.4 GeV data, and the submodels to which they apply are summarized in Table 7.

TABLE 7

Parameters for LIMPT model

parameter	usual value	sub-model	meaning
MPARAM(1)	53	all	form of matrix element
MPARAM(2)	3,6	all	submodel
MPARAM(3)	50	all	number of events to make in finding maximum weight
MPARAM(4)	4	6	highest mass quark to make at gamma ⟶ q qbar vertex. 1=u 2=d 3=s 4=c 5=b 6=t
MPARAM(5)	1	all	1 to produce taus. 0 for none.
XPARAM(1)	10.5	1-6	average multiplicity
XPARAM(2)	1.0	all	alpha in jet axis distribution
XPARAM(3)	0.0	6	probability of s sbar quarks in sea
XPARAM(4)	0.0	6	probability of c cbar quarks in sea
XPARAM(5)	.55	all	R or R1 parameter for matrix element
XPARAM(6)	0.1	6	vector particle fraction (rest is pseudo-scalar)
XPARAM(7)	0.5	3&4 1,2,5	pi0 / (pi+eta) neutral fraction
XPARAM(8)		3&4	K0 / K
XPARAM(9)		3&4	n / (n+p)
XPARAM(10)		3&4	eta / (pi+eta)
XPARAM(11)		3&4	kaon weight
XPARAM(12)		3&4	nucleon weight
XPARAM(13)	0.0	all	beam polarization squared
XPARAM(14)		3&4	neutrino weight
XPARAM(15)		3&4	rho weight
XPARAM(16)		3&4	omega weight
XPARAM(17)	.55	all	m or R2 parameter for matrix element

Appendix C

FEYNMAN-FIELD MODEL

Seiden[41] and Feynman and Field[42] have proposed a phenomenalogical model for the fragmentation of quarks into hadrons. We have adapted this model for e^+e^- annihilation in a way that conserves charge, strangeness, and charm, and energy and momentum. The details of the model as we have implemented it are given here.

Event generation starts with a call to RADIAT to select an initial state 4-vector taking into account the probability of photon emission from one of the initial leptons. If the user has asked for tau production by setting MPARAM(5) = 1, the cross section used in calculating the radiation probability is the total hadronic cross section plus the tau cross section. Otherwise it is just the hadronic part.

The choice between a hadronic event and a tau event is made according to the ratio of the tau cross section to the

---

[41] A. Seiden, Phys. Lett. 68B:157, 1977.
A. Seiden, T.L. Schalk, and J.F. Martin, Phys. Rev. D 18:3990, 1978.

[42] R.D. Field and R.P. Feynman, Nucl. Phys. B136:1, 1978.

total cross section at this (radiated) energy. If the decision is made in favor of the tau, control is passed to subroutine TAUPRD to accomplish it. Otherwise we proceed.

The quark flavor at the photon $\longrightarrow q\,\bar{q}$ vertex is chosen with probability proportional to the quark charge squared. MPARAM(4) is the index of the highest mass quark to make here with 1=u, 2=d, 3=s, 4=c, 5=b, and 6=t. The primary quarks are assumed to be massless with energy equal to the beam energy.

The primary q and $\bar{q}$ are separately fragmented into hadrons by subroutine GOJET. The fragmentation proceeds by iterating the process $q \longrightarrow q'$ + hadron until the energy contained in the hadrons is approximately equal to the initial quark energy. The steps involved in each iteration are described below and illustrated in the flowchart of Figure 56.

First a new $q\,\bar{q}$ pair is chosen from the sea. u and d quarks are taken with equal probability, strange quarks with some smaller probability (F-F use .2), and heavier quarks never. The q and $\bar{q}$ are given equal and opposite transverse momentum with respect to the primary quark direction. The transverse momentum is chosen according to the distribution

$$d\,n\,/\,d\,Pt^2 \sim \exp\,(\,-\,Pt^2\,/\,r^2\,)$$

where r has been adjusted so that the observed transverse momentum distribution agrees with the data ($r \sim .35$ GeV).

FLOW CHART OF GOJET

$EP = 2\ E_{quark}$

$ELEFT = E_{quark}$

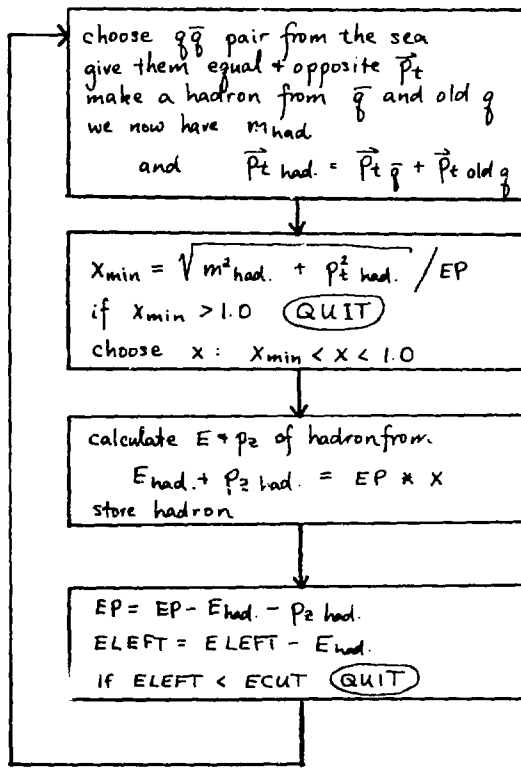

Figure 56: Flow Chart of Quark Fragmentation Subroutine (GOJET)

when a hadron is formed from the old quark and the new anti-quark. The hadrons are always mesons in this model since we always get $q\bar{q}$ pairs. They are chosen to be pseudo-scalar and vector with some relative probability for which F=F use 1. The SU(3) mixing for the Iz=0 case is done. The transverse momentum of the hadron is simply the vector sum of the transverse momenta of its constituents.

The hadron longitudinal momentum is found from a primordial splitting function f(x). It is assumed that the same splitting function can be used at each step in the iteration. In other words, we must be at a high enough energy so that only relative momenta are important and mass effects can be ignored. Since energy and momentum cannot both be conserved in the decay of a massless quark into a quark and a hadron, we use the variable $\epsilon = E + Pz$, which can be conserved. The form of the splitting function proposed by Feynman and Field for light quarks (u,d,s) is

$$f(x) = 1-A + A\ (N+1)\ (1-x)^N$$

where $x = \epsilon(\text{hadron}) / \epsilon(\text{old quark})$ is between 0 and 1. Feynman and Field use N = 2, and A = .77 to .88 . The constant term is there so the resulting inclusive distribution $F(x||)$ does not go to zero at $x||=1$. If that term is left out (i.e. A=1), there is a simple relationship between the splitting function and the inclusive distribution:

$$x||\ F(x||) = f(x)\ .$$

We use a constant splitting function for the heavier quarks.

We do not wish to allow hadrons to go backwards, i.e. have momentum anti-parallel to the primary quark's momentum. This requirement sets a lower limit on x for each hadron, which depends on the hadron mass and transverse momentum, and on the ϵ of the old quark:

$$x_{min} = sqrt\ (\ m^2 + Pt^2\ )\ /\ \epsilon(\text{old quark})$$

If x_{min} is larger than 1.0 we cannot give the hadron forward momentum, so the current hadron is discarded and the iteration is stopped with the previous hadron as the last particle in the jet.

If we had no other means of stopping the iteration, the finite hadron masses and transverse momenta would mean that the average total energy in hadrons would be larger than the primary quark energy. To avoid this, we stop the iteration when the total energy in hadrons has come within ECUT of the beam energy. ECUT is chosen to be a reasonable guess at the energy required to make another hadron. We have tried both a pion mass and the average transverse mass calculated assuming a pion mass. The results are compared in Figure 57. When the iteration is completed, we have n hadrons and n+1 quarks in continuous chain with a known ϵ, $\vec{Pt}$ and mass for each of them.

The two primary quarks from $e^+e^- \longrightarrow q\,\bar{q}$ are fragmented independently. Then we have two separate jets, each with a left over q or $\bar{q}$. The two jets could be joined by making a

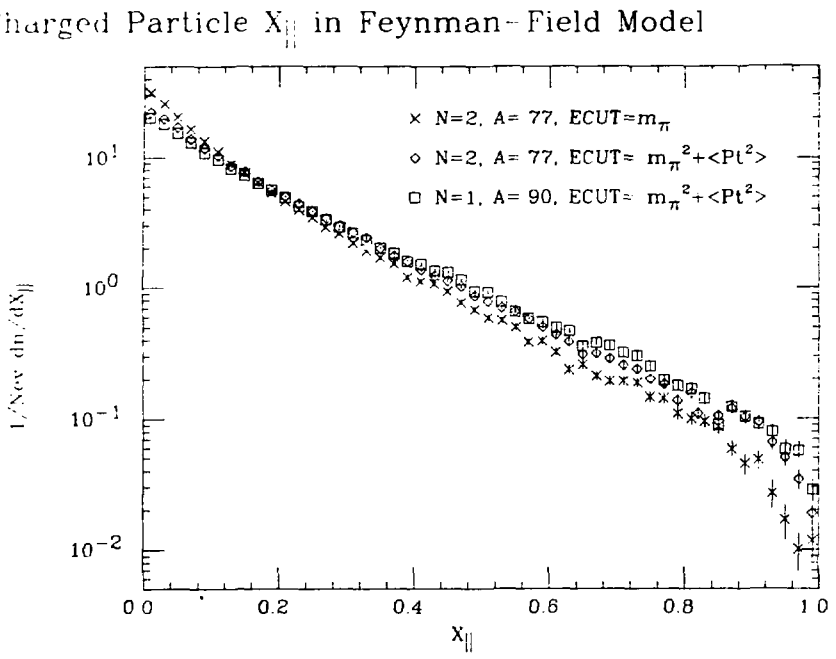

Figure 57: Feynman-Field Charged Particle $X_{\parallel}$ for various modifications of the model (see text).

hadron from the left-over q and $\bar{q}$. However, since each of the jets have already used up on average nearly all of the available energy, we instead split up the last hadron of one of the jets and delete the last $q\,\bar{q}$ pair. Then the remaining left-over q and $\bar{q}$ are made into a hadron. The joining process is illustrated in Figure 58.

Since the quark chain is now continuous, the sum of E and Pz are now conserved, as well as $\vec{Pt}$, charge, strangeness, etc. Energy and momentum are not separately conserved, as shown in Figure 59. However we can adjust separately the two primary quark energies to achieve exact energy and momentum conservation. The ϵ for each hadron is then re-scaled to the new quark energy, and the hadron energy and momentum calculated from ϵ.

There is a certain amount of arbitrariness in this model in how to end each jet and in how to join them. Both affect the low momentum hadrons directly, but through the re-scaling they affect the high momentum hadrons as well. Two Monte Carlo runs were made at Ecm = 7.3 GeV, one in which a jet was terminated when the remaining energy became less than one pion mass; in the other the energy cut-off was set at the average transverse mass = sqrt ($m_\pi^2 + \langle Pt^2 \rangle$) The results are compared in Figure 57. Since similar changes can be achieved by changing the parameters of the splitting function, it is clear that these parameters can

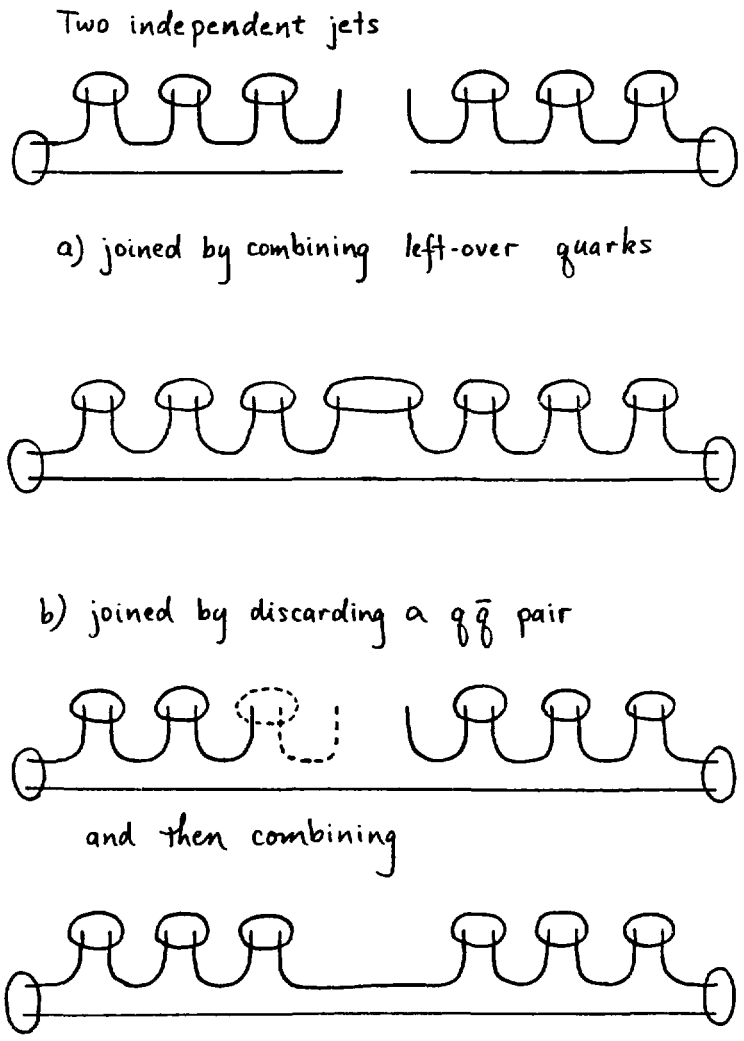

Figure 53: The Joining of Two Jets.
a) by combining the two left-over quarks.
b) by discarding a $q\,\bar{q}$ pair and re-making the last hadron.
Method (b) is used in our program.

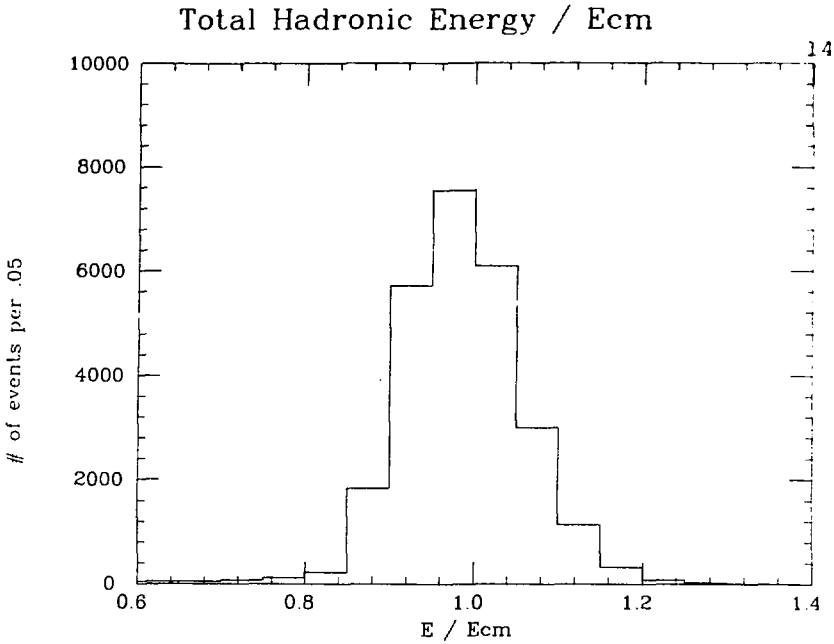

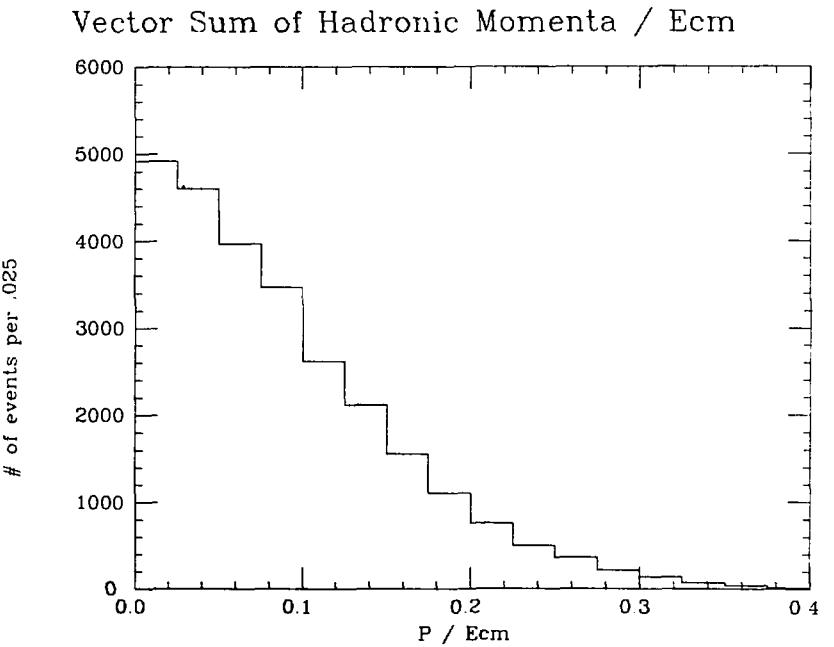

Figure 59: Total Energy and Momentum before Re-scaling.
a) Total energy / 2*Ebeam
b) Total momentum / 2*Ebeam

not be uniquely determined. Another Monte Carlo run was made with the average transverse mass for the energy cut-off and N=1, A=.77. The results are shown in Figure 57. The Feynman-Field model which we compare to the data in this thesis is actually the sum of these three runs.